Visualization of nucleation and growth of supramolecular networks on Cu(001) and Au(111)

Daniel Schwarz | Universiteit Twente | 2012

VISUALIZATION OF NUCLEATION AND GROWTH OF SUPRAMOLECULAR NETWORKS ON CU(001) AND AU(111)

Daniel Schwarz

Committee members:

Chairman and Secretary:

Prof. Dr. G. van der Steenhoven | University of Twente

Supervisor:

Prof. Dr. Ir. B. Poelsema | University of Twente

Assistant Supervisor:

Dr. R. van Gastel | University of Twente

Members:

Prof. Dr. C. Kumpf | Forschungszentrum Jülich
Prof. Dr. H.P. Oepen | Universität Hamburg
Prof. Dr. B.J. Ravoo | Universität Münster
Prof. Dr. W.J. Briels | University of Twente
Prof. Dr. Ir. H.J.W. Zandvliet | University of Twente

VISUALIZATION OF NUCLEATION AND GROWTH OF SUPRAMOLECULAR NETWORKS ON CU(001) AND AU(111)

DISSERTATION

to obtain

the degree of doctor at the University of Twente,

on the authority of the rector magnificus,

Prof. Dr. H. Brinksma,

on account of the decision of the graduation committee,

to be publicly defended

on Wednesday 21 November 2012 at 14:45 hrs

by

Daniel Schwarz

born on 25 July 1983

in Mainz, Germany

This dissertation has been approved by:

Supervisor: Prof. dr. ir. B. Poelsema
Assistant Supervisor: Dr. R. van Gastel

Contents

Contents

Introduction

1.1 Molecular self-assembly

Controlling the structure of materials on an atomic or molecular scale is the ultimate goal in material science. The strategies to achieve this goal can be broadly categorized into "top-down" and "bottom-up" approaches [1].Top-down techniques imprint the desired structure on a surface. A prime example is photolithography. To a certain degree one can see this as advanced relatives of archaic methods like carving or forging. The most sophisticated tool in this respect is the scanning tunneling microscope (STM) [2], which allows to image and manipulate single adatoms or -molecules on a surface [3]. However, STM is a slow, sequential technique and fabrication of nanostructures on a large scale would be unacceptably expensive and time-consuming.

A smart alternative for the construction of nanostructures is inspired by nature. In supramolecular chemistry, the self-assembly capabilities of organic molecules are used, inspired by basic biological processes [4, 5, 6]. A mixture of molecules is brought together in solution and, under the right conditions they come together and assemble into highly ordered structures. This bottom-up technique allows structural control on a molecular level by selecting the individual building blocks. An important aspect is that the molecules interact through non-covalent bonds, e.g., hydrogen bonds. The interaction between units is thus rather weak and the self-assembly process is governed by thermodynamics. The desired structure represents the thermodynamic minimum, which has the big advantage of an intrinsic error-correction mechanism: Molecular units that attached at wrong sites can detach again and reattach at the correct position.

Supramolecular chemistry in solutions is a well-established and understood science. Bringing this knowledge together with surface science bears

high promise for the fabrication of novel and functional molecular 2D nanostructures. This is not only interesting from a technological point of view, but also to increase the fundamental understanding of the driving forces behind the self-assembly process. The controlled environment of single crystalline surfaces and the reduced dimensionality allows to study in detail how the molecular building blocks interact with each other using well-established techniques [7, 8, 9].

1.2 Benzoic acids on metal surfaces

Benzoic-acids adsorbed on single crystalline metal surfaces belong to the more frequently studied systems [10, 11, 12, 13, 14, 15, 16, 17, 18, 19, 20]. Here, the benzene rings of the molecules act as backbones, allowing a flat adsorption geometry on the metal substrates. The functional carboxylic acid groups, on the other hand, define the interaction between molecules. Typically, the molecules interact through the formation of hydrogen bonds or through metal-coordination bonds. In the latter case, metallic atoms, either taken from the substrate or deliberately co-deposited, are incorporated in the structures [21].

The nanostructures that are formed depend strongly on the shape of the molecular building block; especially the positions of the functional groups are decisive. Also, the substrate plays a major role: it imposes its periodicity and symmetry on the adsorbed building blocks or even induces chemical changes. An example for the latter is the metal catalyzed deprotonation of carboxylic acid groups.

We illustrate the versatility of nanostructures that can be formed by three examples. All three examples have exactly the same basic building block: 4,4'-biphenyldicarboxylic acid (BDA). BDA is a linear molecule consisting out of a backbone of two phenyl rings and functional carboxylic acid groups at opposite ends. The length of the molecule is about 1.15 nm as measured from O-atom to O-atom on the two carboxylic acid groups (see sketch in Fig. 1.1). BDA is a common building block in supramolecular chemistry and in the synthesis of metal-organic-frameworks [22, 23, 24].

In Fig. 1.1(a)-(c) we present STM images of BDA adsorbed on Au(111) (see Chapter 7), on Cu(001) (Chapters 3-6) and on Cu(001) co-adsorbed with Fe adatoms. In each case, the molecules interact with each other with different motifs and thus order in different structures. On Au(111), the carboxylic acid groups remain protonated at room temperature. The molecules can thus interact by forming dimerized hydrogen bonds between the carboxylic
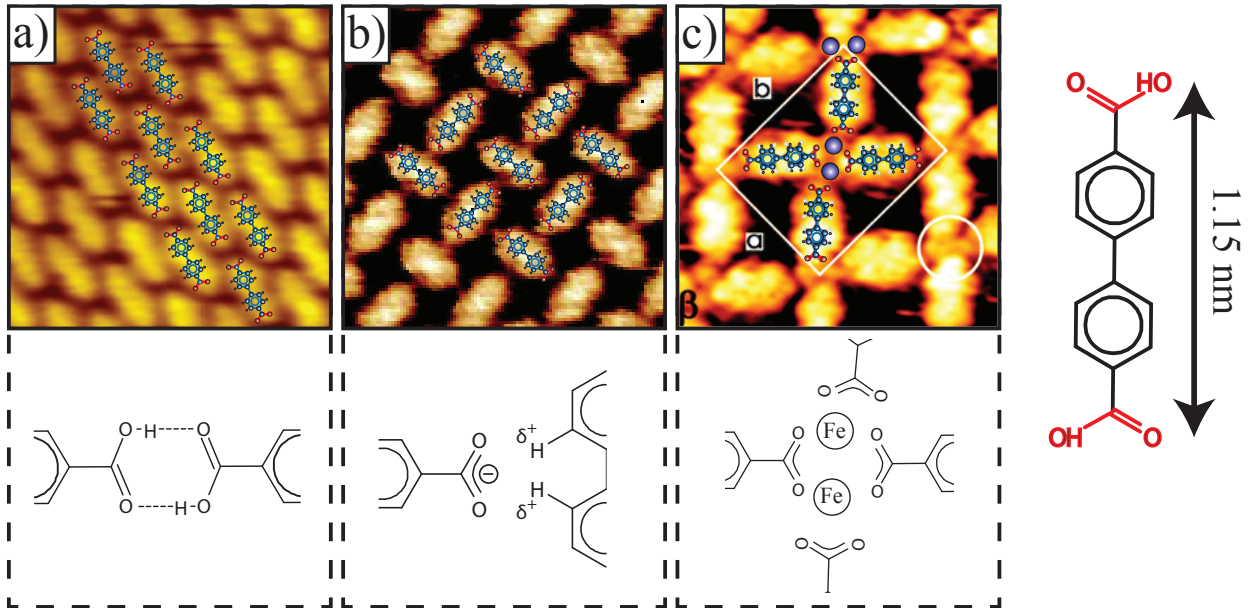
Figure 1.1: Three example STM images for nanostructures formed by BDA (see sketch on the right) through different binding motifs: **(a)** BDA adsorbed on Au(111), forming chain like structures with head-to-tail bonding [Adapted from [25]]. **(b)** BDA on Cu(001): the carboxylic acid group is deprotonated and head-to-tail bonding is not possible, rather carboxylate-phenyl bonds are formed [Adapted from [12]]. **(c)** BDA on Cu(001) co-adsorbed with Fe adatoms. Molecules form structures through metal coordination bonds [Adapted from [26]]. All three images are 5 nm by 5 nm.

acid groups. This bond is very stable and the molecules form a closed-packed structure (Fig. 1.1(a)). On Cu(001), on the other hand, the acid deprotonates below room temperature. The molecules form (weak) hydrogen bonds between the carboxylate group and the phenyl ring of the neighboring molecule, which is rotated by 90° (Fig. 1.1(b)). The resulting open nanostructure originates both from the four-fold symmetry of the substrate and the molecular interaction. The resulting, well-ordered nanopores have been proposed as hosts for the controlled adsorption of larger guest molecules, preventing their clustering [17, 27]. If Fe is deposited onto a Cu(001) surface which is already covered with BDA nanostructures, the molecules rearrange into a 2D metal-organic-framework together with the Fe adatoms (Fig. 1.1(c)) [26]. Fe atoms act as linkers between carboxylate groups. In this way, it is possible to arrange pairs of Fe atoms separated at well-defined distances of nanometers. By adjusting the length of the molecule, e.g., exchanging it with a triphenyl, it is possible to alter the pore size and the separation distance of the Fe atoms.

1.3 Scope and outline of this thesis

The scope of this thesis is to enhance the basic understanding of the thermo-dynamic driving forces behind the self-assembly process and the molecule-substrate interaction. This is accomplished by an *in-situ* observation of the processes happening on the surface. For any application of the molecular networks (Fig. 1.1), it is important to create structures with a high crystal quality, i.e., a minimum amount of defects and crystalline domains. Understanding the driving forces will help to identify the relevant parameters and thus to optimize the growth conditions. While the molecules form structures with lattice constants on the order of nanometers, individual 2D crystalline domains exceed sizes of several hundreds of nanometers. STM is excellent to image the nanostructures on a molecular scale, but the limited scan range and scan speed hinder the in-situ observation of domain nucleation and growth. Observing fast processes on mesoscopic length scales lies at the heart of low energy electron microscopy (LEEM). Research questions include, whether or not the growth can be described within existing models for metal/semiconductor epitaxy [28, 29], or how these models need to be adjusted. For example, entropy effects will play a large role, simply arising from the size of the molecules. Also, the chemical structure of the molecules may be altered on the reactive metal surfaces.

Most of this work is devoted to BDA grown on Cu(001). This system has the advantage to be rather straightforward: over a wide range of parameters (BDA coverage and temperature), we observe only a single ordered BDA phase (see STM image in Fig. 1.1(b)), thus simplifying the interpretation of results. We found that several established concepts from thin-film growth can be modified to describe the growth of BDA on Cu(001).

We will start in Chapter three with a discussion of the phase equilibrium between an ordered, 2D crystalline phase and a disordered, diluted phase formed by adsorbed BDA molecules. From the temperature dependence of the equilibrium between both phases, we determined the 2D cohesive energy of the molecules in the ordered phase. The diluted phase is quite dense, which we attribute to entropy effects, due to the much larger size of the molecule compared to the mesh size of the Cu-lattice.

In Chapter four we study in detail the nucleation of the 2D crystalline domains from the diluted molecular surface phase. A common concept in nucleation models is the critical nucleus size. Nuclei, which are smaller than this critical size, tend to be unstable and decay again, while larger nuclei are stable and tend to grow. Due to nucleation and growth close to thermal equilibrium, the critical fluctuations in the BDA/Cu(001) system become

huge. For metal or semiconductor epitaxy at around room temperature, the critical nucleus consists typically only out of a few atoms. Here, we observed critical sizes of several hundred molecules. We were able to follow this critical behavior in-situ in unparalleled detail.

The BDA growth is inevitably influenced by the morphology of the Cu(001) substrate. In Chapter five we discuss the role of substrate steps on the domain growth. Domains cannot grow over Cu steps, while the steps are permeable for individual molecules. The combination of these effects leads to two important observations: First, nuclei have a maximum size which is determined by the Cu terrace size. This maximum size may result in delayed domain nucleation on neighboring terraces. Secondly, domains show several Mullins-Sekerka growth instabilities. A novel type of this instability includes fast growth along the steps.

BDA molecules show a strong affinity for the Cu surface. If molecules are deposited onto already existing domains, this can lead to the formation of a compressed phase with denser packing. The compression is a result of a trade-off between a loss of average adsorption and interaction energy, and a gain of total free energy due to the increased number of molecules in the layer. In Chapter six we present a study on the formation of the compressed structure and the conversion back into the relaxed structure upon stopping the deposition of molecules.

Finally, in Chapter seven we will turn to a different system: BDA on Au(111). Unlike on Cu(001), the acid group is protonated at room temperature, which allows favorable head-to-tail dimer bonding (see STM image in Fig. 1.1(a)). Upon increasing the temperature slightly, we can follow in-situ the deprotonation of the molecules, which results in an impressive shape transformation of 2D domains on the *mesoscopic* scale. Interestingly, the transition goes along with only a minor change of the molecular arrangement on the *nanoscale*, as we show with a µLEED (micro diffraction) analysis.

2

Experimental

In this chapter, we will introduce the experimental details. First, we will describe the low energy electron microscope (LEEM) that was used to perform the experiments presented in this work. Following that, we will introduce methods to correct the LEEM images and micro low energy electron diffraction (μLEED) patterns for inhomogeneous backgrounds. A major concern when working with molecular layers is electron induced damage. Therefore, we examined the potential of electron induced damage of the 4,4'-biphenyldicarboxylic acid (BDA) layers on Cu(001) under different conditions. Finally, the methods used for preparation of the atomically clean and flat surfaces are introduced.

2.1 Low Energy Electron Microscopy

The experiments presented in this work were all performed in the same Low Energy Electron Microscope (LEEM). LEEM is a powerful technique to visualize in-situ processes on surfaces, using slow reflected electrons for imaging. Since slow electrons interact only with topmost layers of a surface, the technique is extremely surface sensitive. Typical applications for LEEM are the visualization of surface phase transitions and thin film growth. An advantage of LEEM is, that the imaging electron beam is not scanned across the sample, like for example in scanning electron microscope (SEM), but the surface is illuminated simultaneously, like in a transmission electron microscope (TEM). Therefore, the frame rate is only limited by the video camera that is capturing the images and the intensity of the probing beam. The idea of such an electron microscope is relatively old and the first attempts to build one date back to the 60s of the last century [30]. However, it was not until the 80s that a first working instrument was demonstrated by Telieps and Bauer [31].

In Bauers' LEEM design [32], electrons emitted from an electron gun (typically a LaB_6 field emitter) are accelerated to a high energy (10-20 keV). The high energy is necessary to be able to use conventional electron optics. The electron beam is shaped by a set of condenser lenses and subsequently passing a 60° magnetic beam splitter, which deflects the beam on a trajectory towards the surface of the sample. An objective lens focuses the beam onto the surface. While the objective lens is on ground potential, the sample is at the same high potential as the electron gun, plus a small voltage difference, which is called start voltage. Due to the potential difference between the grounded objective and sample, incoming electrons are decelerated in front of the surface to an energy defined by the start voltage and the work function difference between sample and electron gun material. The reflected electrons are re-accelerated back to high energies (10-20 keV) and pass objective lens and magnetic beam splitter a second time in reverse trajectory. All electrons that left the sample under the same angle are focused in the back focal plane of the objective lens, where they form a diffraction pattern.

2.1.1 Measurement modes

In the bright-field mode of the instrument, the specular diffraction spot is selected with a contrast aperture (see Fig. 2.2) and used to form a real space image of the surface on the screen. An exemplary image of this mode is presented in Fig. 2.1. The image shows a Cu(001) surface which is partially
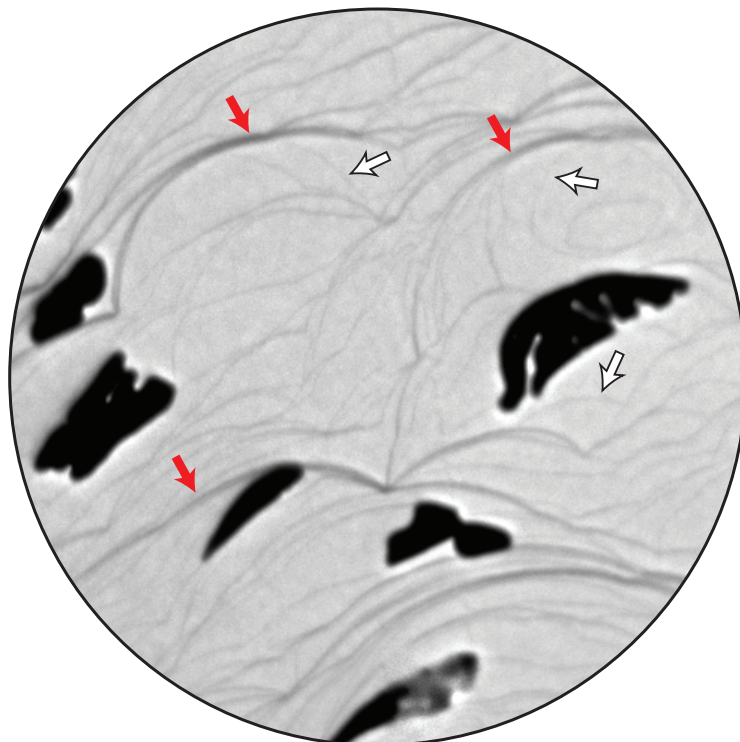
Figure 2.1: Example LEEM image. Cu(001) surface covered with BDA domains at a Field of View (FoV) of 15 μm. Light areas are Cu terraces (filled with a dilute phase of BDA molecules), dark islands are BDA c(8×8) domains (see Chapters 3 - 6). The thinnest dark lines (white arrows) are Cu single steps, thicker lines (red arrows) are step bunches.

covered with BDA domains. The light gray areas are Cu terraces, the dark areas are BDA domains and the thin dark lines are Cu steps. The contrast between the Cu terraces and the BDA domains is due to different electron reflectivities, which arise from differences of the electronic and crystalline structure. The contrast depends strongly on the electron energy, i.e., start voltage. The steps are visible due to phase contrast: electrons reflected from the terraces on both sides of a step have a different phase due to the path difference, which results in destructive interference. A third contrast mechanism is caused by diffuse scattering from a dilute species adsorbed at random sites [33, 34, 35]. Electrons are scattered by the adsorbate into a trajectory out of the specular beam direction and filtered out by the contrast aperture, thus reducing the measured intensity on the terrace [36]. This intensity change was used in Chapters 3-6 to measure in-situ the density in a diluted BDA phase on the Cu terraces.

In the μLEED mode of the instrument, the contrast aperture is removed from the beam path and the diffraction plane is projected onto the screen. By inserting an illumination aperture into the incoming beam path (see Fig. 2.2), we can restrict the area which is illuminated by electrons on the surface down to a circle with a diameter of 1.4 μm. In this way, it is possible to

relate directly real space with crystal structure information. This is especially useful, if several different crystalline domains coexist on the surface, which in a conventional LEED pattern would all overlap and may be difficult or even impossible to disentangle.
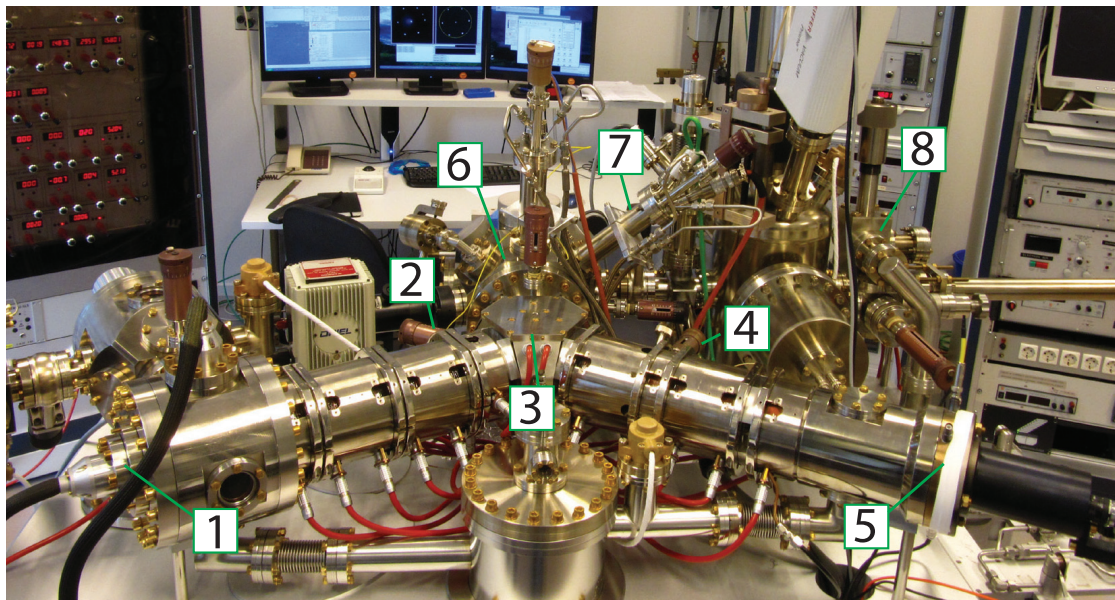
Figure 2.2: Picture of the LEEM system in which the experiments presented here were performed. 1) electron gun 2) illumination aperture 3) magnetic beam splitter 4) contrast aperture 5) screen with camera 6) main (sample) chamber 7) BDA evaporator 8) preparation chamber with load lock.

2.1.2 LEEM instrumentation

The experiments were performed in a commercial Elmitec LEEM III system, which is based on Bauer's original LEEM design [31, 32]. A picture of the instrument is shown in Fig. 2.2. The system consists of three ultra-high vacuum (UHV) chambers separated by gate valves: column, main chamber and preparation chamber. All chambers are pumped by a combination of ion-pumps and titanium sublimation pumps to avoid noise from moving pump parts. An exception is the preparation chamber, which is additionally pumped by a magnetically levitated turbopump for pumping the large gas loads needed during surface preparation. The turbopump is separated with a gate valve and can be turned off during imaging to decrease the vibrational noise level. The preparation chamber contains a load lock and facilities for ion-sputtering and sample heating. In the main chamber, six ports for evaporators are available. Each port is pointing towards the sample during imaging allowing the in-situ observation of thin-film growth. BDA (purity > 0.97, TCI Europe, CAS: 787-70-2) was deposited from a commercially

available organic material effusion cell, which was held at temperatures between 443 K and 483 K. The base pressure of the main chamber was around 1×10^{-10} mbar. After degassing the BDA evaporator thoroughly at operating temperatures (>24 hours), the pressure did not increase noticeable from the base pressure during BDA deposition experiments.

2.2 LEEM and µLEED image correction

Bright-field image correction

The screen in most LEEM systems, and in ours, is a combination of micro-channel plates (MCP), a fluorescent screen and a high resolution camera [31, 32]. While this combination is very sensitive to small electron currents, there are also major drawbacks. Different areas of the channel plates have different thicknesses, which give rise to different amplification factors, leading to large contrast gradients in the LEEM images. The plates are also very prone to damage, either by exposure to air or bleaching by electrons. This may result in large defects, or even cracks, that appear completely dark. These defects are not only annoying for their appearance, but also interfere with image analysis, e.g. thresholding to extract feature sizes. However, correcting for most of the defects and the inhomogeneities is actually straightforward: The image intensity *Im(u,v)* of each pixel *(u,v)* is given by the unamplified image intensity *F(u,v)* multiplied with the amplification factor *A(u,v)* of the MCP at that pixel. What we are really interested in, is only the original intensity distribution *F(u,v)*. To obtain it, we need to do a pixel by pixel division of *Im(u,v)* by *A(u,v)*:

$$F(u,v) = Im(u,v)/A(u,v) \tag{2.1}$$

For this operation, we need to know amplification factor *A(u,v)* of the channel-plates. We can get *A(u,v,)* from an image of a featureless, flat surface with no steps in the field of view - or alternatively by imaging a clean surface in mirror mode (negative electron energies). In mirror mode, the image contrast is formed by long ranging differences of the surface work function. For a well aligned electron beam and a clean surface, *F* is then constant over the entire image, and the measured image *Im(u,v)* is simply proportional to *A(u,v)*. With this reference image, it is straightforward to correct all other images using Eq. 2.1.

Figure 2.3 shows an example of this operation for an image of a clean Ir(111) surface with a field of view of 10 µm. The defect in the channel-
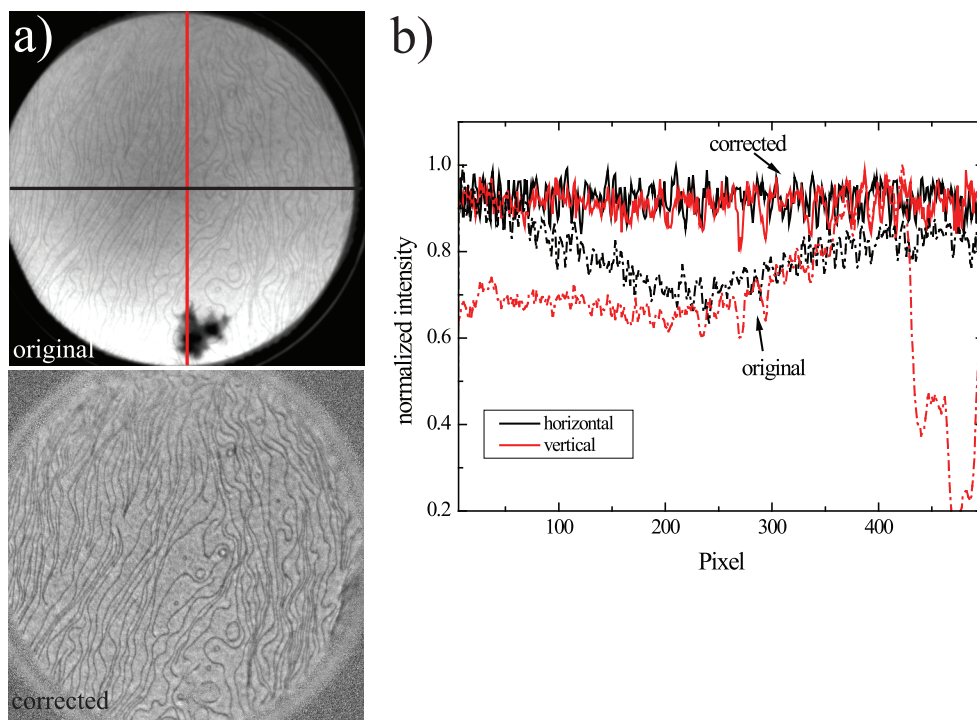
Figure 2.3: **(a)** Original (top) and background corrected (bottom) bright-field LEEM images of Ir(111). The Field of view is 10 μm and the electron energy is 2.5 eV. Note, that the damaged part of the channel plates in the lower part of the image disappeared almost completely in the corrected image. **(b)** Line profiles along the horizontal and vertical directions indicated in the original LEEM image. The intensities are normalized to the maximum value.

plates visible in the lower part of the original image disappeared completely in the corrected image. Though, the noise in this region slightly increased, due to the smaller dynamic range of the detector there. The line profiles in the same figure show that in the original the intensity differs by as much as 30% from bottom to top. This background is completely removed in the corrected image.

μLEED background correction

μLEED patterns recorded in a LEEM setup, that is not energy filtered, typically suffer from a different effect: secondary electrons (inelastically scattered electrons) form a large diffuse intensity cloud. The center and size of the secondary cloud varies with energy. Unless the LEEM is equipped with an imaging energy analyzer (SPELEEM), there is no way to separate the secondaries from the diffracted electrons experimentally. While there is some information in the amount and distribution of the secondaries, they usually distract from the important information, which is the diffraction pattern.

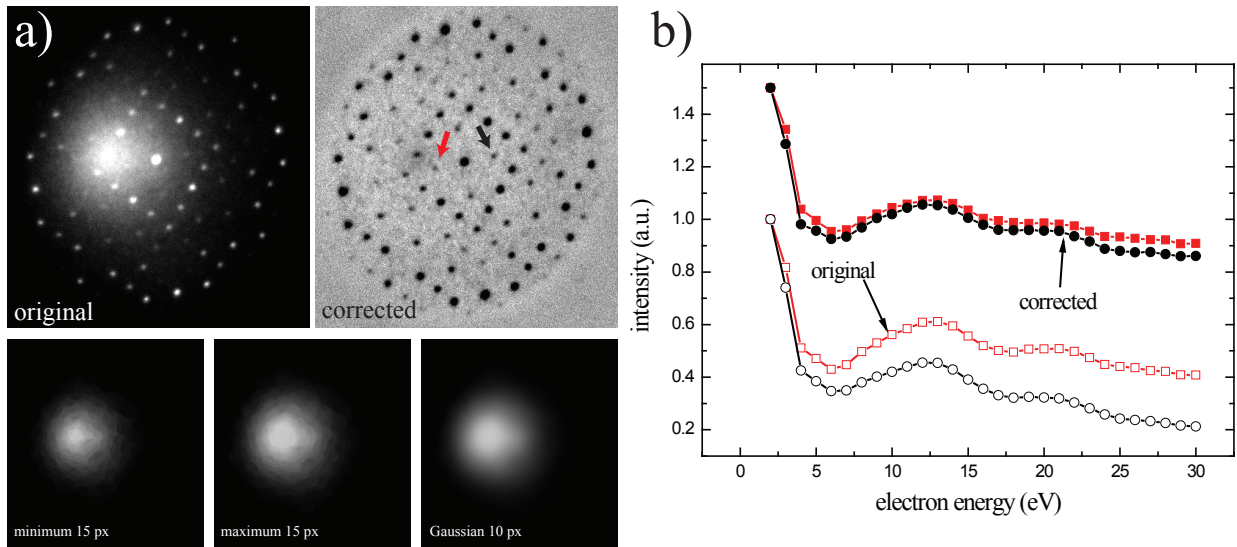Figure 2.4: **(a) Top:** Original and corrected μLEED patterns of crystalline 4,4-biphenyldicarboxylic acid domains on Cu(001). Beam energy is 29 eV. **Bottom:** Steps in generating the background image. First, a minimum filter (15 pixels) is applied to isolate the secondary intensity, followed by the reverse operation, and finally a Gaussian filter (10 pixels) to smooth the background. **(b)** Spot intensity versus electron energy (LEED IV) curves of the two LEED spots marked with red and black arrows respectively. An offset was added to the corrected LEED IV curves for clarity.

To remove the secondaries from the μLEED patterns, we first need to separate them from the diffraction spots. That means, we need to find a background image that only contains the secondaries. Since the background is moving with energy and also depends on alignment, each μLEED image needs a different background. The solution is to generate a background from the pattern itself by applying a series of simple filters. The first step is to isolate the secondary cloud from the LEED spots, which is easily accomplished with a minimum filter. This filter replaces each pixel value with the minimum value found in a defined radius around it. The radius should be chosen according to the size of the LEED spots. Usually a radius of 15-20 pixels was sufficient. By doing the reverse operation with a maximum filter of same radius, and by applying a Gaussian image filter for smoothing, we end up with a background image containing only the secondary electrons (see Fig. 2.4(a)). Correcting the original LEED pattern using Eq. 2.1 results in almost complete removal of the secondary cloud.

An example of the correction procedure is shown in Fig. 2.4(a) for the μLEED pattern obtained from 4,4-biphenyldicarboxylic acid domains on Cu(001), which have a c(8×8) superstructure (see Chapters 3-6). A secondary cloud is obscuring a large part of the original pattern. This cloud is almost completely removed after the background correction, and even weak

spots become clearly visible. Also, equivalent spots have almost equal intensity, as can be seen in the spot intensity versus electron energy (LEED IV) curves in Fig. 2.4(b).

2.3 Electron beam induced damage to BDA films

Possible damage of the BDA structure induced by the probing electrons was a major concern in this study. The energy of the electrons is extremely low with only a few eV and at first sight one would expect that the damage induced to the molecular films is minimal. However, especially this low energy can be problematic, since it is close to typical values of the HOMO-LUMO gap and potentially at vibrational molecular resonances. Molecules can get into an electronically excited state, making them more reactive. This can both destabilize the weak intermolecular hydrogen bonds, or may even result in the decomposition of molecules. How the molecules interact exactly with low energy electrons is probably a topic in itself and would require different instrumentation.

All experiments were performed with a $25\,\mu\mathrm{m}$ illumination aperture to limit the area exposed to electrons. Any electron induced damage is then apparent at the edge of this area as a sudden change of contrast, island density, size or shape. With the electron energy ($2\,\mathrm{eV}$) used in most of the experiments presented in this thesis, this was never observed.

To further investigate potential beam damage, we did the following test: We grew large BDA domains on Cu(001) at $390\,\mathrm{K}$ (see Chapter 5) and exposed them to equal amounts of electrons of different energy, ranging from $2.0\,\mathrm{eV}$ to $3.5\,\mathrm{eV}$. An estimate of the total dose gave about 10^5 electrons per molecule in the c(8×8) structure at a flux of 40 electrons per molecule and second. The dose is comparable to the dose during a typical experiment. The resulting damage after exposure to electrons of different energies is illustrated in Fig. 2.5. After exposure to $2.0\,\mathrm{eV}$ and $2.5\,\mathrm{eV}$ electrons, no damage is observed. The domains appear regular and have straight and well defined boundaries (compare also to LEEM images shown in Chapters 3 to 6). The size of the domains decreased slightly, however, this was not related to the electron exposure, but caused by a slight temperature increase during measuring. After exposure to electrons with a higher energy of $3.0\,\mathrm{eV}$ and $3.5\,\mathrm{eV}$, the domain borders become more irregular, almost fuzzy. This points at a reduced intermolecular interaction, i.e., breaking of the hydrogen bonds between molecules.
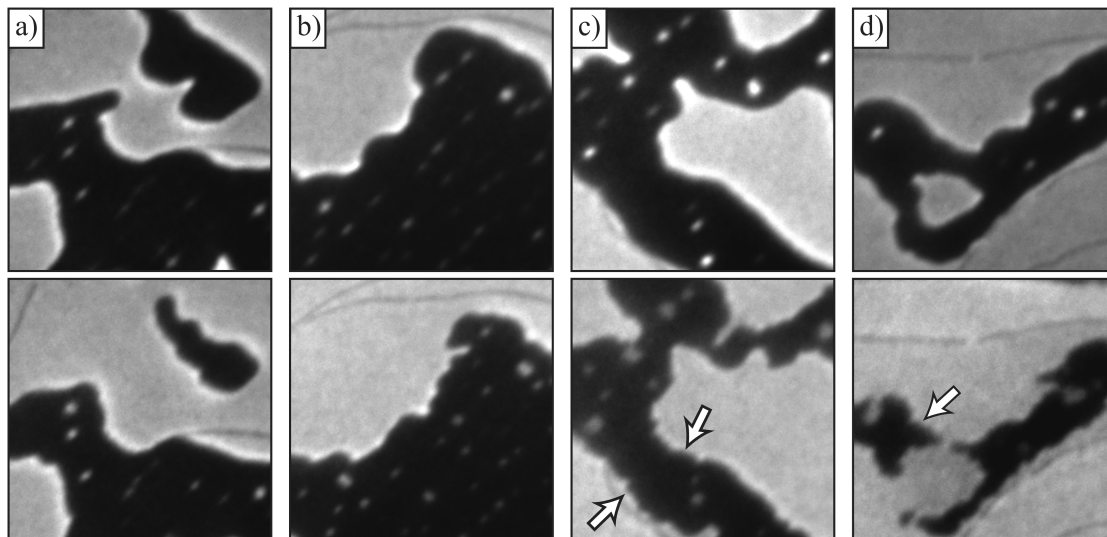
Figure 2.5: LEEM snapshots of BDA c(8×8) domains grown on Cu(001) at 390 K (top row) and exposed to equal electron doses of about 10^5 electrons per molecule (bottom row) with **(a)** 2.0 eV, **(b)** 2.5 eV, **(c)** 3.0 eV and **(d)** 3.5 eV. Note, how the domain edges become more and more irregular after exposure to electrons with a higher energy (arrows). The temperature was slightly above the growth temperature, which gave rise to an additional shrinking of the domains not related to the electron exposure (All images 1 μm FOV).

The damage becomes more obvious, if we induce more mass transport from the c(8×8) domains into the diluted phase by a larger change of sample temperature. In Fig. 2.6, we illuminated a large BDA domain grown at 383 K (Fig. 2.6(a)) with 3 eV electrons while increasing the temperature to 394 K. The total dose of electrons per molecule was about twice that in Fig. 2.5 with the same electron flux. The irregular, fuzzy domain edges after exposure (Fig. 2.6(b)) are very clear here, mainly because the interface moved considerably more due to the increase in temperature. The Cu terrace, on which the BDA domain is located, appears much darker than the surrounding terraces in Fig. 2.6(b), this includes also the parts of the terrace that were not initially covered by the domain. This must be attributed to an increased density in the dilute 2D phase with increasing temperature, as described in Chapters 3-6. As we will show in Chapter 5, Cu steps are permeable for BDA molecules. Under the influence of 3 eV electrons, this is apparently not the case. One explanation is, that the electrons produce excited molecules or radicals that interact strongly with the steps, decorating them even at elevated temperatures. If the steps are decorated, they will also be impermeable for intact BDA molecules. Upon reducing the substrate temperature, BDA domains reappear at a higher density on the dark terrace. However, with ragged island shapes, suggesting many pinning sites, e.g., broken or immobilized molecules. The μLEED pattern obtained from the damaged ar-
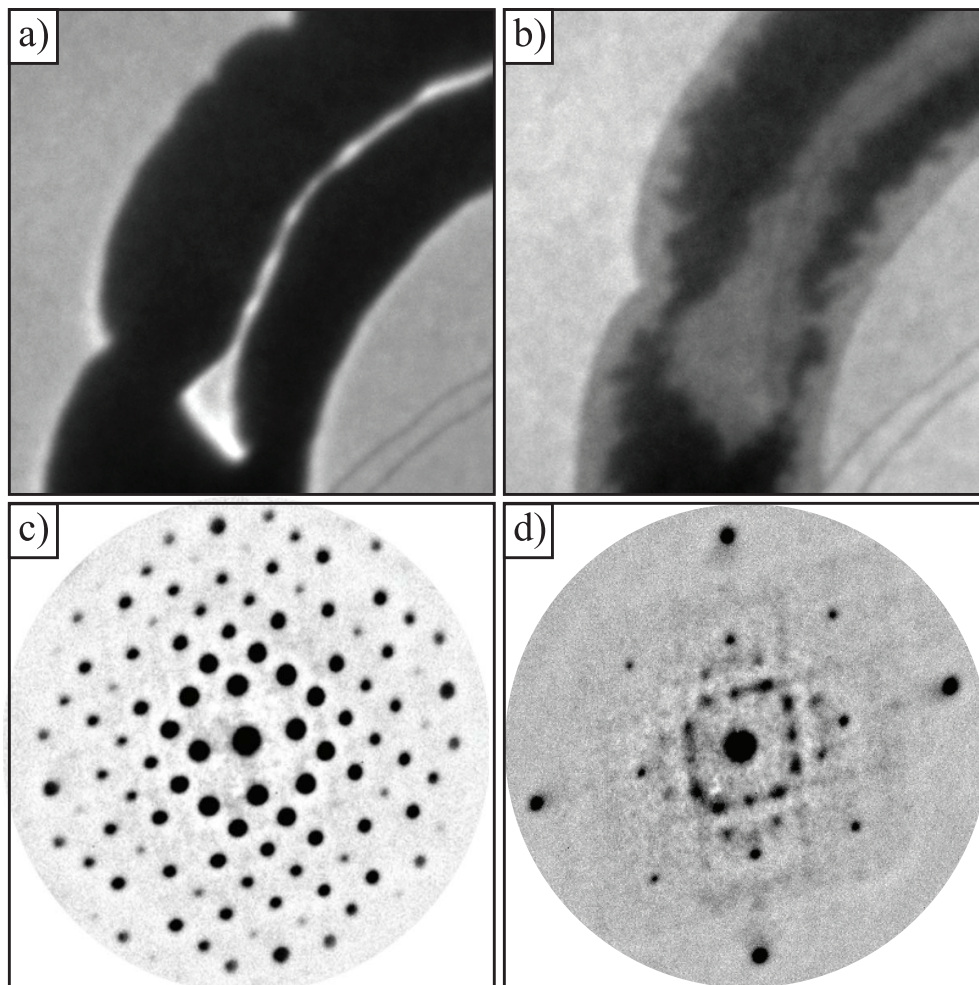
Figure 2.6: LEEM snapshots of a BDA c(8×8) domain grown on Cu(001) at 383 K **(a)** and heated to 394 K **(b)** while imaged with 3 eV electrons. The total dose of electrons was twice that in Fig. 2.5 (FOV 1 μm). Images **(c)** and **(d)** show cumulative (3 eV to 28 eV) μLEED patterns obtained from an intact c(8×8) structure, and from the electron damaged patches in (b).

eas (Fig. 2.6(d)) shows also a structural change, which was induced by the electrons. An analysis of the structure is not straightforward; we cannot even say whether the molecules are still intact and merely rearrange, or if they decomposed into unknown fragments. It is also possible, that a polymerization reaction was induced by the electrons. The domains outside of the illuminated area showed no beam induced damage, in particular they featured straight and clearly defined domain boundaries.

In conclusion, exposure of the molecular layers to low energy electrons may induce damage. However, the damage depends strongly on the electron energy. While we didn't observe damage after exposure to electrons with energies between 2 and 2.5 eV, already increasing the energy further to 3 eV leads to visible damage. The doses necessary to observe strong damage are

relatively large and in no way impede experiments, as long as the possibility of beam damage is kept in mind and the illuminated area is changed from time to time.

2.4 Surface preparation

For the experiments in Chapters 3-6, a Cu(001) single crystal with a miscut angle less than 0.1° was used [37]. Prior to mounting, it was annealed at about 1170 K in an Ar-H$_2$ mixture for a prolonged period to deplete the bulk of the crystal from sulfur contamination. After insertion into the LEEM, the sample was further cleaned by cycles of sputtering and annealing. In a previous study [38], carbon proved to be a particularly persistent contamination. That is because of the notorious low carbon sputter yield with Ar-sputtering and the deposition of fresh carbon during each experiment. Oxygen treatment is not an option, due to the possibility of bulk oxide formation. An elegant and very effective solution is sputtering with hydrogen [39] in combination with argon sputtering and annealing at 900 K. This typically allowed the preparation of a clean surface within a few hours. For the study of BDA on Au(111) (Chapter 7), a Au(111) single crystal was used. The surface was prepared by prolonged cycles of sputtering with argon and annealing at 700-800 K.

3

Phase transformations of BDA on Cu(001)

The growth and structure of 4,4'-biphenyldicarboxylic acid (BDA) on Cu(001) at temperatures between $300\,\mathrm{K}$ and $400\,\mathrm{K}$ was studied by LEEM and μ-LEED. First, the adsorbed BDA molecules form a disordered dilute phase. Once this phase reaches a sufficiently high density, a crystalline phase nucleates, in which the molecules form a hydrogen-bonded two-dimensional (2D) supramolecular c(8×8) network. By a careful analysis of the bright-field image intensity we can measure the density in the dilute phase, which is up to 40% of that in the crystalline phase. From the respective equilibrium densities at different temperatures we determine the 2D phase diagram and extract a cohesive energy of $0.35\,\mathrm{eV}$. We also analyzed the island decay behavior and estimated the BDA molecule diffusion constants. Steps are found to be highly transparent for diffusing BDA molecules. In the temperature range of $362\,\mathrm{K}$ to $400\,\mathrm{K}$ we find chemical diffusion constants between $650\,\mathrm{nm^2\,s^{-1}}$ and $1300\,\mathrm{nm^2\,s^{-1}}$.

3.1 Introduction

The self-assembly of organic molecules into large supramolecular networks is a promising method for the fabrication of novel nanoscale structures [7, 40, 5, 4]. Hydrogen bonds, which can be highly selective, play an important role in the self-assembly process. One of the more frequently studied building blocks are benzoic acid groups [41, 42, 11, 12, 38, 43, 16, 44]. It has been reported that benzoic acids adsorb on Cu(001) as deprotonated carboxylate species [41, 42, 11]. 4,4'-biphenyldicarboxylic acid (BDA) is an organic molecule with two phenyl rings and two functional carboxyl end groups. It is a non-chiral molecule that is 1.3 nm in length (see Fig. 3.1). On Cu(001), the molecules adsorb in a flat-lying configuration. Re-evaporation (or desorption) into vacuum does not occur, the molecules decompose on the surface above 450 K. Below these temperatures, BDA exists in two phases on Cu(001): a dilute phase and a two-dimensional (2D) crystalline phase which nucleates from the dilute phase [38]. In the crystalline phase the molecules form a well-ordered, square network with a c(8×8) superstructure, as was found by scanning tunneling microscopy (STM) and μLEED [12, 38]. An example of the μ-diffraction pattern obtained from the structure is shown in Fig. 3.2. Adjacent molecules are rotated by 90° and the lateral molecule-molecule interaction is governed by hydrogen bonds formed between the phenyl rings of one molecule and the carboxylate end group of the next molecule (see Fig. 3.1).
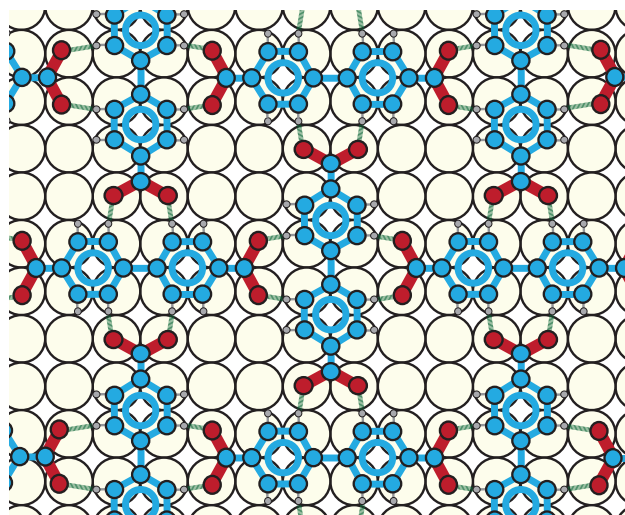

Figure 3.1: Schematic arrangement of the BDA molecules in the c(8×8) domains on Cu(001). The blue (light gray), red (dark gray), and smaller gray dots represent C atoms, O atoms, and H atoms, respectively.

Calculations show that the two benzene rings constituting the single BDA molecule are twisted along the long axis of the molecule in vacuum. While

for BDA adsorbed on, e.g. Au(111), both rings are expected to be in-plane [43], we found in a previous µLEED study, that they are also twisted on Cu(001) [38].

The strength of the molecule-molecule interaction as well as the diffusion constant are key ingredients to understand and control the self-assembly process and important input parameters for simulations. However, they are difficult quantities to access experimentally. It is also not clear how the underlying substrate influences the interaction strength. In this paper, we will show how low energy electron microscopy (LEEM) can be used to measure the density in the disordered phase by analyzing the local electron reflectivity. This allows us to construct a 2D phase diagram, which provides a direct route to determine the cohesive energy of a molecule in the 2D network. Additionally, we will study the decay of the domains using the measured mean densities in the dilute phase.

a)   b)
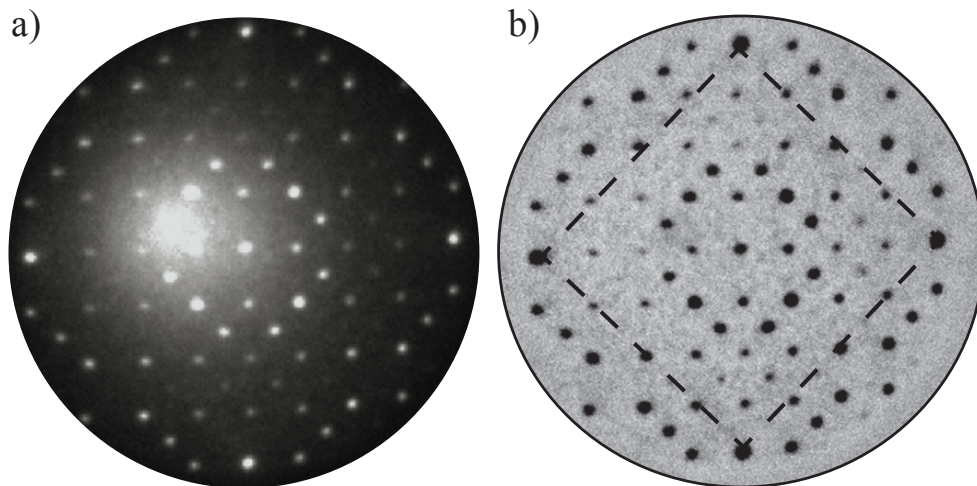
Figure 3.2: µLEED pattern of the BDA domains measured at an electron energy of 27 eV. The dashed lines connect the Cu(001) first-order spots. **(a)** Measured and **(b)** background corrected pattern (see Chapter 2).

3.2 Experimental

Experiments were performed in an Elmitec LEEM III low energy electron microscope with a base pressure of about 1×10^{-10} mbar. A Cu(001) single crystal with a miscut angle of less than 0.1 degrees was used [37]. To deplete the bulk of the crystal from impurities like carbon and, especially, sulfur it was annealed at 900° C under a flow of an Ar-H$_2$ gas at atmospheric pressure for 48 hours. After transferring the crystal to the LEEM the surface was further cleaned by cycles of sputtering with atomic hydrogen [39], sputtering

with argon ions and annealing at 900 K. This method allowed us to prepare clean surfaces with sharp LEED spots, large terraces and smooth step lines.

Commercially available BDA in powder form (purity > 97%, TCI Europe, CAS: 787-70-2) was deposited from a Knudsen cell type source. Before the experiments, the BDA-source was carefully degassed. Throughout the experiments, the source was held at one of two temperatures. The corresponding deposition rates differ by a factor of ∼4. During deposition, the Cu(001) surface was held at constant temperatures between 300 K and 420 K.

A 25 μm illumination aperture was used to limit the illuminated area on the surface. Any potential influence of the electron beam on the BDA behavior, e.g. differences in island size distribution and nucleation density, would therefore become visible at the edge of the illuminated area, which was never observed under the imaging conditions selected here.

3.3 Measurement of the density in the dilute phase

3.3.1 BDA induced change of electron reflectivity

The measurement of the density in a dilute 2D surface phase by the attenuation of a scattering beam is a well-known technique. For example, He scattering was used to measure the 2D gas to 2D gas + 2D solid transition of Xe on Pt(111) [45, 46, 36, 47]. Recently, the technique was also applied in LEEM, where the real-space image helps in distinguishing between a solid/liquid and disordered phase. Examples are the growth of Ag on W(110) [33] and C on Ru(0001) and Ir(111) [35, 34]. In LEEM, a dilute or 2D gas phase leads to a decrease in image intensity of the substrate terraces. In previous LEEM studies, this resulted in a drop of image intensity that is proportional to the local adatom concentration. The sensitivity of this method is up to 10^{-3} ML, depending on the system investigated [33].

To have maximum sensitivity, it is necessary to know how the BDA in the dilute phase changes the electron reflectivity of the Cu(001) surface. Figure 3.3(a) shows LEEM IV curves for the clean Cu(001) surface and for the surface covered with BDA molecules in the dilute phase at a coverage before island nucleation (see LEEM image in Fig. 3.3). Both curves were normalized to the intensity at negative energy < 0 eV. In the region between 1.5 and 3.5 eV the relative difference between the curves is largest. We used an electron energy of 2 eV for further imaging. No density gradients can be observed, close to a BDA domain or on different Cu terraces. The
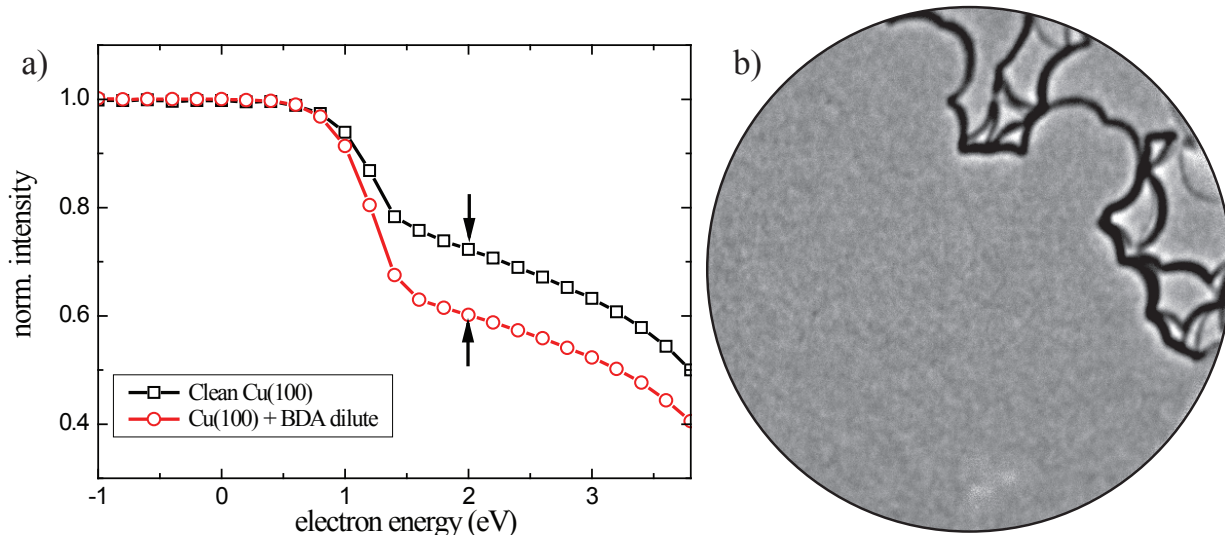
Figure 3.3: **(a)** LEEM IV curves measured on a clean Cu(001) terrace and on a terrace covered with BDA in the dilute phase. The BDA coverage is approximately 0.01 ML, expressed in occupied Cu lattice sites. Arrows indicate the energy used for imaging, 2 eV. **(b)** LEEM image of a large Cu terrace with BDA gas (Field of View (FoV) 4 µm). The molecules give rise to a homogeneous decrease of the image intensity. No density gradients can be observed. The lighter area in the lower part of the image is due to a defect in the MCP detector.

BDA molecules in the 2D dilute phase give rise to a homogeneous change in intensity covering all parts of the surface.

Next, we need to understand this intensity change as a function of coverage. For this we tracked the bright field intensity of the Cu terraces for different conditions at an electron energy of 2 eV while depositing molecules. In Fig. 3.4 we show the evolution of the intensity of two representative experiments. The experiments were done with deposition rates, which differ by about a factor of 4, as well as with different substrate temperatures (353 K and 368 K respectively). We emphasize that the initial slope of such a take-up curve only depends on deposition rate and not on the substrate temperature. At t = 0 s the shutter of the source is opened and the intensities are normalized to this point. After opening the shutter the normalized intensities $\frac{I}{I_0}$ start to drop linearly with time. The slope depends on the source temperature; the higher setting leads to a larger slope. The change in intensity is proportional to the density of molecules on the surface. At t = 750 s (black circles) and 2000 s (red squares) BDA domains start to nucleate from the dilute phase. The domains mainly nucleate on the Cu terraces (homonucleation) and are blocked in their growth by both upward and downward Cu steps (see Fig. 3.5). The nucleation is accompanied by a sharp transition in the intensity on the terraces. Because of the nucleation barrier the dilute phase was supersaturated during nucleation [48]. This results in an
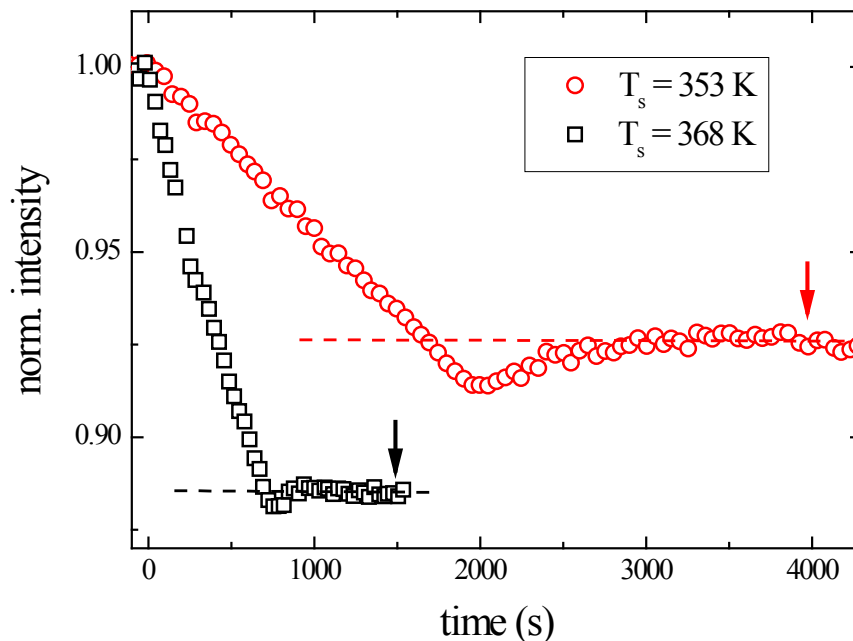
Figure 3.4: Normalized intensity change measured on the Cu terrace (far away from nucleated BDA domains) during deposition of BDA at 353 K and 368 K. After the shutter is opened, the intensity drops linearly until BDA islands nucleate at 750 s (368 K) and 2000 s (353 K), respectively. The two curves were obtained at different deposition rates. We verified that the initial slope of the decay curves at fixed deposition rate does not depend on the substrate temperature. The shutter is closed at t = 3900 s (353 K) and t = 1500 s (368 K), respectively.
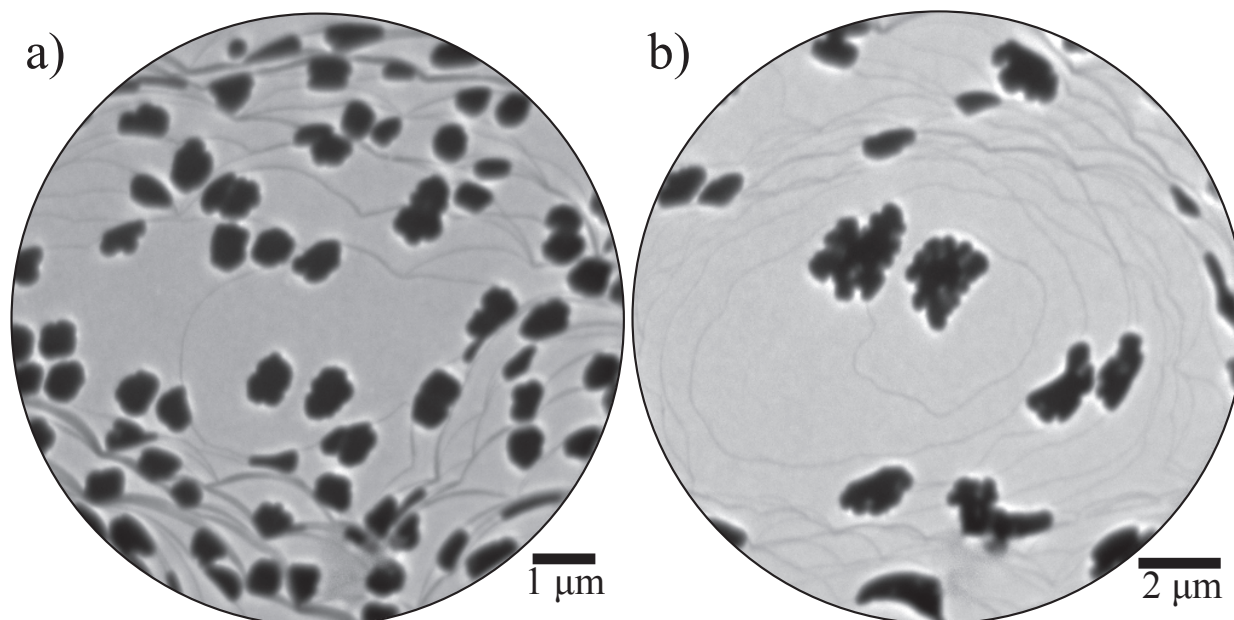
Figure 3.5: LEEM images corresponding to the experiment in Fig. 3.4. The images show the island configuration at the end of the deposition for **(a)** 353 K and **(b)** 368 K. By averaging several images at different positions we find that the islands cover 11% (a) and 10% (b) of the surface.

increase of intensity after nucleation when BDA domains grow not only from the molecules that arrive from the evaporator, but also at the expense of the supersaturation on the bare terraces. After some minutes the intensity stabilizes at a constant value, which means that a dynamic equilibrium is reached. This value is also close to the true equilibrium, and thus low supersaturation, since no change in intensity is observed when the shutter is closed at t = 3900 s (353 K) and t = 1500 s (368 K)).

Due to the statistical overlap of the diffuse scattering cross section of individual scatterers the intensity should in principle decay exponentially [36, 46, 47]. The slope is given by:

$$d(I/I_0) = -\Sigma exp(-\Sigma n)dn \tag{3.1}$$

where Σ is the BDA scattering cross section and n is the BDA density. Since in this case we are covering only small Σn values up to 0.15, the exponential behavior is approximated well by a linear uptake curve. In the crystalline phase each molecule covers an area of $1.04\,\text{nm}^2$ and the corresponding density is therefore $0.96\,\text{nm}^{-2}$ or one molecule per 16 Cu atoms. For the remainder of the article we will express coverage (or density) as the fraction of occupied Cu-lattice sites. A closed c(8×8) layer corresponds to a coverage of $0.0625\,\text{ML}$.

It is now straightforward to determine the cross section for diffuse scattering, Σ, introduced in Eq. 3.1. The final level of the normalized intensity in Fig. 3.4 is determined by the density of the dilute phase, n_d, corresponding to the 2D vapor, and Σ. This level has been reached first at time t_1, where all deposited molecules belong to the dilute phase. At the end of the experiment at time t_2 a fractional area A_c is covered with the condensed phase with a higher density $n_c = 0.0625$. Assuming that all molecules that hit the surface are incorporated in the film leads to the situation in which $n_d(A_c + t_2/t_1 - 1)$ molecules contribute to an area A_c with density n_c. The resulting value for n_d equals $0.0625 A_c/(A_c + t_2/t_1 - 1)$. Consequently, $\Sigma = -\ln(I(t_2)/I_0)/n_d$, or $\Sigma \approx [1 - I(t_2)/I_0]/n_d$, with n_d being approximately an order of magnitude smaller than n_c for the data shown in Fig. 3.4. With $A_c = 0.11 \pm 0.01$ and 0.10 ± 0.02 for $T = 353$ and $368\,\text{K}$, respectively, the resulting mean value for $\Sigma = 1.2 \pm 0.1\,\text{nm}^2$. In principle, Σ depends on the energy of the probing electrons and by coincidence the value at $2\,\text{eV}$ is close to the actual area of the molecule. This implies that statistical overlap is negligible and we can, to a good approximation, use a linear relationship between intensity and

density. The density in the dilute phase at time t is then given through the intensity I(t) by

$$\theta_{BDA}(t) = 0.052 * \frac{I(0) - I(t)}{I(0)} \, \text{ML}, \tag{3.2}$$

where $I(0)$ is the intensity when the shutter was opened at t = 0 s. A drift of the instrument (cathode emission current or alignment) will change this initial intensity and thus change the normalization. One might expect that the intensity of the BDA c(8×8) gives a possibility to normalize the intensity, however due to field distortion at the island's perimeter this intensity is not uniform and is decreasing towards the island center.

With this result we return to Fig. 3.4 for a moment. Nucleation occurs at coverages of about 4.5×10^{-3} ML (red curve, 353 K) and 6.3×10^{-3} ML (black curve, 368 K). Compared to values common in epitaxial growth of, e.g. metals, these values are very large. The relative densities in the dilute phase, corresponding to the 2D vapor pressure, are up to 40% of the crystalline structure. This fortunate fact allows us to monitor the density in the dilute phase in a relatively wide temperature window. The system is already close to equilibrium, i.e. in a low supersaturation stage, where the 2D dilute phase has a high density. After nucleation, the density goes down slightly, which means that the dilute phase was significantly supersaturated during the nucleation period. Supersaturation is genuinely necessary for nucleation due to the aforementioned nucleation barrier. For an ideal 2D gas the supersaturation $\Delta\mu$ is defined as $\Delta\mu = k_B T \ln(\frac{\theta}{\theta_{eq}})$, where θ is the gas density [49, 48]. The equilibrium density θ_{eq} is almost identical to the plateau reached at the end of both curves, 3.8×10^{-3} ML and 5.9×10^{-3} ML. Taking these numbers we find maximum supersaturations of about 5 meV and 2 meV per molecule. These rather small values indicate that the system is only slightly out of equilibrium for nucleation to occur.

3.4 Part I - BDA 2D phase-diagram

In the preceding section we have determined the local molecule concentration in the dilute phase. We apply the same method now to determine the equilibrium density in the presence of large BDA domains in a temperature range from 330 K to 420 K. BDA domains were grown at different temperatures in individual experiments on freshly cleaned substrates. After growing sufficiently large islands the temperature was changed in discrete steps of
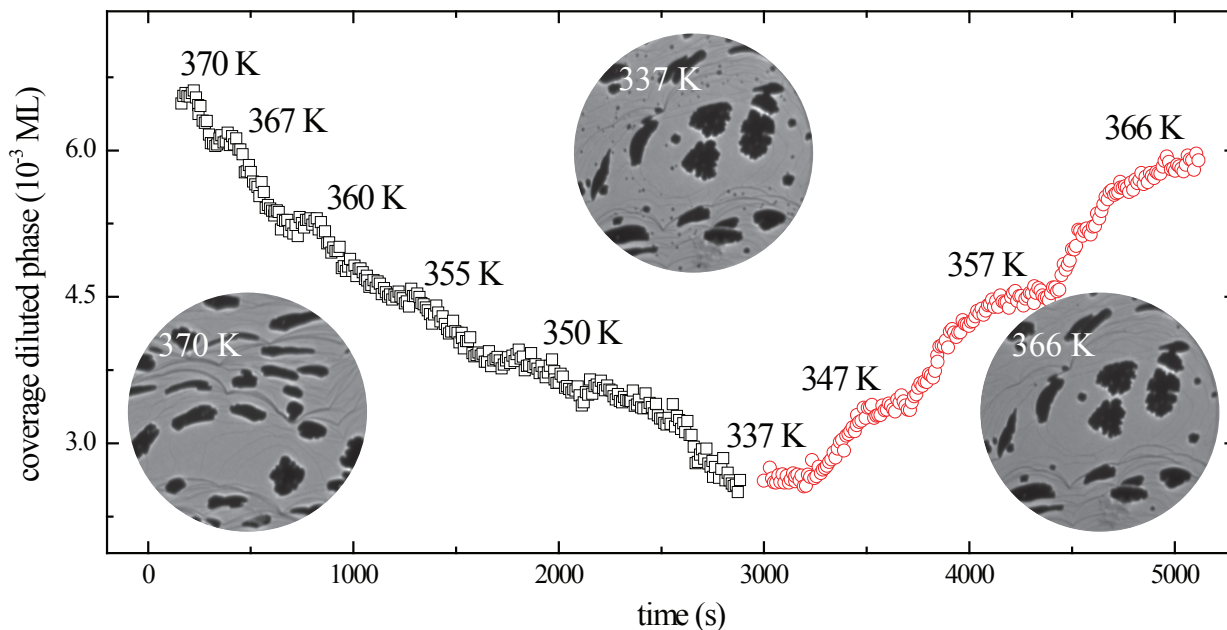
Figure 3.6: Experiment to determine the equilibrium BDA density in the dilute phase. First BDA domains were grown at 370 K. Then the sample was cooled in steps to 337 K. Next the sample was heated again in three steps. The temperature of each step is indicated in the figure. Each temperature was maintained until the intensity was constant. LEEM images show the configuration at the start of the experiment (left) after cooling down (middle) and after heating again (right); 15 μm FoV.

about 5-10 K. At each step the system was given time to reach equilibrium again. When the temperature is lowered, molecules in the dilute phase attach to existing BDA domains or nucleate to form new domains if the temperature change was too fast. Slowly a new constant density is reached and the system is in equilibrium again. We assume that the BDA islands merely act as a reservoir for molecules and have large enough curvature. The latter condition is necessary to avoid a size dependence of the equilibrium density, since domains with a small curvature will have a larger corresponding vapor pressure (Gibbs-Thomson relation). An example of such an experiment is shown in Fig. 3.6. Large BDA domains were grown at 370 K. Then the sample was cooled down in discrete steps to 337 K. Next the sample was heated again in three steps. The temperatures of each step are indicated in the figure. Each temperature was maintained until the intensity did not change anymore. The relatively long time before the density equilibrates, especially during the heating steps, shows that the molecular diffusion is rather slow. This will introduce a small error when the measured concentration is actually not yet the equilibrium value. In Fig. 3.7 we show the resulting 2D phase diagram, summarizing the data from several measurements. The data obtained for the equilibrium concentration after a temperature increase are

denoted with top-up triangles and those obtained after a temperature decrease are denoted by top-down triangles. Data points derived directly from the isothermal deposition curves, shown in Fig. 3.4, are denoted with squares. It is obvious that the data points are probing identical situations, proving that they represent thermal equilibrium data. The measured equilibrium densities lie on a line that is closely following a logarithmic curve.
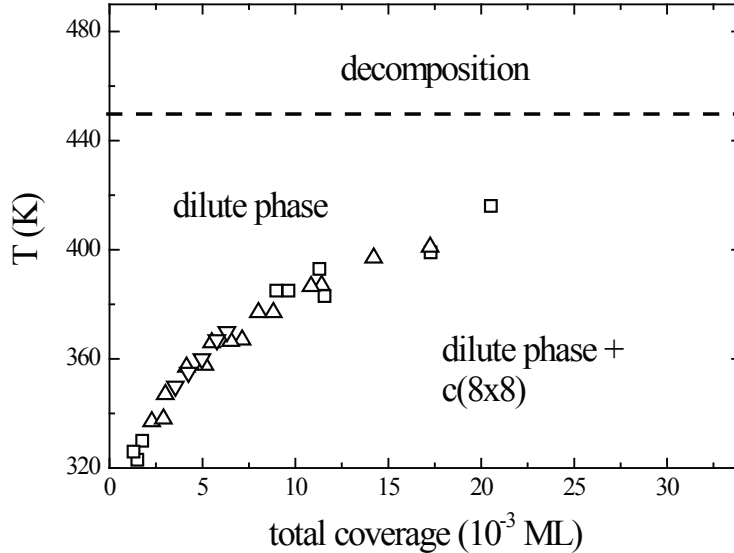
Figure 3.7: 2D phase diagram of BDA on Cu(001). Copper assisted decomposition of the molecules starts at temperatures above 450 K. Squares give the equilibrium density after growth (see Fig. 3.4), downward triangles cooling and upward triangles heating experiments (see Fig. 3.6).

On the dividing line, the chemical potential of the dilute phase μ_d and the c(8×8) phase μ_s have to be equal, meaning that no net mass transport occurs from one phase to the other. Phenyl rings have a strong affinity with fourfold hollow sites and threefold hollow sites on, respectively, *fcc* (100) and (111) surfaces [10, 50]. This would lead to the c(8×8) structure as sketched in Fig. 3.1. We will have the occupation of these sites in mind also for the molecules in the dilute phase. We emphasize, however, that this assumption is irrelevant for our further considerations, which would apply also for bridge or on-top sites. The molecules will form a lattice gas where they are free to jump between different 4-fold hollow lattice sites with a probability that is governed by the diffusion constant [51, 52, 53]. By equating the chemical potentials μ_d and μ_s, we can calculate the density in the dilute phase. Neglecting vibrational excitations and thus negating entropy in the crystalline phase, the chemical potential of an atom in the crystalline phase is equal to the (negative) cohesive energy ($\mu_s = -E_C$), the energy difference between a molecule in the solid and in the dilute phase.

In the dilute phase the chemical potential contains entropy terms and a coverage-dependent mean field interaction term $W(\theta)$:

$$\mu_d = k_B T \, ln(\frac{\theta}{1-\theta}) - k_B T \, ln(Z) + W(\theta) \tag{3.3}$$

The first term follows from occupation statistics and the second term, with Z representing the partition sum, summarizes the remaining entropy terms. The latter will contain, for example, vibrational or rotational terms. By equating μ_s and μ_d we find:

$$\frac{\theta}{1-\theta} = exp(\frac{-E_C - W(\theta)}{k_B T} + ln(Z)) \tag{3.4}$$

Plotting $ln(\frac{\theta}{1-\theta})$ versus $1/k_B T$ should therefore give a curve with a slope of $-E_C - W(\theta)$. This is done in Fig. 3.8, the data scatters along a straight line
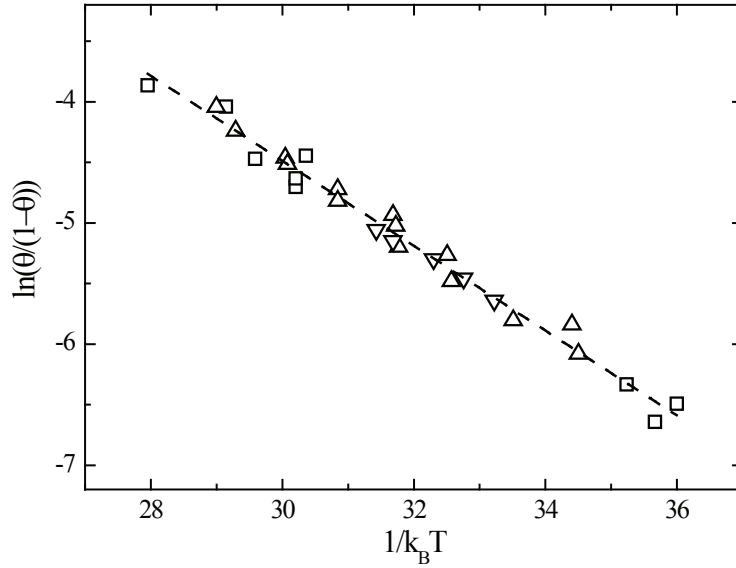
Figure 3.8: Plot of $ln(\frac{\theta}{1-\theta})$ versus $1/kT$ from Fig. 3.7. The data can be fitted with a straight line with a slope of $0.35\,\text{eV} \pm 0.03\,\text{eV}$. For the meaning of the symbols see Fig. 3.7.

with a slope of $0.35 \pm 0.03\,\text{eV}$ and with an intersection with the ordinate at $ln(Z) = 6.33$. Measurement errors arise mainly from small drifts of the total image brightness, which change the reference point of the intensity normalization. This is also limiting the resolution at low coverages (temperatures), where intensity changes of a few percent were tracked over up to half an hour.

3.4.1 Discussion on the cohesive energy

The slope in Fig. 3.8 gives us a value for $E_C + W(\theta)$. In the analysis we cannot separate the cohesive energy from the mean field interaction term. Molecules will not only interact attractively through the short ranged hydrogen bonds, but also by exclusion of lattice sites and through repulsive long ranged Coulomb forces from the negatively charged carboxylate groups. This means that the sign and coverage dependence of $W(\theta)$ are unknown. The sign might even change with coverage. However, from the quality of the straight fit we conclude that $W(\theta)$ has to be rather small. A larger value would introduce a coverage dependent slope. A good estimate for the cohesive energy is therefore given by $E_C = 0.35 \pm 0.03\,\text{eV}$.

From the temperature independent part in Fig. 3.8 we find an entropy term of $ln(Z) = 6.33$. In a simple model, i.e. a monatomic lattice gas where every gas atom occupies exactly one site and has no vibrations, $ln(Z)$ should be zero. However, the size and the structure of the molecules add entropy terms. These will contain, for example, rotational and vibrational terms which are frustrated in the crystalline phase. Also, a term that is introduced by blocking of neighboring sites through the molecules in the dilute phase contributes. In the c(8×8) phase each molecule blocks 16 lattice sites (see Fig. 3.1), while in the dilute phase one molecule blocks at least 41 sites and possibly more if we take into account the repulsion from the negatively charged carboxylate groups (see Fig. 3.9). On the other hand for larger densities the molecules will have to order, thereby reducing the number of occupied sites down to 16 in the limit of full coverage. This effect will change the configurational entropy for molecules in the dilute phase, also as a function of coverage.

The $ln(Z)$ term increases the density in the dilute phase by a factor of Z compared to a monatomic lattice gas with the same cohesive energy, . It is important to note that the large densities that we observe in the dilute phase, up to half of the density in the c(8×8), do not originate from a weak intermolecular interaction, but rather from the size and structure of the molecule.

The BDA molecules form a square 2D crystal with four nearest neighbors for each molecule. Hydrogen bonds are very short ranged, so we can assume that nearest neighbor interaction will be by far the largest contribution to the cohesive energy. Therefore, the cohesive energy is equal to the binding energy of a molecule in a kink position, which corresponds to a molecule with two nearest neighbors. This means that the strength of an individual bond between two molecules is $E_{NN} = 0.175\,\text{eV}$. The only other study
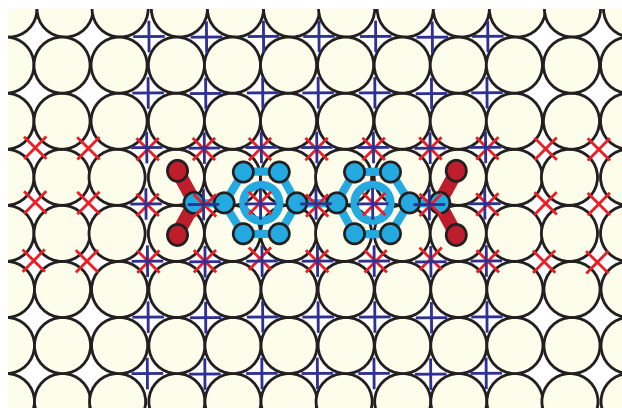
Figure 3.9: Sketch illustrating the number Cu-lattice sites blocked by one molecule assuming a hard sphere model. The center of mass on a marked lattice site cannot be occupied by another molecule. Red crosses (33) are blocked for molecules oriented parallel, blue pluses (49) for perpendicular oriented. With equal probability for parallel and perpendicular orientation we arrive at a mean number of blocked sites of 41.

that determined a comparable value for the cohesive energy of PTCDA on Ag(100) used an indirect method by fitting decay curves [54]. For this system a lower value for the cohesive energy (100 meV) was found.

In the c(8×8) structure, each bond is made by hydrogen bonds from the carboxylate group of one molecule to the two nearest carbon atoms of both phenyl rings of the neighboring molecule. The hydrogen bonds are formed by the negatively charged oxygen atoms and the positively polarized hydrogen atoms of the phenyl rings. Since carbon is only slightly more electronegative than hydrogen, the polarization will be rather small, which limits the overall hydrogen bond strength. If we treat the bond as two independent C-H··O bonds, we find a dissociation energy of 0.09 eV for each bond. This value is well in the range of a weak hydrogen bond [55], as expected for this type of bond. The hydrogen bond strength usually depends strongly on temperature and pressure, due to changing bond lengths. However, here the BDA molecules are locked in position by the underlying substrate. Ignoring the small thermal expansion of the Cu-substrate, the bond length will therefore remain constant and accordingly so will the binding strength.

From the value for the cohesive energy, we can estimate the line tension in a nearest neighbor model. In this model, the line tension per molecule is equal to one-quarter of the cohesive energy: $\gamma^* = 0.09 \pm 0.015$ eV. The actual value of the line tension will depend on the shape of the island, which can introduce a correction, on the order of 10% [56]. We will use this value for γ^* in the next part to analyze BDA island decay, which allows us to estimate the molecule diffusion constant.

31

3.5 Part II - Island decay

The decay kinetics of islands on a surface was studied extensively, and allows us to obtain information on diffusion constants and boundary energies [54, 57, 58, 59, 56, 60, 61]. Here, we will first use a classical approach to analyze the decay of small islands. With the previously obtained information on the line tension γ^* and equilibrium densities $\theta_{eq}(T)$, this allows us to estimate the diffusion constant.

Upon changing the substrate temperature we change the equilibrium condition between the dilute and crystalline phase. This leads to mass transport towards or away from the islands, and islands grow or decay as can be seen in the insets in Fig. 3.6. The driving force for the growth or decay is the difference between the actual mean density $\overline{\theta}$ and the equilibrium density θ_r of the dilute phase. Generally, θ_r will depend on the island's curvature r according to the Gibbs-Thomson relation:

$$\theta_r = \theta_\infty exp(\frac{\gamma\Omega}{kTr}), \tag{3.5}$$

where r is the island curvature, γ is the line tension, Ω is the area occupied by each molecule and θ_∞ is the equilibrium density of an infinitely large island. The change of the island area A is then given by:

$$dA/dt = -\kappa(r)(\theta_r - \overline{\theta}) \tag{3.6}$$

$$dA/dt = -\kappa(r)(\theta_\infty exp(\frac{\gamma\Omega}{kTr}) - \overline{\theta}) \tag{3.7}$$

where $\kappa(r)$ is a rate constant that contains the diffusion constant and geometry information. The decay can either be limited by the rate at which molecules diffuse away from the islands or by the detachment of molecules from the island [62, 63, 64, 65]. In the case of diffusion limited decay, the rate constant is given by: $\kappa_D = \frac{2\pi\Omega D(T)}{l_c}$. $D(T)$ is the temperature dependent diffusion constant and l_c is a screening length. Typically the expression $l_c = ln(R/r)$ is used for the screening length, where r is the islands' radius and R is the distance away from the islands' edge where θ_∞ is reached. This expression is exactly valid only for a concentric geometry, e.g. an isolated island on a large terrace. Compared to the exponential term in Eq. 3.7 it is changing only slowly with r and is typically approximated to be a constant

on the order of 1. Analytical solutions for l_c exist only for a few special geometries [59].

3.5.1 Decay of small islands - classical Ostwald theory
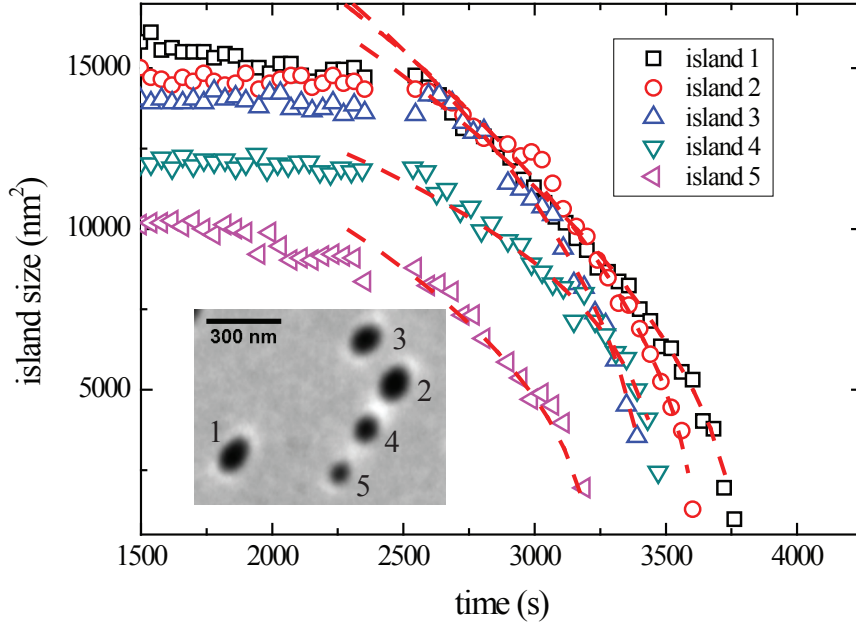
Figure 3.10: Size evolution of decaying islands at 362 K, shown in the inset. The temperature was changed from 348 K at about 2500 s and reached the final value of 362 K at about 3000 s. The red dashed lines are fits of the type $\alpha \cdot (t_c - t)^p$ with exponents between 0.35 and 0.53 and prefactors α of 400 nm^2 s$^{-2/3}$ to 950 nm^2 s$^{-2/3}$. Only the last part of the curves was used for fitting where the temperature change was negligible.

In a previous study we showed indications for a diffusion limited BDA island decay [38]. Diffusion limited decay was also found in a similar system, namely PTCDA on Ag(100) [54]. In the classical Ostwald theory Eq. 3.7 is integrated using a first order approximation of the Gibbs-Thomson term and assuming that the surrounding mean density is equal to θ_∞ [62, 58, 64]. It follows that the island area decreases like $\alpha \cdot (t_c - t)^{2/3}$ for diffusion limited decay. It is straightforward to find an expression for α in this case:

$$\alpha = \pi (3\frac{\Omega^2 \theta_\infty \gamma D(T)}{l_c k_B T})^{2/3} \tag{3.8}$$

Figure 3.10 shows five decay curves of neighboring BDA islands. The temperature was increased in one step from 348 K to 362 K starting at t = 2500 s and reached the final temperature at about t = 3000 s. We can see that individual decay curves cross each other several times, for example island 3

and 4 at $t = 3400\,\mathrm{s}$. This cannot be understood within the simple model. Local correlations influence the decay behavior of individual islands. This is a feature of diffusion limited decay, where the exact arrangement of islands determines the decay rate through density fields. Nevertheless, the final parts of the decay curves, where the temperature change was negligible, could be fitted with curves of the form $\alpha \cdot (t_c - t)^p$. The fitted exponents p are between 0.35 (island 5) and 0.53 (island 1) and prefactors α are approx. $400\,\mathrm{nm}^2\,\mathrm{s}^{-2/3}$. The exception is island 3 which decays much faster and has a prefactor of $950\,\mathrm{nm}^2\,\mathrm{s}^{-2/3}$. The exponents that we find are smaller than the $2/3$ expected from diffusion limited decay, but are clearly incompatible with the exponent of 1 expected for interface limited decay. Smaller exponents are expected if the linearization of the Gibbs-Thomson term in Eq. 3.7 is not justified, i.e. $\frac{\gamma\Omega}{kTr}$ is large. From the presence of local correlations in the decay process and critical exponents well below 1, we conclude that the decay is indeed, at least partially, limited by diffusion. However, we cannot exclude a mixed case, i.e. also the detachment of molecules is a limiting factor in the decay.

The classical Ostwald theory approach that we used here has two major deficiencies: First, it does not include the local correlations between the decaying islands, which we observe. Secondly it assumes a constant mean density $\overline{\theta}$, implying that the decay is only driven through the size dependence of θ_r. This is a crude approximation since the decay involves large amounts of molecules transported from the islands into the dilute phase changing $\overline{\theta}$.

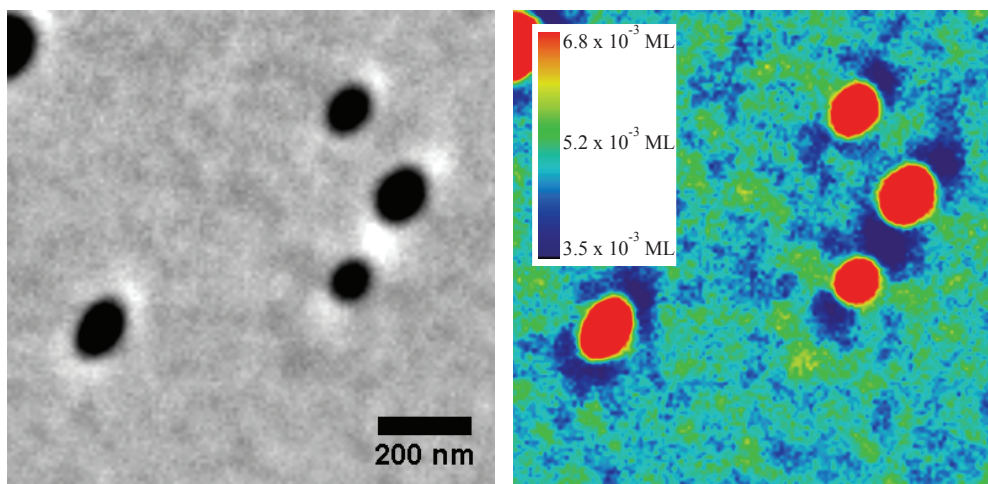Figure 3.11: **Left:** LEEM image of the BDA domains in Fig. 3.10 at $t = 3250\,\mathrm{s}$. **Right:** The same image in false colors representing the molecular density between the islands. The high contrast makes the island appear bigger. The blue areas around the islands going from bottom left to top right are due to lensing effects (see text), obscuring density gradients close to the islands edges.

Since we are able to measure $\bar{\theta}$ and we know the equilibrium density, we can, in principle, fit the curves with Eq. 3.7 directly. However, this will fail for the rather small islands in Fig. 3.10. We cannot resolve $\bar{\theta}$ locally. Figure 3.11 shows a LEEM image of the islands from Fig. 3.10 at $t = 3250\,\mathrm{s}$. In the right hand image of that figure, the color scale was scaled to represent the molecule density. No gradients can be observed between the islands. Unfortunately, work function differences between BDA and Cu lead to lensing effects (blue halos around the islands) [66], which hide the particularly interesting molecular density close to the islands' edges. The density should drop fast from island edges, while further away the change becomes considerably smaller [58]. For most of the decay in Fig. 3.10 the islands are larger than $2500\,\mathrm{nm}^2$. A quick estimate of the vapor pressure of such an island using Eq. 3.5 gives a value that is $\sim 11\%$ above the equilibrium density. This would be the maximum density change from the edge of an island of such size, to sufficiently far away. A density difference of this size would be on the order of the noise level in Fig. 3.11 and is thus not detectable under the conditions here.

3.5.2 Decay of large islands

To avoid the local correlations, we will now analyze the decay of large, well separated islands. Figure 3.12 shows a LEEM image of the relevant islands. The initial island sizes were between $6 \times 10^5\,\mathrm{nm}^2$ and $1.4 \times 10^6\,\mathrm{nm}^2$, with cauliflower like shapes. This is not the equilibrium shape. We observed that the islands become compact on a time scale of several hours. In the experiment the temperature was changed in two steps, first from $375\,\mathrm{K}$ to $386\,\mathrm{K}$ and then from $386\,\mathrm{K}$ to $400\,\mathrm{K}$.

Unlike for the small islands, we will now use Eq. 3.7 directly. We know θ_r from the sample temperature and we can measure $\bar{\theta}$. Despite the cauliflower shape, the islands' curvatures are very small and we can replace θ_r with θ_∞ without introducing a large error. The decay rate should thus simply be given by the difference of $\bar{\theta}$ and θ_∞.

In Fig. 3.13(a) we show both $\bar{\theta}$ and θ_∞. The temperature was first increased at $\mathrm{t} = 600\,\mathrm{s}$, then a second time at $\mathrm{t} = 1740\,\mathrm{s}$. After each step the temperature was kept constant at the new value. θ_∞ has been calculated following exactly the actual variation of the temperature. The difference of the two curves is plotted in Fig. 3.13(b)). This curve was used to fit the decay of four islands, which is shown in the same graph.

We can describe the decay of all four islands by taking the difference between $\bar{\theta}$ and θ_∞ multiplied with a constant value (κ) as the decay rate. The
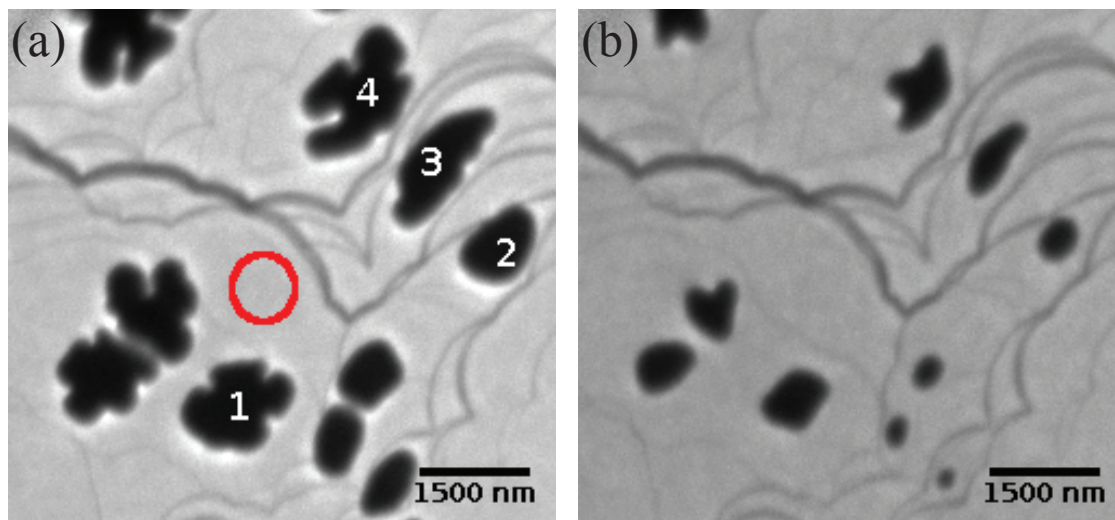
Figure 3.12: LEEM images of large decaying islands. **(a)** At the start of the experiment at $T = 375\,\mathrm{K}$. The circle marks the area used to measure the mean density. **(b)** At the end of the experiment at $T = 400\,\mathrm{K}$. The contrast change of the Cu terraces shows the increased BDA density.
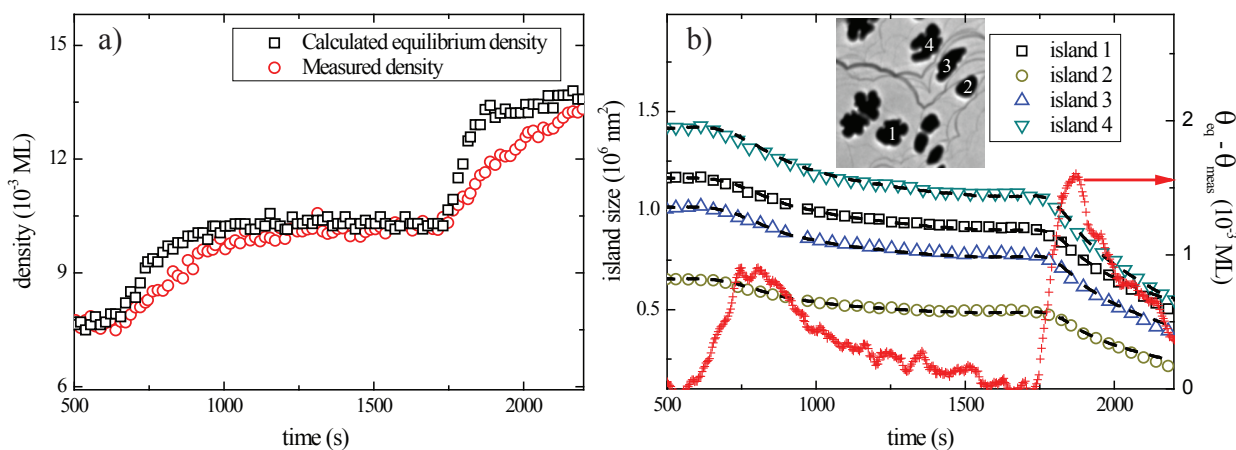
Figure 3.13: **(a)** Measured density surrounding the islands from Fig. 3.12 (red circles) and equilibrium density (black squares) calculated with the help of the phase diagram (Fig. 3.7). The temperature is raised in a first swift step at $600\,\mathrm{s}$ from $375\,\mathrm{K}$ to $386\,\mathrm{K}$ and then in a second swift step at $1740\,\mathrm{s}$ to $400\,\mathrm{K}$. The sharp change at $t = 1800\,\mathrm{s}$ is due to a reduced heating power. **(b)** Measured island size as a function of time together with the fitted curves (dashed lines). The small red pluses show the difference between the two curves in (a). This curve is used as the driving force for the island decay.

value of κ is different from island to island and was used as a fit parameter. The last part could not be fitted, probably because the assumption of a constant screening length starts to fail. The shape and the local geometry are changing too much. The unknown parameters in κ are the temperature dependent diffusion constant $D(T) = D_0 \cdot exp(\frac{-E_D}{kT})$ and the screening length l_c. Unfortunately, the temperature difference is too small to get a meaningful value for the diffusion barrier E_D. We could fit the data with values from $0\,\text{eV}$ to $0.6\,\text{eV}$, however slightly better fits are obtained with a diffusion barrier in the middle of that range. We find that κ depends almost linearly on the initial island size and has values between $1.9 \times 10^4\,\text{nm}^2\,\text{s}^{-1}$ (island 2) and $3.6 \times 10^4\,\text{nm}^2\,\text{s}^{-1}$ (island 4). The reason for this is a size-dependent screening length l_c. It is impossible to give an analytic expression for the screening length. However, ignoring the complex shapes and using the exact expression for a concentric geometry, $l_c = ln(\frac{r+R}{r})$, it is obvious that l_c will decrease for increasing island size, as long as R is a constant. Surprisingly, κ seems to be almost independent of the islands surroundings. For instance, the fits for islands 1 and 3 result in almost the same κ ($\approx 2.6 \times 10^4\,\text{nm}^2\,\text{s}^{-1}$), but their environment is substantially different. While island 3 is blocked by Cu steps on two sides and is located on a small terrace, island 1 is situated on a large terrace and is relatively open to all sides. Apparently, Cu steps are not limiting the diffusion of molecules, since otherwise a smaller κ (i.e. a slower decay) would be expected for the island located on a smaller terrace.

3.6 Discussion on island decay

We analyzed the decay of single BDA domains using two methods. First we studied the decay of small islands at $362\,\text{K}$ using a classical Ostwald ripening approach. Except for the screening length l_c, we have all ingredients to calculate the diffusion constant D from the fitted prefactors ($\alpha = 400\,\text{nm}^2\,\text{s}^{-2/3}$). However, we can estimate l_c using the exact expression for a concentric geometry. Since we cannot observe density gradients between the islands, the equilibrium density has to be reached close to the islands' edges, probably within a few tens of nanometers. This would result in $l_c \approx 0.5..1$ and a diffusion constant in the range of $650\,\text{nm}^2\,\text{s}^{-1}$ to $1300\,\text{nm}^2\,\text{s}^{-1}$ at $362\,\text{K}$.

In order to avoid the local correlations during the decay process, we also analyzed the decay of larger, further separated islands and used the difference between θ_∞ and measured $\overline{\theta}$ surrounding the islands as the driving force for decay. Using this single curve, we could fit the decay of four islands, each with an individual, size-dependent rate constant κ. The decay rate is

independent of the island's location on the underlying Cu-substrate. This means that BDA diffusion is not limited by Cu steps. It is important to note that this observation is independent of the model used, i.e. whether the decay is limited by diffusion or by detachment of molecules. It is solely based on the observation of comparable decay rates for islands having completely different relations to step edges. Another observation showing the transparency of steps for BDA diffusion is that terraces which are free of BDA islands follow the same contrast change as the other terraces upon changing the substrate temperature. If there was a significant barrier for molecules to cross, there should be a delay during which the densities on the terraces equilibrate.

As for the small islands in Fig. 3.11, we cannot resolve BDA density gradients, which implies that the density falls off rather fast from BDA island edges. Assuming that within $100\,\mathrm{nm}$ from the islands' edge the mean density is reached, we find $l_c = ln(\frac{100\,\mathrm{nm}+r}{r}) = 0.14 \, .. \, 0.22$, depending on island size r. With these numbers we can give a further estimate for the diffusion constant: $800 \pm 100\,\mathrm{nm^2\,s^{-1}}$ in the temperature range between $375\,\mathrm{K}$ and $400\,\mathrm{K}$. This value is an estimate that is relying on the assumption of diffusion limited decay. As we already mentioned, we cannot exclude a mixed case, in which the detachment rate of molecules also limits the decay.

Another way to measure diffusion constants of organic molecules on a surface is by STM, either at low temperature when the diffusion is slow enough to observe single hopping of molecules [67] or by placing the tip over the surface and measuring the fluctuations of the tunneling current [68]. In the latter reference, again for PTCDA on Ag(100), a diffusion constant of $(4 \pm 1.1) \times 10^3\,\mathrm{nm^2\,s^{-1}}$ was found at room temperature.

The tracer diffusion constant is measured by STM. This constant refers to the rate at which individual molecules hop between lattice sites, which at low coverage is given through an attempt frequency and a Boltzmann factor containing the diffusion barrier [69, 70]. Here we determined the chemical diffusion constant, which describes the rate at which density gradients equilibrate following Fick's law. To be precise, we used the density gradients from the islands' edges to the area farther away where the mean density is reached. Individual molecules still hop in a random way from site to site, going with almost equal chance towards or away from the island edge, but there is a net mass flow away from the islands.

The high coverage in the dilute phase relative to the crystalline phase will lead to strong molecular interaction, changing the diffusion constant in different directions [71]: Blocking of lattice sites, attractive interaction through hydrogen bonds, and repulsive forces from the negatively charged carboxylate groups will make both the tracer and chemical diffusion constant

a complex function of coverage and temperature. One could even imagine a situation in which, due to a larger equilibrium density, the diffusion constant at a higher temperature is smaller than at a lower temperature.

3.7 Conclusions

We studied the temperature dependent equilibrium density of the dilute phase formed by BDA molecules surrounding ordered hydrogen bonded BDA networks with LEEM by measuring the local electron reflectivity. The amount of molecules in the dilute phase is substantial, with densities of up to 40% of the crystalline phase. We analyzed the resulting 2D phase diagram with a lattice gas model and found a cohesive energy of $E_C = 0.35 \pm 0.03\,\mathrm{eV}$. This value also contains a coverage dependent interaction term, which we cannot separate from the cohesive energy using our data. However, we can estimate the interaction term to be small, if compared with E_C. We also see large entropy effects, originating from the large size and structure of the BDA molecules. These entropy effects lead to a large density in the dilute phase relative to the crystalline phase. From the cohesive energy it follows that an individual hydrogen bond has a strength of approximately $0.09\,\mathrm{eV}$, a value which is typical for this type of hydrogen bond.

We also studied the decay behavior of individual BDA domains, and we found diffusion limited decay. By applying a classic Ostwald ripening model to a set of smaller domains, we can estimate the diffusion constant at $362\,\mathrm{K}$ to be between $650\,\mathrm{nm^2\,s^{-1}}$ and $1300\,\mathrm{nm^2\,s^{-1}}$. However, local correlations, characteristic for (partially) diffusion limited decay, have a large influence on the decay behavior of individual islands. To avoid these effects, we also studied the decay of larger, more separated domains. We modeled the decay using the difference between measured density and equilibrium density as the driving force. In the temperature range of 375 - 400 K, we estimate the diffusion constant to be $800 \pm 100\,\mathrm{nm^2\,s^{-1}}$. The decay is independent of the underlying Cu substrate's topography: domains located on a small Cu terrace decay the same way as domains on a larger terrace. This means that Cu steps do not act as high barriers for BDA diffusion.

4

Size fluctuations of near critical nuclei and Gibbs free energy for nucleation of BDA on Cu(001)

We present a LEEM study of nucleation and growth of BDA on Cu(001) at low supersaturation. At sufficiently high coverage a dilute BDA phase coexists with c(8×8) crystallites. The real time microscopic information allows a direct visualization of near-critical nuclei, determination of the supersaturation and the line tension of the crystallites, and thus, to derive the Gibbs free energy for nucleation. The resulting critical nucleus size nicely agrees with the measured value. Nuclei up to 4-6 times larger still decay with finite probability, urging reconsideration of the classic perception of a critical nucleus.

4.1 Introduction

Different models exist that describe the nucleation process of solid structures from a dilute mother phase. All of them have the existence of a critical nucleus size in common. This critical size gives the smallest stable structure during nucleation [29, 51, 52, 48, 72]. Smaller nuclei tend to decay; larger nuclei tend to grow. The reason for this is a competition between positive interface energy terms, favoring decay, and negative bulk terms, favoring growth in the case of supersaturation. For epitaxial growth of metals or semiconductors at room temperature, the size of the critical nucleus is typically a handful of atoms or molecules, while at higher temperatures it can contain several hundred entities [73]. The small size at low temperatures and the fast fluctuations and high mobility at high temperatures make it challenging to observe critical nuclei experimentally. Examples of the direct observation are, therefore, rare. Subcritical nuclei were observed during the nucleation of strained Ge islands on a flat Si surface [74, 75]. Jesson et. al. observed decay of nuclei showing an unexpectedly large size (270 atoms) with STM. Another example is the nucleation of crystallites from a glassy phase, using fluctuation transmission electron microscopy (TEM) and laser pump-probe techniques [76]. On much larger length scales, it is possible to observe the critical nucleus during the growth of colloidal crystals using laser scanning confocal microscopy [77].

The models that describe nucleation are all valid under different conditions [29, 28, 48]. For nucleation close to thermal equilibrium, i.e., low supersaturation and temperatures well below the critical temperature, a classical thermodynamic approach is appropriate. The Gibbs free energy of a randomly formed 2D cluster can easily be determined. Molecules at the islands perimeter add a positive energy term through the edge line tension, and molecules in the bulk add a negative term due to free energy gained from lateral bonding. This leads to an energy maximum for a size where both contributions are equal which defines the critical nucleus size. For a circular flat cluster of size A, the Gibbs free energy is given by:

$$\Delta G = -\frac{A}{\Omega}\Delta\mu + 2\sqrt{\pi A}\chi \tag{4.1}$$

where χ is the cluster's edge line tension, Ω the area occupied by one molecule in the cluster, and $\Delta\mu$ the difference in chemical potential of a molecule in the dilute and in the condensed phase. In the remainder, we will refer to this quantity as chemical potential difference. The maximum, i.e., the Gibbs free energy for nucleation, is reached for a size of $A^* = \pi \left(\frac{\Omega\chi}{\Delta\mu}\right)^2$.

Clusters which are smaller than this size have the tendency to decay; clusters which are larger have the tendency to grow. However, even clusters larger than the critical nucleus can still decay, due to the statistical nature of the process. In equilibrium, the density of subcritical clusters of size A at a given supersaturation is given by:

$$n(A) = n_s exp[-\Delta G(A)/kT] \qquad (4.2)$$

where n_s is the density of nucleation sites. However, during growth, the system is by definition not in equilibrium, and these numbers can differ by one or two orders of magnitude [29].

Here we report on the observation of critical nuclei during the crystallization of 4,4'-biphenyldicarboxylic acid (BDA) molecules into two-dimensional (2D) crystals on Cu(001) using LEEM. BDA forms well-ordered nanostructures on Cu(001) exhibiting a square c(8×8) superstructure [38, 12]. Neighboring molecules are rotated by 90°and interact laterally through hydrogen bonds. These bonds form between the carboxylate group of one molecule and the phenyl rings of the next molecule (see inset in Fig. 4.1). The strength of this bond is $E_{NN} = 0.18$ eV [78]. Surrounding the BDA islands is a molecular dilute phase. Close to room temperature, the equilibrium density in the dilute phase is around a few percent of that in the c(8×8) phase [78]. We will express the density θ in the remainder of this letter in coverage of the underlying Cu lattice. Each molecule occupies 16 Cu-lattice sites or an area of $\Omega = 1.043$ nm^2 and the fully completed c(8×8) structure corresponds then to a coverage of 0.0625 ML.

We used a low BDA deposition rate of only a fraction of a ML per hour. BDA domains grew therefore at low supersaturation, i.e., close to thermal equilibrium. Under these conditions, classical thermodynamic nucleation theory should be applicable [29].

4.2 Experimental

Experiments were performed in an Elmitec LEEM III with a base pressure in the low 4×10^{-10} mbar range. A Cu(001) single crystal was annealed outside UHV for 48h at 1173 K under a flow of a Ar/H$_2$ gas, to deplete bulk sulfur and carbon contamination. The surface was further prepared by prolonged cycles of sputtering with hydrogen and argon ions and subsequent annealing at 873 K. Images were recorded in bright field mode with an electron energy of 2 eV with a frame rate of 0.5 Hz. These settings did not lead to any

observable electron damage to the molecules. All images were corrected for a background originating from the MCP detector plates.

We measured the density in the dilute phase by analyzing locally the change of image intensity on the Cu terraces. With this method it is possible to measure density changes as small as 10^{-3} ML for atomic species [35, 34, 33]. Intensity changes are normalized to the intensity of the clean surface at the start of the experiment. For BDA on Cu(001), we found in a previous study that, one percent change of intensity corresponds to a density change of 5.2×10^{-4} ML [78]. The temperature of the Knudsen cell type BDA evaporator was kept constant at 446 K during the experiments. This setting gave a BDA deposition rate of $F = 1.06 \times 10^{-6}$ ML/s.

4.3 Results and Discussion
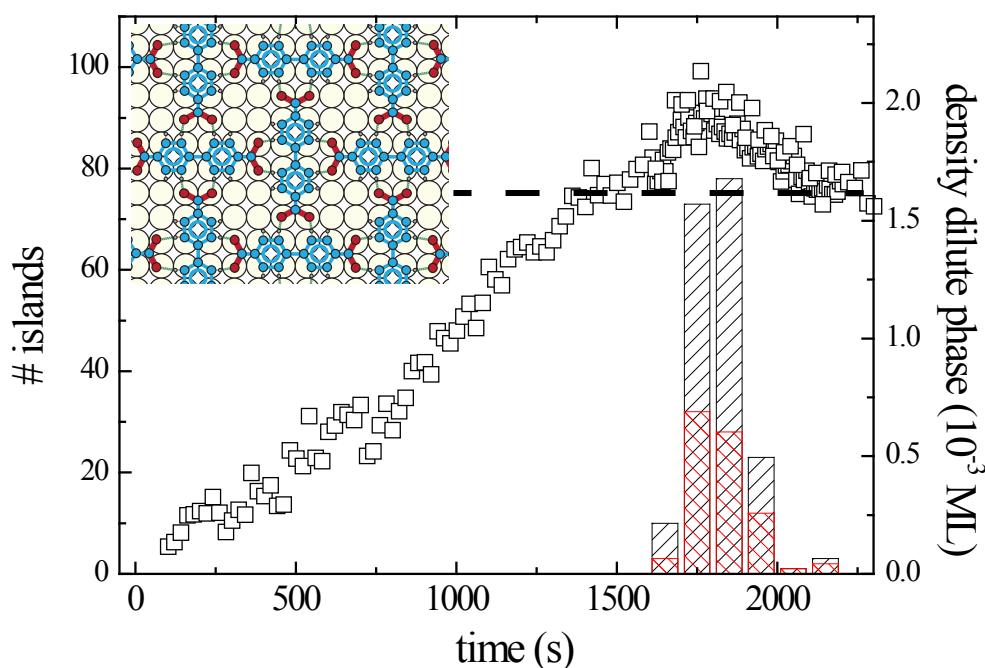
Figure 4.1: Number of nucleating and decaying islands in an area of 12.5 µm^2 (bars, left axis) and density in the dilute phase (squares, right axis). The substrate temperature is 332 K, the shutter is opened at 0 s. From the linear increase of the gas density before nucleation we find a deposition rate of $F = 1.06 \times 10^{-6}$ ML/s. Hatched bars show all nucleation events, cross hatched bars nuclei that decayed. The dashed line marks the equilibrium BDA density level. The inset shows the arrangement of molecules in the c(8×8) structure. Blue (light gray) circles stand for carbon, red (dark gray) for oxygen, small gray circles for hydrogen atoms.

We first describe a typical BDA growth experiment at 332 K. The experiment starts with a clean surface. Right after the shutter of the BDA

evaporator is opened (defined as $t = 0\,s$), the BDA coverage in the dilute phase increases linearly (see Fig. 4.1). Molecules in the dilute phase have the lowest chemical potential up to the equilibrium density $\theta_{eq}(T)$. Once θ becomes (significantly) larger than θ_{eq}, the dilute phase is supersaturated and nucleation of c(8×8) domains becomes possible (t $\approx$ 1600 s - 2200 s in Fig. 4.1). However, due to the aforementioned nucleation barrier, the nucleation rate depends strongly on supersaturation. In Fig. 4.1, we show the measured density together with the number of islands nucleating in time windows of 100 s. The nucleation rate depends strongly on supersaturation and is highest during the maximum θ (t $\approx$ 1700 s - 1800 s). Finally, the island density is large enough to accommodate the arriving molecules and to reduce the supersaturation. In the end, nucleation stops and existing islands merely grow in size. The density θ at this point is almost equal to the equilibrium value θ_{eq}.

We observe the decay of small nuclei throughout the distinct nucleation period. The number of nuclei that decayed are shown as red (cross hatched) bars in Fig. 4.1. Nuclei which contain up to 4000 molecules can decay. The time scales of these fluctuations are several seconds or even minutes. Islands which are larger, are stable for a substantially longer time span. Another way for these larger islands to decay is through Ostwald ripening, which occurs on a time scale of hours or even days for the sample temperatures used here.

As can be seen in Fig. 4.1, about 40% of the observed nucleated clusters are unstable and eventually decay. Example LEEM images of these subcritical nuclei are shown in Fig. 4.2 for two experiments at 305 K and 332 K. It is difficult to capture the process in a few images. The average lifetime of the subcritical nuclei is only one or two frames, not many of them are imaged simultaneously. We could not distinguish any specific pattern formed by the position where the unstable nuclei nucleated. Particularly, the distance to a substrate step did not seem to matter and islands did not nucleate twice at the same position. The latter would be a strong indication for defect induced nucleation. However, we do note a tendency for extremely long range order formed by the position where a nucleation event occurred, irrespective of whether the nucleus is stable or not. For example, in the second panel of Fig. 4.2(b), the central region is almost without islands, while above this region several islands nucleated with a large density. Probably because of diffusion and/or attachment limitations [38], there is a higher nucleation probability on or close to lines connecting existing islands, leading to preferential nucleation along these line and, thus, to an average island-island distance that is smaller than what would be expected for purely random nucleation. Tentatively, we explain this observation with local density gra-

dients in the dilute phase, which are generated in a complex way by growing and decaying islands. We already reported that island decay is limited by diffusion, which means that local density gradients can exist [38, 78]. The molecular density is then highest on the line connecting circular islands. Subtle differences in the local supersaturation will then dramatically influence the local nucleation rate.

We analyzed the maximum size each nucleus reached before decaying and grouped them in bins with size windows of $500\,\mathrm{nm}^2$. Figure 4.3 shows these distributions for experiments at substrate temperatures of T $=$ $297\,\mathrm{K}$ and T=$332\,\mathrm{K}$. Obviously, the decay of larger nuclei is observed less often. For nuclei smaller than $1000\,\mathrm{nm}^2$, we are limited by the instrument resolution: With a field of view of $4000\,\mathrm{nm}$ and an image size of 512x512 pixels, a $1000\,\mathrm{nm}^2$ nucleus covers about 16 pixels.

Any determination of the size of decaying islands is therefore affected by a large error bar. Especially for smaller scale fluctuations ($< 1000\,\mathrm{nm}^2$), we may not capture all events.

From the final nucleation density and the maximum size distributions (Fig. 4.3), we can calculate the probability for a nucleus of a given size to decay. These probabilities are shown in Fig. 4.4 for four experiments between $297\,\mathrm{K}$ and $332\,\mathrm{K}$. Nuclei that reached a size of $1500\,\mathrm{nm}^2$ decay with a probability between $17 \pm 3\%$ ($332\,\mathrm{K}$) and $8\% \pm 1\%$ ($297\,\mathrm{K}$). As expected, the probability for a nucleus to decay is dropping for larger sizes. Except for the smallest sizes, this decay probability can be very well fitted with exponentials of the form $p_{decay} = exp(-A/A^*)$. This is reasonable given that the size distribution of subcritical nuclei is also given by an exponential (Eq. 4.2). From the fits, we find that nuclei with a size between $400\,\mathrm{nm}^2$ ($297\,\mathrm{K}$) and $600\,\mathrm{nm}^2$ ($332\,\mathrm{K}$) have an equal chance to decay or grow. This value should depend on $\Delta\mu$. We did not see such a dependence for two reasons: first, most of the islands nucleate during the largest $\Delta\mu$ anyway (see Fig. 4.1), and second, the statistics are too poor.

It is intriguing that we can observe critical fluctuations in such detail as we show here. Why is this possible? Compared to other systems, the fraction of molecules in the dilute phase of BDA on Cu(001) is already substantial at room temperature. This means that the nucleation rate will be higher at relatively small supersaturation, and the critical nucleus size accordingly very large, cf., Eq. 4.1. The 2D cohesive energy of the BDA molecules in the hydrogen bonded c(8×8) structure is rather small, which leads to high densities in the dilute phase at room temperature [78]. The combination of an appreciable nucleation rate at low supersaturation and slow molecular
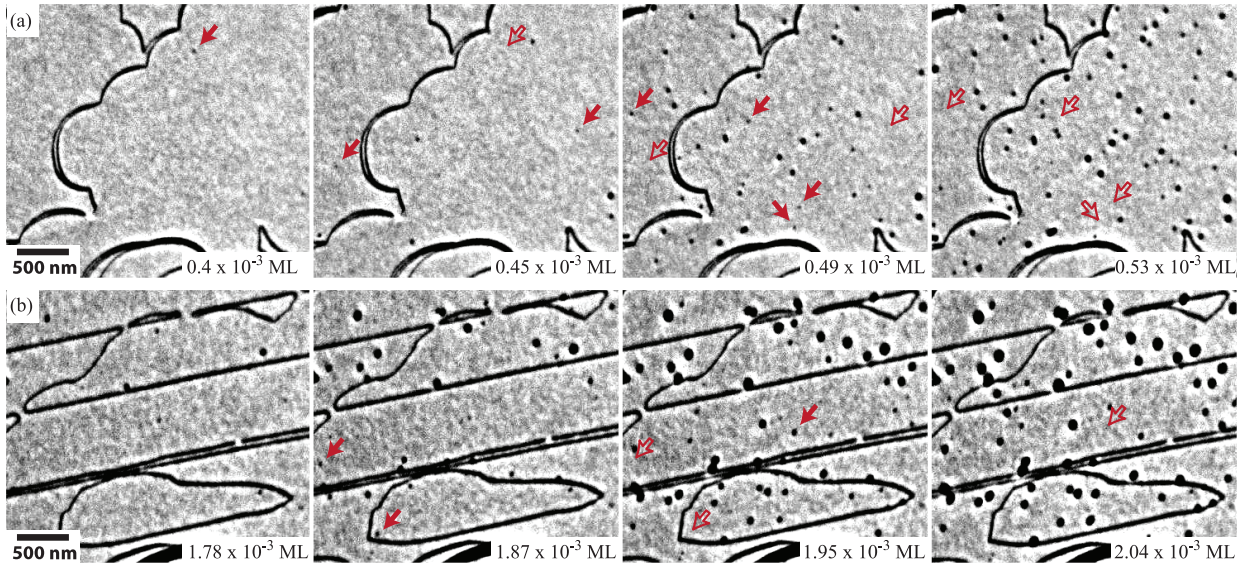
Figure 4.2: LEEM images taken during the nucleation phase (total BDA coverage is indicated in the images) with $T_S = 305\,$K **(a)** and $T_S = 332\,$K **(b)**. Islands marked with a red arrow disappeared in the subsequent image, the corresponding position is marked with hollow arrows. Time between images is $40\,$s (a) and $80\,$s (b), respectively.
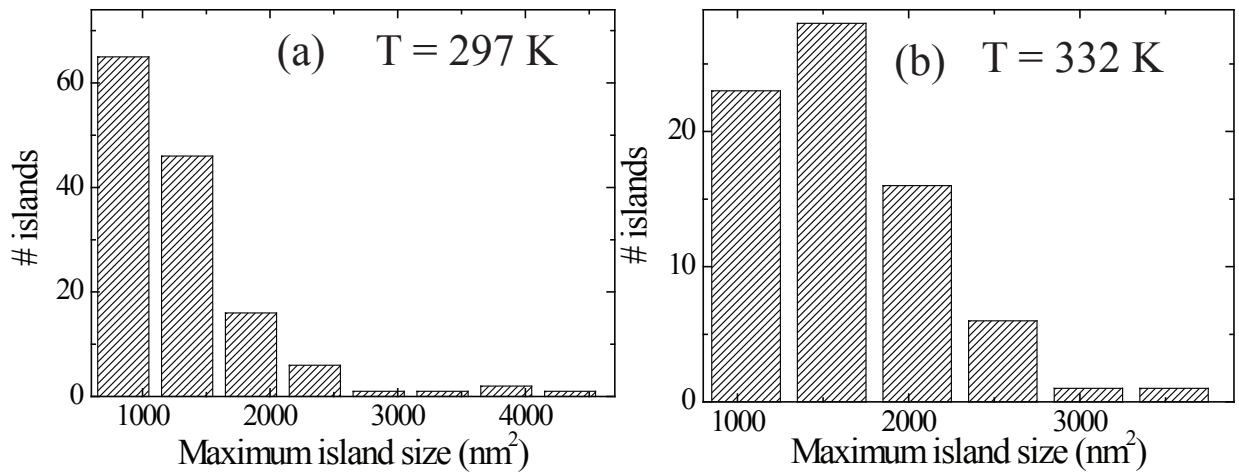
Figure 4.3: Maximum island size reached by islands that decayed for two experiments at T $= 297\,$K **(a)** and T $= 332\,$K **(b)**. The total number of stable and unstable nuclei was 381 (T $= 297\,$K) and 189 (T $= 332\,$K) in an area of $12.5\,\mu\text{m}^2$.

Figure 4.4: Decay probability for clusters reaching a certain size for four experiments at different temperatures. The dashed lines are exponential fits to the data.

diffusion results in a large critical nucleus which has a sufficiently long lifetime to be observed.

Finally, we emphasize that we present a rather complete data set on the nucleation of BDA on Cu(001). We have the equilibrium density of the BDA molecules in the dilute phase and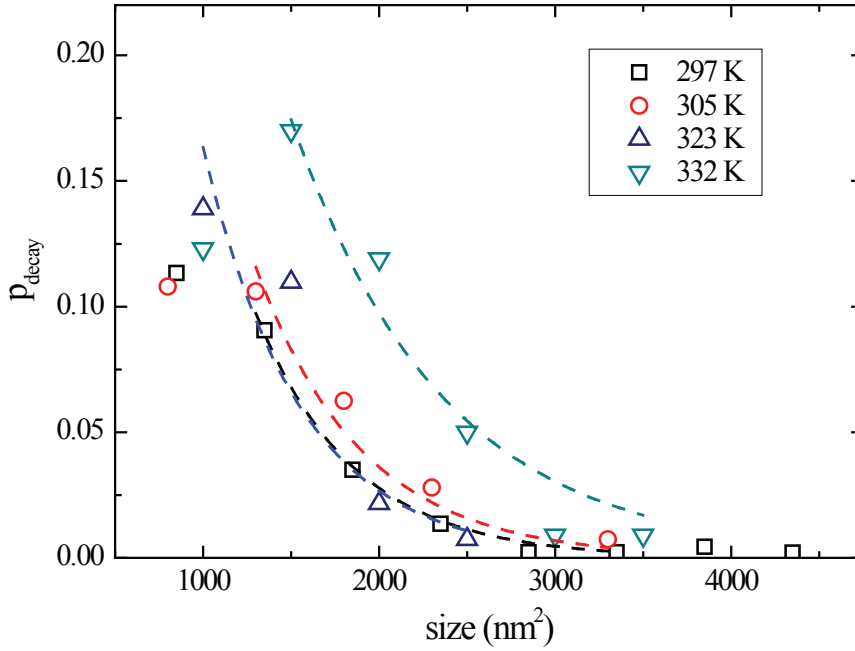 from the phase coexistence line of the dilute and the crystalline phase we have obtained the 2D cohesive energy of $0.35 \pm 0.03\,\mathrm{eV}$ [78]. From that value we can directly derive the line tension $\chi = 86\,\mathrm{meV/nm}$. From Fig. 4.1, we learn that the molecular density in the dilute phase reaches $\theta_{max} = 2 \times 10^{-3}\,\mathrm{ML}$, while the equilibrium value is about $\theta_{eq} = 1.6 \times 10^{-3}\,\mathrm{ML}$. Treating the dilute phase as an ideal 2D monatomic gas, the maximum chemical potential difference during nucleation is then: $\Delta\mu = kT\,ln(\frac{\theta_{max}}{\theta_{eq}}) \approx 6\,\mathrm{meV}$. With the molecular area Ω of $1.043\,\mathrm{nm}^2$, we have all the information we need to extract the Gibbs free energy for nucleation, which so far was not reported for any heteroepitaxial system. Tromp and Hannon reported a value of 1.5 eV for high temperature homoepitaxial nucleation of Si on Si(001) [72]. Rewriting Eq. 4.1 for this purpose we obtain $\Delta G^* = \pi\frac{\Omega\chi^2}{\Delta\mu}$. At 332 K, the Gibbs free energy barrier for nucleation of BDA on Cu(001) amounts to $4.0\,\mathrm{eV}$ with an error flag of about 25%, with the uncertainty dominated by those in line tension χ and $\Delta\mu$.

With the above numbers for the line tension and the chemical potential difference, we obtain a size of the critical nucleus at 332 K of $A^* \approx 680\,\mathrm{nm}^2$. We estimate this number to be correct within a factor of 2 due to uncertain-

ties in $\Delta\mu$ and χ, equally contributing to the possible error. This number compares favorably with the experimental value of $600\,\text{nm}^2$ at $332\,\text{K}$. This value is subject to experimental uncertainties, related to field distortions which may generate bright halos surrounding the islands. We estimated this effect by applying realistic values in Eq. 8 of reference [79] to be less than 10% for islands of $700\,\text{nm}^2$. We therefore conclude that our data are convincingly consistent, and the critical nucleus has a large size of about 650 molecules at $332\,\text{K}$. We found substantial fluctuations in the size of the unstable nuclei. Up to $4000\,\text{nm}^2$, islands still have a finite probability to decay for a critical nucleus size of $680\,\text{nm}^2$. These fluctuations are a lot larger than expected. In classical nucleation, it is assumed that clusters with Gibbs free energy of $\Delta G = \Delta G^* \pm kT$ contribute to the nucleation. In this context the largest cluster that still decays will have a Gibbs free energy of the critical nucleus minus kT. The size fluctuations can be estimated through the so called Zeldovich factor [48], which would, however, underestimate the magnitude of the size fluctuations by one order of magnitude. We suggest that local fluctuations in supersaturation are responsible for this remarkable critical behavior. This is consistent with the diffusion limitations during decay we reported earlier [38].

4.4 Conclusions

In conclusion, we have measured size fluctuations of near critical clusters during the nucleation of BDA on Cu(001) for temperatures between $297\,\text{K}$ and $332\,\text{K}$. From the LEEM image intensity data, we extract the local chemical potential difference, which is of the order of (a few) meV. We sample the probability for decay and further growth of individual islands. By equalizing the integrated values of both probabilities, we arrive at critical island sizes of 400 - $600\,\text{nm}^2$. We find that islands with a size of $1500\,\text{nm}^2$ decay with a probability between 8% and 17%, depending on the substrate temperature. The decay is exclusively observed for subcritical nuclei and in those situations where the surrounding dilute phase is still supersaturated. It is remarkable that islands with a size of 6 and 4 times the critical value have still a 1-2% and $> 10\%$ probability, respectively, of eventual decay. We believe that this commonly neglected behavior is generic, especially in the case of low supersaturation. Finally, the complete set of microscopic data allowed us to determine experimentally the Gibbs free energy for nucleation. For BDA growth on Cu(001) at $332\,\text{K}$ and a chemical potential difference of $6\,\text{meV}$,

we obtain a value of $\Delta G = 4.0\,\text{eV}$ with an uncertainty of about 25%. This method using LEEM can be applied in general.

5

Growth anomalies in supramolecular networks: BDA on Cu(001)

We have used low energy electron microscopy (LEEM) to demonstrate how the interaction of 4,4'-biphenyldicarboxylic acid (BDA) molecules with (steps on) the Cu(001) surface determines the structure of supramolecular BDA networks on a mesoscopic length scale. Our in-situ, real time observations reveal that steps are permeable to individual molecules, but that the change in crystal registry between different layers of the Cu substrate causes them to completely block the further growth of condensed BDA domains. The initial number of nuclei is much smaller than the number of Cu terraces, resulting in the occurrence of nucleation "waves", once the first domains cover an entire respective terrace. The growth of the domains is governed by growth instabilities and include a novel Mullins-Sekerka type growth instability, that is characterized by high growth rates *along*, instead of *perpendicular* to the Cu steps. This growth instability is responsible for the majority of residual defects in the BDA networks.

5.1 Introduction

The self-assembly of organic molecules into extended supramolecular networks is of high current interest [5, 4, 80, 21]. Most of these studies are motivated by the potential for the networks to act as flexible templates for the fabrication of novel nanoscale structures [10, 11, 12, 20, 81]. Detailed STM studies of the molecular networks and their building blocks have been performed [10, 11, 13, 14, 15, 16, 17, 18, 19]. So far, only a few studies have concentrated on thermodynamic and kinetic aspects of the growth of supramolecular domains on a mesoscopic length scale [27, 54], despite the importance of both to make these networks applicable. An in-depth study of either involves relatively high temperatures. Consequently, the topography of the molecular films will no longer only be determined by the intermolecular bonds that stabilize the domains, but instead be dominated by the interaction of molecules and/or molecular domains with substrate steps.

The self-assembly process itself can be described within the well-established formalism for homo- and heteroepitaxial growth [29, 48, 52]: At low adatom (-molecule) densities, the surface is only covered with a dilute phase. When more atoms (molecules) are deposited on the surface, the dilute phase becomes more and more dense, until the system enters the coexistence region with a solid (crystalline) phase. The dilute phase becomes supersaturated at this point, which induces the nucleation of crystalline domains. The larger the supersaturation, the higher the nucleation rate, i.e., the probability for a nucleus to form. The nuclei grow at the expense of the supersaturation, which inhibits further nucleation. Nucleation of domains occurs thus in a well-defined time window, during which the supersaturation is largest. In the further course, the domains grow, until they eventually cover the entire surface and coalescence. For sake of completeness we note that above "solid" may be replaced with "liquid". However, the latter is not applicable here.

The case becomes more complicated, if the influence of steps is taken into account, which is well documented from studies on single crystalline metal surfaces [82, 83, 84, 85, 86, 87, 88, 89, 90]. At the elevated temperatures of interest here, all deposited atoms can reach existing substrate steps, where they aggregate. This leads to growth by step propagation or step-flow growth; in the ideal case the steps continuously advance and a smooth layer-by-layer growth results. This is not only the case for homoepitaxial growth, but sometimes also for heteroepitaxial growth. Fluctuations during growth may lead to growth instabilities. As pointed out by Mullins and Sekerka [91, 92], protrusions at steps lead to a decreased distance between isoconcentration lines of adatoms and enhanced growth rate, while inclinations tend to locally

reduce growth rates. This generic tendency for instability is counteracted by minimization of step length via edge diffusion. Mullins and Sekerka (MS) were able to define conditions for the occurrence of MS growth instabilities. For 2D growth, a MS instability occurs through the enhanced growth of protrusions perpendicular to the pre-existing steps. This should not be confused with the related Bales-Zangwill instability [93], which is counteracted by a downward flux from the upper terrace due to an accumulation of isoconcentration lines above inclinations. Examples of the latter have been published for the homoepitaxial growth of vicinal Cu(001) surfaces [94, 95].

In this manuscript, we describe how the same concepts, that were developed to describe the initial growth of metal films on metal surfaces, can be applied to understand the growth of molecular films at elevated temperature. LEEM and µLEED were used to study the growth of 4,4'-biphenyldicarboxylic acid (BDA) on Cu(001). BDA is a benzoic acid that deprotonates on Cu(001) below room temperature [10, 11, 12, 20, 81]. It consists of two phenyl rings with one functional carboxyl group at each end. The slightly twisted molecule adsorbs flat on Cu(001) and forms islands with a c(8×8) superstructure [12, 38], facilitated by a hydrogen bridge between the phenyl groups of one molecule and the carboxylate group of another. As a consequence, a square building block is formed in which adjacent molecules are oriented perpendicularly (cf. Fig. 5.5). LEEM images reveal a strong influence of the substrate morphology on the growth of the BDA domains: Monatomic steps block the expansion of domains, while steps are permeable for individual molecules. Also, the images reveal clear evidence for a MS-type growth instability. We observe the classic case, in which an isolated island, that is initially compact, ramifies during further growth, as well as the classic MS-instability at a step. In this case, the growth front moves fastest in a direction perpendicular to the substrate steps. In addition, we demonstrate a case that has not been previously reported, in which the growth rate is highest parallel, instead of perpendicular to the steps. As we will show below, the latter instability is mainly responsible for deficiencies in the final BDA-film.

5.2 Experimental

The experiments have been performed in an Elmitec LEEM III microscope [32] with a base pressure of about 1×10^{-10} mbar. A Cu(001) single crystal with a miscut angle less than 0.1° was used [37]. Prior to mounting, it was annealed at about 1170 K in an Ar-H_2 mixture for a prolonged period

to deplete the bulk of the crystal from sulfur contamination. The sample surface was further cleaned in UHV by cycles of sputtering with hydrogen [39], argon, and annealing at 900 K. The BDA (purity > 0.97, TCI Europe, CAS: 787-70-2) was deposited from a Knudsen cell. The deposition rate was kept constant at 3.2×10^{-5} monolayers (ML) per second. One monolayer is defined as one BDA molecule per Cu(001) unit cell. The c(8×8) structure completely covers the surface at 0.0625 ML. All LEEM images were recorded with 2 eV electrons using a 25 µm illumination aperture and were background corrected by applying a flat field correction. Densities of BDA admolecules were estimated from the diffuse reflectivity [33, 34, 35]. No indications for electron beam induced damage of the molecular networks were observed at any time (cf. Chapter 2). The substrate temperature was kept fixed at 410 K, well below the temperature where thermal decomposition occurs (>450 K), but also high enough to ensure a high mobility that results in a very low density of nuclei. In previous work, we have already established that no significant desorption of BDA molecules into vacuum takes place up to the decomposition temperature and that the condensate is crystalline with a c(8×8) structure at all considered temperatures [78, 96].

5.3 Results and Discussion

In a first experiment, we recorded a LEEM movie during deposition of BDA on Cu(001) at 410 K. A few snapshots with a Field of View (FoV) of 15 µm are shown in Fig. 5.1 (bottom). The light gray curved lines represent single steps and step bunches. The shutter of the Knudsen cell was opened at t = 0 s and closed at 1660 s. Figure 5.2(a) shows the density of the 2D dilute BDA phase as a function of time and measured in three different areas on the surface (marked with dashed squares in Fig. 5.2(b)). The "noisy" appearance of the coverage versus time plots is by no means accidental. The first maximum coincides with the first nucleation stage in which three nuclei start to grow within the FoV, which are recolored in red in the LEEM image shown in Fig. 5.2(b). Immediately after growth of the first generation of nuclei, the admolecule density is reduced from the supersaturation that is needed to initiate condensation close to equilibrium [96]. Several observations are immediately evident. First, the number of initial nuclei is more than two orders of magnitude lower than the number of Cu(001) terraces. Second, the consequences of nucleation and growth of new domains affects the admolecule density across at least ten Cu steps over a distance of several microns. Third, secondary nucleation is observed and further nucleation oc-
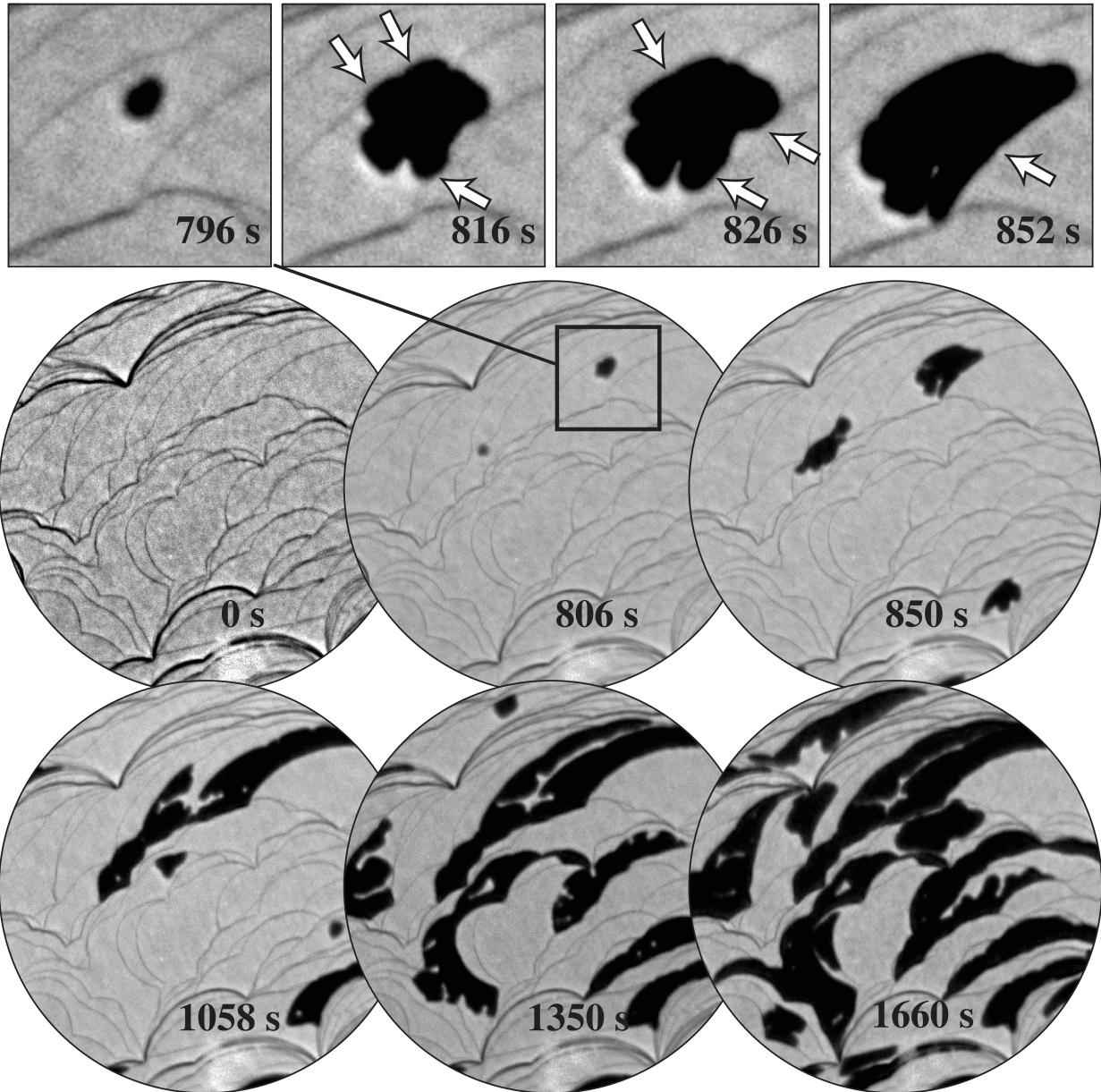
54

Figure 5.1: **Bottom:** Snapshots from a LEEM movie at the indicated times with a FoV of $15\,\mu m$ and a substrate temperature of $410\,K$. The time is relative to the start of the deposition. Dark areas correspond to the crystalline c(8×8) structure. The curved lines in the background represent single and multiple steps on the Cu(001) substrate and are most clearly visible on the clean substrate (first image). This image was superimposed on the subsequent LEEM images to improve the step contrast. **Top:** The growth of a single BDA domain. First, a compact shape develops, which evolves into a ramified one with protrusions and recesses due to a MS growth instability. Upon further growth, the protrusions hit the Cu step first (arrows). Recesses remain, which are subsequently filled until the domain edges precisely follow the steps bordering the host terrace.
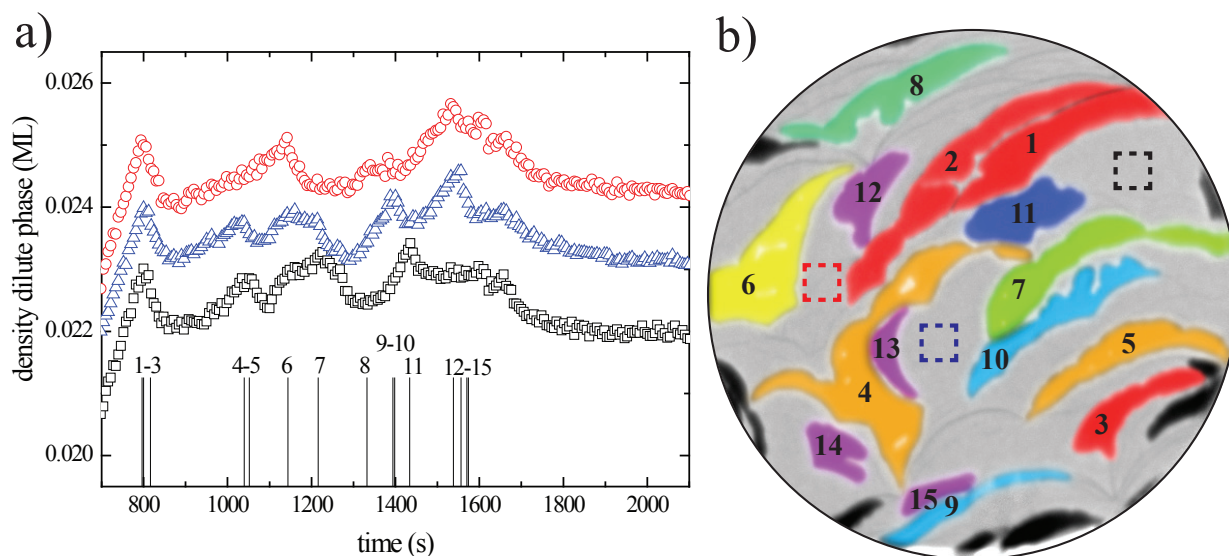
Figure 5.2: **(a)** Density in the dilute phase as a function of time for the experiment in Fig. 5.1. The BDA deposition was started at $t = 0\,s$ and stopped at $t = 1660\,s$. Nucleation started at $794\,s$ at a dilute phase density of $0.024\,ML$. The three different curves are measured in the areas marked with dashed squares of the same color in (b) and offset against each other for clarity. The scale on the left corresponds to the center (blue) data points. Bars indicate the individual nucleation events. **(b)** Recolored LEEM image from the end of the growth in Fig. 5.1. Domains of the same color nucleated approximately at the same time during the experiment.

curs in "waves". Fourth, each combination of a maximum and decay in the admolecule density can be traced down to a single nucleation event. Finally, not all nucleation events are visible in the admolecule density measured in the different areas, as nucleation and growth proceeds. For example, nucleation of island 10 and 11 (cf. Fig. 5.2) shows only up in the density measured in the corresponding area close by, not in others. These observations lead to a number of important conclusions. First, monatomic steps are permeable for individual BDA molecules, i.e., the Ehrlich-Schwoebel barrier for crossing steps must be low. Second, existing BDA domains act as a high barrier for diffusion of individual BDA molecules, thereby preventing the remote nucleation events from becoming visible in the admolecule density of the different areas (dashed squares Fig. 5.2(b)). Third, the steps do not act as preferred nucleation sites, since that would lead to roughly one nucleus per terrace and a well-defined nucleation window. Thus, nucleation proceeds through homonucleation rather than heteronucleation.

The latter is reiterated by the fact that nuclei eventually emerge on all terraces and any preference for nucleation at steps is absent. We analyzed the position of 14 nuclei and plotted the sum of nuclei within a certain distance from the next ascending step in Fig. 5.3. The resulting curve shows a slightly
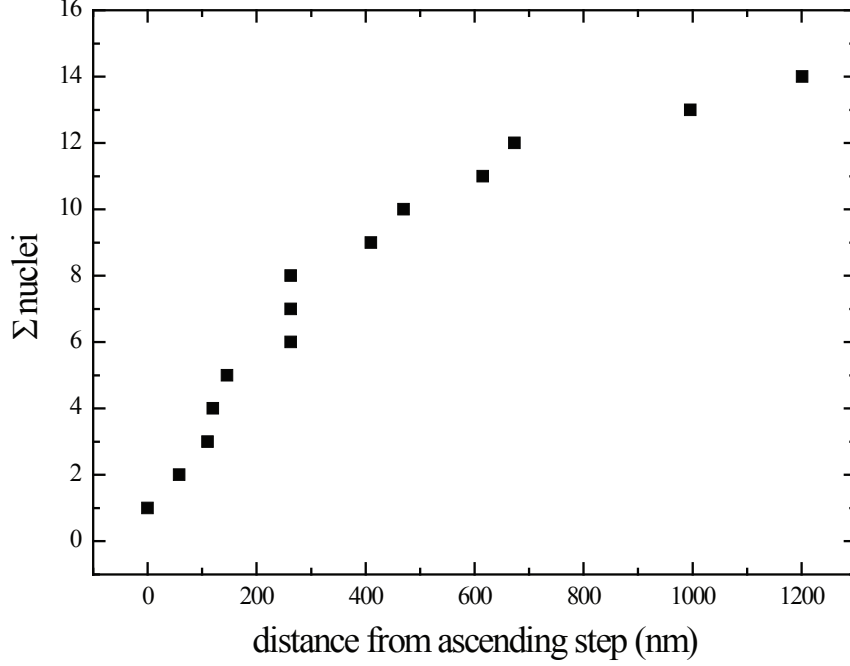
Figure 5.3: Integrated number of nuclei as function of the distance from the nearest ascending step from the experiment shown in Figs. 5.1 + 5.2(a). The average terrace width was about 900 nm.

higher slope at small distances to an ascending step, as compared to farther away. Despite the poor statistics, this shows a trend for nucleation closer to an ascending step. The same trend is obtained if we make the same plot as a function of the relative position on the terrace. Since the first suppresses and the latter enhances the effect, we are confident that it is real. Still, only one island nucleated right at a step edge, while most of them nucleated slightly in front of an ascending step. An explanation for this preference is a higher probability for downward as compared to upward diffusion over a step edge. During deposition of molecules, this would lead to a slightly increased molecular density close towards an ascending step resulting in an asymmetric density profile. Within classical nucleation theory, the nucleation rate J of 2D nuclei is proportional to [29, 48, 52]:

$$J \propto exp(-\frac{\pi \chi^2 \Omega}{kT \Delta \mu}), \tag{5.1}$$

where $\chi = 0.086\,\text{eV/nm}$ is the domains' line tension and $\Omega = 1.04\,\text{nm}^2$ is the area occupied per molecule in the c(8×8) structure. In Fig. 5.3, the nucleation rate (proportional to the slope of the curve therein) close to an ascending step is about a factor of 2 larger than farther away. Already a minute difference of 0.2% of $\Delta \mu$ explains the different nucleation rates. The correspondingly small differences in density are impossible to measure here

and can already be caused by a slight anisotropy in the down- and upwards diffusion of the molecules.

5.3.1 Supersaturation during nucleation

From the blue curve in Fig. 5.2(a), we can see that the first islands nucleated at a density of about 0.024 ML. After closing the shutter (t = 1660 s), the density drops exponentially to a constant value of 0.0231 ML within about 300 s. Therefore, the relative supersaturation was about 3.9% during the nucleation of the first islands. For an estimate of the chemical potential difference $\Delta\mu$ in the dilute phase during nucleation, we use the equation for an ideal gas [48, 49]:

$$\Delta\mu = kT \; ln(\frac{\theta}{\theta_{eq}}) \tag{5.2}$$

With the aforementioned numbers, this gives $\Delta\mu = 1.5 \pm 0.5$ meV. The dilute phase is quite dense, so one needs to be careful using Eq. 5.2, which is exactly valid only for an ideal (2D) gas. The biggest deviation will be due to mean field interaction and entropy effects [53, 78]. To account for these, a coverage dependent term $W(\theta)$ needs to be included in the chemical potential $\mu(\theta, T)$ of the dilute phase:

$$\mu(\theta, T) = -kT \; ln(\theta) + W(\theta) \tag{5.3}$$

Since the relative increase of density above the equilibrium value is still rather small, the difference $W(\theta_{eq}) - W(\theta)$ will to a good approximation cancel in $\Delta\mu$. The estimated value of $\Delta\mu$ (1.5 meV) is slightly smaller than the value measured during nucleation at lower temperatures (6 meV at 332 K) [78, 96]. This is to be expected, since, at a higher temperature and for the same deposition rate, nucleation occurs closer to equilibrium.

Using a classical nucleation model [29, 48], we expect a critical nucleus for this supersaturation on the order of $A_c = \frac{\chi\Omega}{\Delta\mu} = 10^4$ nm², where we used the BDA line tension of $\chi = 86$ meV/nm [78]. This is huge, and in principle the fluctuations are large enough to be observed, as we already did for critical fluctuations at lower temperatures [96]. However, here we did not observe any. This is attributed to two reasons: first of all, the nucleation rate is too low. The probability of observing more than one critical nucleus on a single terrace, which would compete directly for material from the dilute phase, is simply negligible. Secondly, and probably more important, the diffusion rate of molecules and the attachment-detachment kinetics are presumably faster

at 410 K than at lower temperatures. Subcritical nuclei grow and decay on much shorter time scales than at lower temperatures, and much faster than the frame rate of $0.5\,\mathrm{s}^{-1}$ we used here. While we observed some intensity fluctuations of the expected size during nucleation, the intensity changes were too small to attribute them unambiguously to critical fluctuations. This is consistent with short time scales and therefore only partial exposure in a single frame.

5.3.2 Secondary domain nucleation

The subsequent nucleation waves following the initial nucleation events (cf. Figs. 5.1 + 5.2(a)) are unexpected at first sight. In classic nucleation and growth, the few initial nuclei (islands 1-3 in Fig. 5.2(b)) would continuously grow until the complete area is filled, provided that the steps are permeable for individual BDA molecules. This situation, however, does not apply here. The Cu steps apparently provide a highly efficient way to block aggregation beyond steps, which is easily understood: Except for a potentially inhibiting height difference of about 2.08 Å per Cu step, the *fcc* structure of Cu imposes a registry problem. The c(8×8) registry is shifted by at least half a nearest neighbor distance in two ⟨110⟩ directions on adjacent terraces that are separated by a single step. Therefore, single steps impede the aggregation of BDA domains. In the case of a double step, this does not apply, but the height difference of 4.16 Å will effectively prevent growth across steps. Consequently, steps act as effective barriers for BDA domains, even when individual molecules can pass them. This implies that when a significant fraction of the domain boundaries of the initial nuclei is impinging on steps, further aggregation of BDA molecules is suppressed and the admolecule density rises again. Due to the size distribution of the Cu terraces, this will not happen simultaneously for all domains. At first, the increasing admolecule density will lead to an increased expansion rate of the still not step-bordered parts of domains. Finally, the supersaturation becomes large enough for the next wave of nuclei to form, reducing the admolecule density once again.

This process repeats until eventually all terraces are filled with domains. Between the first (islands 1-3) and second (islands 4-5) wave of nuclei, we observe a relatively long time scale with no further nucleation, while subsequent nuclei form at much shorter intervals within the FoV. After the initial nucleation, the different terraces are still connected with each other and can exchange molecules through diffusion. Different densities due to the local blocking/growth of domains are thus equilibrated and the density is approximately constant in the general area. The second nuclei form on a time scale

that is determined by the average Cu terrace size, i.e., when the first nuclei cover an entire terrace. In the later stage of the growth, a major fraction of the surface area is covered with c(8×8) domains, separating several areas from each other (see for example at t = 1350 s in Fig. 5.1). As a result, the admolecule densities in different areas become gradually decoupled from each other, since molecules cannot diffuse across domains. The subsequent nucleation events occur then at independent times, once the domains in the *local* area are mostly bordered (nucleation events 6-15 in Fig. 5.2).

The c(8×8) structure has 16 equivalent translational domains. In order to minimize the number of different domains in a network, the initial number of nuclei has to be well below the number of Cu terraces, as is the case in Fig. 5.1. One single domain will then develop on each terrace. However, macroscopically all variations will occur.

5.3.3 Wetting of steps

We now inspect the influence of the steps in more detail. Figure 5.4 shows a LEEM image that was recorded 800 s after closing the shutter of the Knudsen cell (cf. Fig. 5.1). It reveals a contact angle of the condensate with the Cu
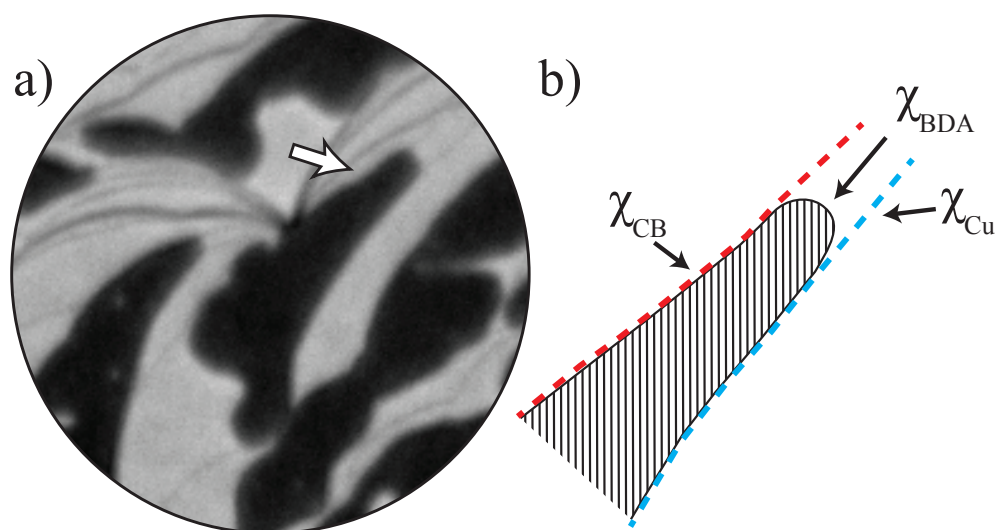
Figure 5.4: **(a)** LEEM image (FoV = 6 µm) taken 800 s after closing the shutter. The dark areas represent c(8×8) crystallites. The bright spots inside the domains are vacancy clusters that have reduced their edge length after coalescence (see Fig. 5.1). **(b)** Sketch of the region indicated by the arrow in (a). The dashed lines indicate descending (red, darker gray) and ascending steps (blue, light gray). χ_{CB}, χ_{BDA} and χ_{Cu} indicate the line tensions for the BDA covered step, the BDA domain boundary and the uncovered Cu step, respectively.

steps that is well above 150°. This observation is very significant. In three dimensions, the contact angle ϕ between a substrate and a film is given by Young's equation:

$$\cos \phi = \frac{\sigma_s - \sigma_i}{\sigma_f} \tag{5.4}$$

where σ_s, σ_i, and σ_f refer to the surface tension of the substrate, the interface and the film, respectively. In the present two-dimensional case, these are replaced by the line tensions of the free Cu step, the BDA covered Cu step and the BDA domain, respectively. A small value for ϕ is indicative for strong adhesion and wetting of the steps by BDA, while large ϕ values reveal a weak interaction and non-wetting. It is obvious from inspection of Fig. 5.4 that there is strong non-wetting, which is consistent with the observation that steps do not act as nucleation centers.

5.3.4 Growth instabilities

The growth of BDA/Cu(001) exhibits several instabilities, which we now consider in more detail. First, we examine an early stage of growth, as depicted in the second snapshot of the top row in Fig. 5.1. It shows two nuclei that are compact. A more detailed inspection of the evolution of the right domain is shown in the top panel. Protrusions develop that evolve into a ramified shape. This behavior is characteristic of a Mullins-Sekerka growth instability: protrusions capture material from an area with a larger solid angle. In the BDA/Cu(001) system, the protrusions will be strongly enhanced because the mobility along the edges of BDA domains is extremely low. Edge molecules are alternatingly placed in an orientation perpendicular and parallel to the edge along the $\langle 110 \rangle$ directions, as shown in Fig. 5.5. Movement along such edges involves detachment, diffusion in the vicinity of the edge and reattachment at an appropriate position. For ideal $\langle 110 \rangle$ oriented edges, an additional rotation of the molecule in the dilute phase is required. Along a perfect $\langle 100 \rangle$ oriented step, all molecules are oriented parallel. A diffusing molecule will have only parallel binding partners and be weakly bound, while reattachment requires a rotation of the molecule in the dilute phase. In either case, mass transport along the BDA domain edges will be slow and the MS instability criterion is therefore well met. In more advanced stages of growth, protrusions of the domain will impinge on steps (arrows Fig. 5.1) where further growth is inhibited. The final result is that all domain boundaries impinge on steps and follow the smooth contour of the step.

Figure 5.6 presents the shape evolution of the BDA island shown in the center panel of Fig. 5.1. Each color represents the island shape after an incremental 20 s. If we concentrate on the growth along the right side of the
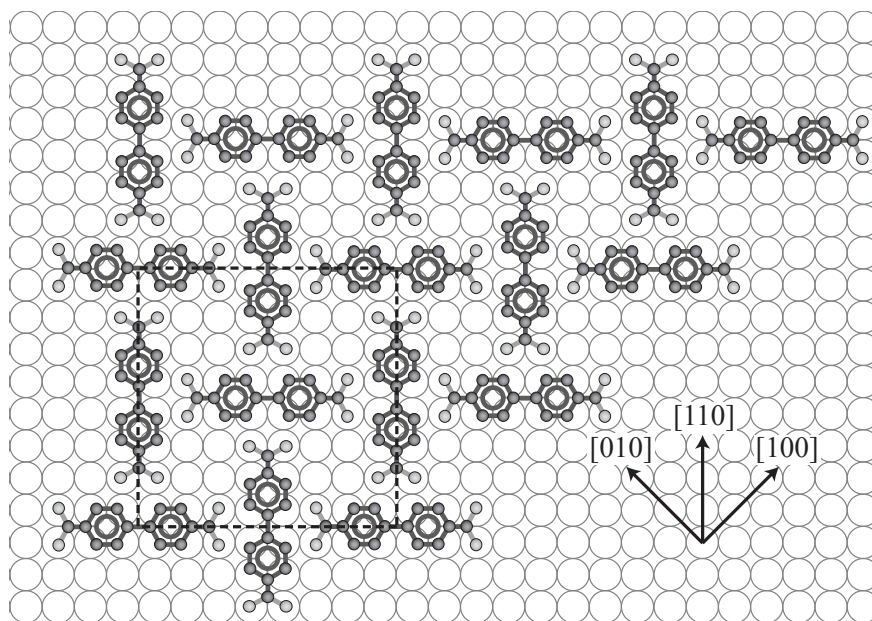
Figure 5.5: A sketch of the BDA molecules in the c(8×8) structure, with the unit cell shown by the dashed square. The crystallographic azimuth directions on Cu(001) are shown in the inset.

lower Cu step, we can see that the domain growth rate is very fast, much faster than the growth rate away from the step towards the terrace (cf. red arrows in Fig. 5.6). For the growing domain front at the step, the solid angle for accepting incoming admolecules is over 270°. Note that the steps are permeable for individual admolecules. For the material arriving within the remaining 90°, the front competes with domain boundaries further towards the interior. The solid angle that is available for diffusing species is thus very large, which can result in extremely fast growth. Even at a very low deposition rate of 3.2×10^{-5} ML/s, domain boundary growth rates of 25-50 nm/s have been observed. The very different growth rates may even result in the formation of vacancy clusters (cf. white arrow in Fig. 5.6). Clearly, this growth instability fulfills all requirements of a MS growth instability. The edge mobility is still extremely low, as explained above, whilst the accumulation of isoconcentration lines around the protrusion is extremely high. The latter is enhanced by the fact that the surrounding BDA domain boundaries are no longer able to accommodate BDA molecules because they are limited by the Cu steps. Counter intuitively, the fast growth direction is however along the step, instead of the more common direction perpendicular to the steps. This unexpected growth behavior is a direct consequence of the underlying physics: a non- or only weak wetting of steps. It should be of general importance for a wide range of molecular film systems, in which the affinity of molecules for steps is less than that for molecular domains. It is also of
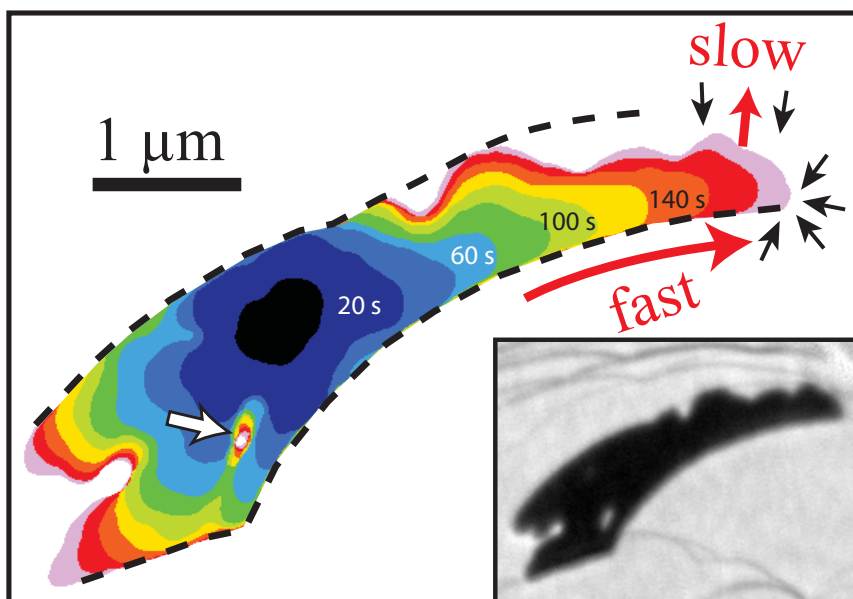
Figure 5.6: Color coded shape evolution of the island shown in the top panel of Fig. 5.1. Each color represents the island shape after a time increment of 20 s. Dotted lines indicate bordering Cu steps. The fast wetting *along* steps can be seen at the right side of the lower step. The conventional MS instability can be seen for the much slower growth *away* from the step. Red (gray) arrows indicate the domain expansion rate, black arrows the BDA admolecule flux. The white arrow marks the inclusion of a vacancy hole. The inset shows a LEEM image of the island at the latest stage.

more general importance for film morphology, since it will lead to defects (holes and vacancy clusters) in extended supramolecular networks.

5.4 Conclusions

In conclusion, we have reported a number of surprising anomalous features for the growth of BDA on Cu(001). The features are of more general interest, since these results are representative for a frequently studied class of supramolecular networks constituted by benzoic acids on metal surfaces. We find that at sufficiently high temperatures substrate steps are permeable for individual molecules. At the same time, steps raise an effective barrier for the expansion of BDA domains. No indication for preferential nucleation at steps or defects is found. Nucleation occurs in "waves": once the first nuclei cover their respective terraces, the supersaturation of the dilute phase increases again, inducing secondary nucleation. While the first and second waves are synchronized in time, subsequent nucleation events happen at random, as the admolecule densities in different areas become separated by existing BDA domains. A high temperature (410 K for BDA/Cu(001)) is needed to guarantee that each individual terrace is covered by one sin-

gle BDA domain, which is minimizing the number of translational domains present on the surface. We found strong MS-type growth instabilities: the ramification of initially compact islands is observed and a fingerlike growth occurs in screened regions of terraces. Both are consistent with a strongly suppressed diffusion along the domain boundaries. We also report an as yet unknown MS-type growth instability that is related to an anomalous growth rate of domains along Cu steps. These growth instabilities lead to coalesce and residual vacancy clusters in the domains, which causes defects in the otherwise ideal BDA domains.

6

Formation and decay of a compressed phase of BDA on Cu(001)

The molecular structure of 4,4'-biphenyldicarboxylic acid (BDA) on Cu(001) has been studied at high coverage and relatively high temperature ($\sim 400\,\mathrm{K}$) using Low Energy Electron Microscopy, LEEM, and selected area diffraction, µLEED. Next to the previously reported c(8×8) structure, we also observe a compressed phase with a $\left(\begin{smallmatrix} 5 & -7 \\ 5 & 4 \end{smallmatrix}\right)$ superstructure in matrix notation. All four equivalent (rotational and mirror) domains are equally populated. Both the c(8×8) and the compressed phase are confined to the first layer and the latter has a 14% higher density compared to the c(8×8) phase. Remarkably, this compressed phase is stable only during deposition and decays after interruption of the deposition. Apparently, the density of physisorbed admolecules on top of the c(8×8) layer has to be above a relevant threshold to allow the formation of the compressed phase.

6.1 Introduction

The structure in which large molecules order on metal surfaces depends strongly on the interplay between intermolecular (intralayer) energies, binding (interlayer) energies and entropy [97, 98, 99, 100, 101]. For example, molecules without any functional groups, which could mediate an attractive molecular interaction, often interact repulsively with each other and try to maximize their lateral distance. At low coverages this results in the formation of a disordered gas phase, while for high(er) coverages the molecules order without forming islands [102, 101, 103]. On the other hand, molecules with functional groups that allow the formation of molecule-molecule bonds, form ordered structures (islands) already at low coverage, due to an attractive interaction force. A typical example for the latter are benzoic-acids, where the functional carboxylic acid groups are actively involved in the formation of hydrogen-bonds between adsorbed molecules. In this case, the formation of large, well-ordered supramolecular networks is regularly observed [10, 11, 13, 14, 15, 16, 17, 18, 19, 78].

In previous studies it was often found, that also these structures formed by the molecules depend strongly on coverage. With increasing coverage the molecules order in increasingly dense structures. By squeezing more molecules into the layer, the system gains total free energy, even though this decreases the average binding energy of the molecules. For example, Ye et al. [104] observed different structural phases of trimesic-acid on Au(111). At low coverage the molecules formed open molecular networks, which converted into more closely packed structures with increasing coverage. The molecules interacted less and less through the formation of energetically favorable dimeric hydrogen bonds, and formed rather cyclic hydrogen bonds in increasingly denser structures. Also, different structures due to different degrees of deprotonation at higher coverages were observed [99]. The molecular overlayers are often commensurate with respect to the substrate lattice at low coverages. On the other hand, incommensurate (or higher order commensurate) overlayers are found at higher coverages [105, 100]. While this reduces the average binding energy, it increases the total free energy: the commensurate, relaxed, layer is forced into a compressed structure, due to the typical strong interaction of the (chemisorbed) molecules with the substrate, which is often much stronger than the interaction between adsorbed molecules. For the system as a whole, it is thus energetically favorable to pay some price in binding energy by reducing attractive intermolecular interaction (e.g., reduce the number of dimeric hydrogen bonds [104]) and

gain total free energy by increasing the number of molecules in the surface confined layer.

Understanding the interplay between the different energies is crucial to gain control over the nanostructures formed by the molecules. The goal in molecular epitaxy is to obtain tailored structures with the lowest number of defects, which may be vacancies in the layers, but also domain walls. Therefore, a high growth temperature (relative to the intermolecular interaction) is usually advisable to decrease the nucleation density to the point where only one nucleus forms per substrate terrace (cf. Chapter 5).

Here, we present a low energy electron microscopy (LEEM) and selected-area diffraction (µLEED) study on the formation and decay of a compressed structure for high coverages of 4,4'-biphenyldicarboxylic acid (BDA) on Cu(001). BDA is a linear molecule approximately 1.15 nm in length. It consists of two phenyl rings and two functional carboxylic acid groups, each at opposite ends of the molecule. The molecule is a typical building block used for the formation of supramolecular or metal-coordinated networks on metal surfaces [12, 26, 43, 25, 19, 44, 38, 78]. On Cu(001) at or above room temperature, BDA adsorbs in a flat lying geometry with the carboxylic acid groups deprotonated [106, 11, 107]. At low BDA coverage, the molecules form a 2D dilute phase without long range order. If this dilute phase reaches a critical (temperature dependent) density, molecules start to form large supramolecular networks, which can extend over entire Cu terraces [12, 38, 78, 96]. In these networks, the molecules form a c(8×8) superstructure on the Cu(001) lattice. The superstructure is commensurate: each molecule in the structure is adsorbed at an equivalent position on the Cu(001) lattice. Neighboring molecules in the structure are rotated by 90° (cf. Chapter 3) and interact through the formation of hydrogen bonds between the deprotonated carboxyl groups and the phenyl rings of the adjacent molecules. One molecule occupies 16 Cu(001) unit cells (1.04 nm^2) in this structure. In a previous study, we determined the 2D cohesive energy of the molecules in the networks to be $E_C = 0.35$ eV [78]. At the substrate temperatures employed in this study, the density of molecules in the dilute phase is between 10% and 30% of the density in the c(8×8) structure. The molecular networks cannot grow across Cu steps, the growth of domains gets efficiently terminated as they reach steps, due to registry conflicts on the *fcc* (001) surface. In contrast to this, steps are permeable for individual molecules (cf. Chapter 5). For a wide range of BDA coverage and temperatures, the c(8×8) structure is the only solid phase we observe.

Here, we show that for high coverages and high substrate temperatures a compressed phase forms, with a higher order commensurate superstructure.

The compression starts by a conversion of the c(8×8) structure in the center of large domains during deposition. The compressed phase is not stable, it transforms slowly back into the c(8×8) phase upon interruption of the deposition.

6.2 Experimental

Experiments were performed in an Elmitec LEEM III microscope [32] with a base pressure of about 1×10^{-10} mbar. A Cu(001) single crystal with a miscut angle less than 0.1° was used [37]. Prior to mounting, it was annealed at about 1170 K in an Ar-H$_2$ mixture for a prolonged period to deplete the bulk of the crystal from sulphur contamination. After insertion into the microscope, the sample surface was further cleaned by cycles of sputtering with hydrogen [39], argon, and annealing at 900 K. BDA in powder form (purity > 0.97, TCI Europe, CAS: 787-70-2) was deposited from a Knudsen cell. Deposition rates between 2 and 5 $\times 10^{-5}$ monolayers (ML) per second were used, where a monolayer is defined as one BDA molecule per Cu(001) unit cell. With this definition, the c(8×8) structure completely covers the surface at 0.0625 ML. LEEM images were recorded with a 25 µm illumination aperture and were background corrected by applying a flat field correction. No indications for beam damage induced to the molecular networks were observed (see also Chapter 2). We inserted illumination apertures in the incoming electron beam path for selected area diffraction (µLEED). Apertures with diameters of either 1.4 µm or 25 µm were used to spatially resolve the surface structure. The µLEED patterns were corrected for a cloud formed by secondary electrons using the procedure described in Chapter 2. During deposition, the sample temperature was kept at the values mentioned in the text, always well below the temperature of 450 K, at which we start to observe degradation of the films, presumably due to substrate assisted decomposition.

6.3 Results and Discussion

6.3.1 Formation of the compressed phase

We start by describing an experiment in which we have grown a closed layer of the c(8×8) phase at a substrate temperature of 420 K using an average BDA deposition flux of 4 $\times 10^{-5}$ ML/s. A LEEM image sequence showing the completion of the first BDA layer is given in Fig. 6.1. The light gray areas
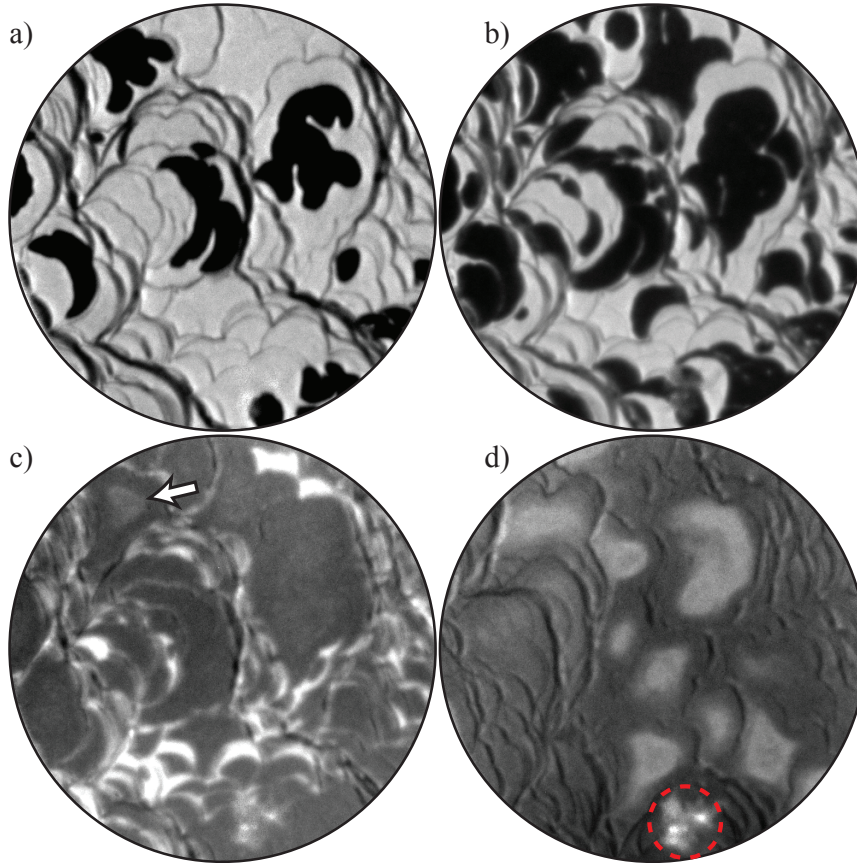
Figure 6.1: LEEM images showing the completion of the first BDA layer on Cu(001) during growth at a temperature of 420 K. Cu terraces appear light gray and c(8×8) BDA islands dark. Thin lines in **(a)** and **(b)** are Cu steps, thicker lines step bunches. BDA coverage is increasing from **(a)-(d)**. The arrow in **(c)** shows the formation of a second phase within the existing BDA islands upon closing of the c(8×8) layer. The new phase appears lighter than the surrounding island for the given imaging conditions. The start voltage was 2 eV for **(a)-(c)** and 2.3 eV for **(d)**. The dashed circle marks a defect on the micro-channel plate detector which appears bright. Image contrast was adjusted for each image. Field of View (FoV) is 10 μm.

in Fig. 6.1(a)+(b) are Cu terraces covered with a BDA dilute phase [78] and the dark areas are BDA c(8×8) islands, which was verified with μLEED. The thin curved lines are Cu steps and thicker curves are step bunches. In the first two images (Fig. 6.1(a)+(b)), we can see how the first BDA domains get blocked in their growth by Cu steps, and the resulting island shapes follow the shape of the underlying Cu steps. The termination of domain expansion induces reentrant nucleation of domains on neighboring terraces (cf. Chapter 5). In the third image (Fig. 6.1(c)) almost the entire surface is covered with BDA c(8×8) domains. The arrow in Fig. 6.1(c) marks a triangular area, where a light contrast developed in one of the larger domains. The contrast first appeared in the center of that domain, whose expansion was already terminated by steps earlier in the growth process. The shape

of the lighter area roughly mimics the shape of the surrounding domain. In the last image (Fig. 6.1(d)) the c(8×8) layer is closed and all of the larger domains developed the light contrast in the center. The lighter areas are growing in size with further BDA deposition. It is thus evident, that the lighter areas are representing a second layer forming either on-top of the c(8×8) layer, or a compressed surface confined phase that formed due to the pressure exerted by admolecules adsorbed on-top of the domains. Our further findings, which we present in the following, strongly hint at a compressed phase. For clearness, we will thus denote the newly emerging structure as the "compressed" phase for the remainder of this chapter.
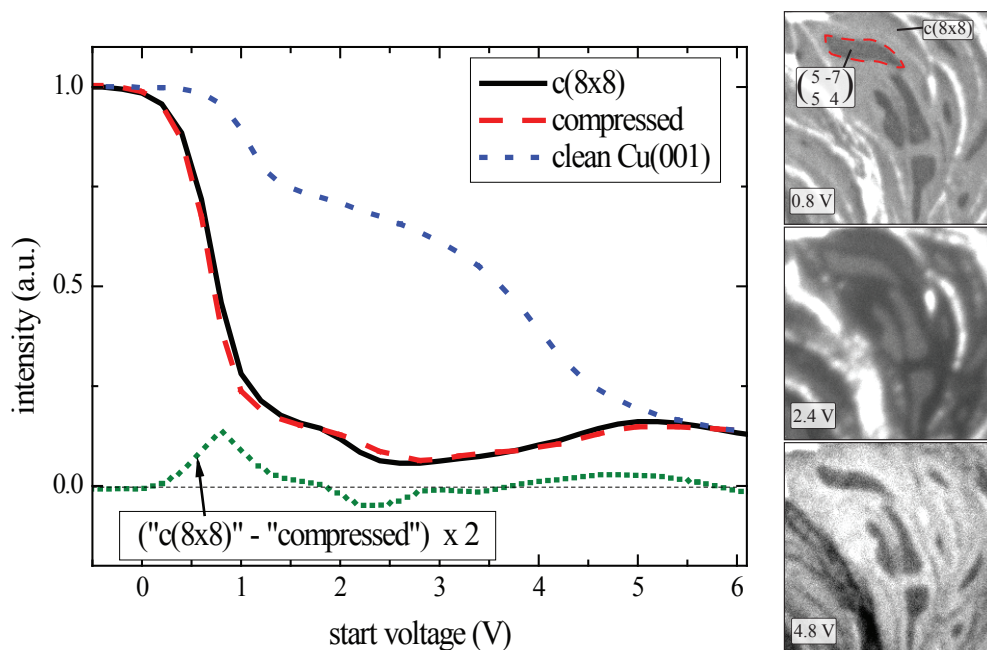

Figure 6.2: Image intensity versus start voltage (LEEM IV) plots obtained from different areas: c(8×8) (black, solid), compressed phase (red, long dashed), and clean Cu(001) (blue, short dashed). The difference between the first two is plotted as the green dotted line at a two times magnification. The LEEM images on the right show the surface at start voltages for which the difference is maximal (FoV 4 µm). For 0.8 eV and 4.8 eV the compressed phase is darker, and for 2.4 eV lighter than the surrounding c(8×8) phase. The red dashed line in the first snapshot indicates the border of the compressed phase.

The contrast between the compressed and the regular c(8×8) areas depends heavily on electron energy (start voltage). In Fig. 6.2, we analyzed the electron reflectivity of the two phases as a function of start voltage (LEEM IV). At first sight, the two curves fall almost perfectly on top of each other. This is consistent with the presence of a compressed phase and not a second layer, for which we would expect features (peaks) at energies different from the peaks of the c(8×8) phase. Small differences between the curves give rise to the observed contrast in Fig. 6.1, which is more clear in the plot of the

difference between both curves in the same figure. The difference between both curves is largest for start voltages of 0.8 V, 2.4 V and 4.8 V. While the compressed phase appears dark for 0.8 V and 4.8 V, the contrast is inverted for 2.4 V. Exemplary LEEM snapshots of both phases taken at the three respective start voltages are shown in the right hand part of Fig. 6.2.
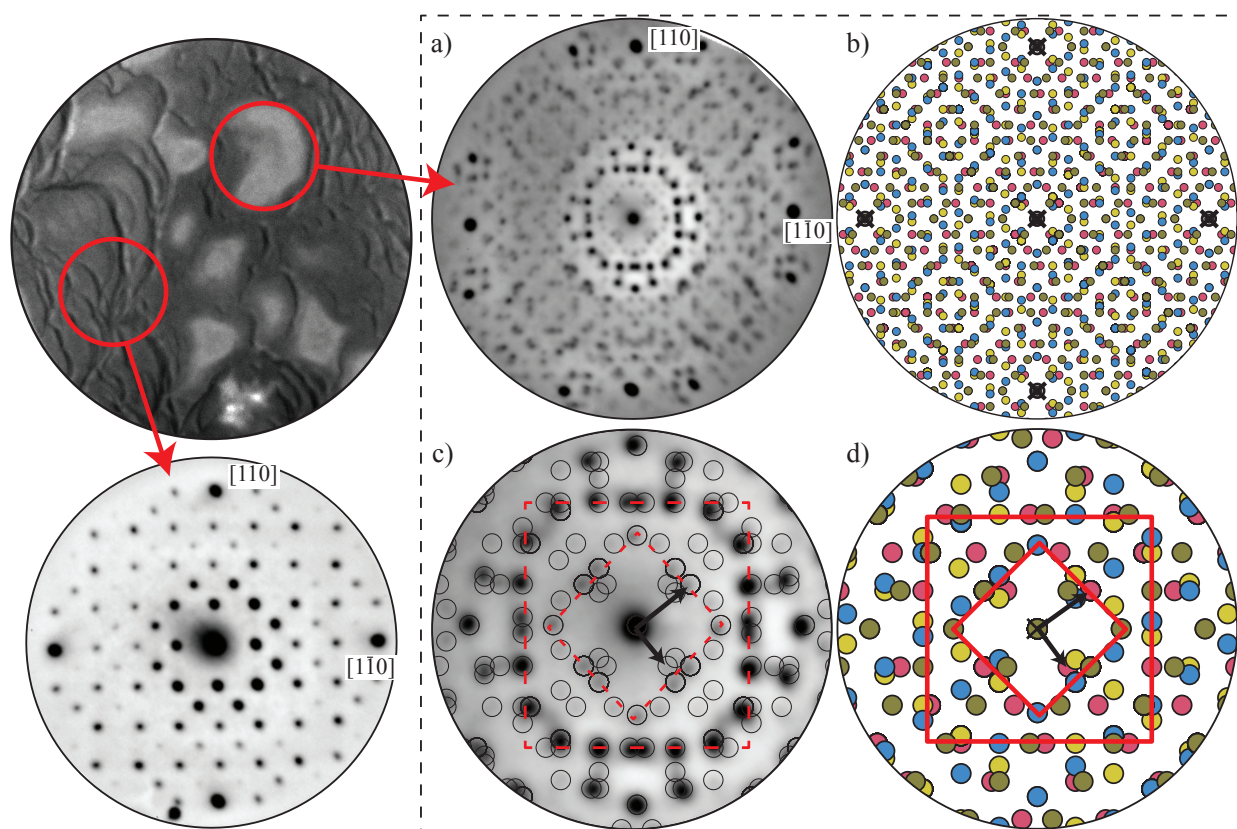
6.3.2 µLEED structure analysis

Figure 6.3: µLEED analysis of Fig. 6.1(d). The darker areas show the c(8×8) pattern, while the lighter areas show a new diffraction pattern. **(a)** Cumulative (background corrected) µLEED pattern obtained from the lighter phase by summing up patterns for electron energies from 5 eV to 36 eV at 1 eV spacing. The complex diffraction pattern can be described with a superposition of four equivalent domains, of which one is a $\left(\begin{smallmatrix} 5 & -7 \\ 5 & 4 \end{smallmatrix}\right)$ overlayer in matrix notation. A calculation of the pattern is shown in **(b)**. Each color (gray tone) represents one of the four domains. **(c)** and **(d)** show the inner part of **(a)** and **(b)** enlarged. The calculated positions of spots are superimposed in **(c)** as black circles. Without exception we found experimentally finite intensity at these positions, even when sometimes very weak. Black arrows indicate the unit vectors of the $\left(\begin{smallmatrix} 5 & -7 \\ 5 & 4 \end{smallmatrix}\right)$ superstructure, red dashed squares are guides to the eye.

After stopping the deposition of BDA molecules, we analyzed the layer shown in the last image of Fig. 6.1 using µLEED. We restricted the electron

beam to an area of 1.4 μm diameter on the surface by introducing an illumination aperture. When we selected the darker areas of the layer in Fig. 6.1(d) under the aperture, we observed the regular c(8×8) superstructure without any additional spots [38]. An example of the corresponding LEED pattern is presented in Fig. 6.3. However, if we selected one of the lighter areas (i.e., the compressed phase), we observed a new, highly complex pattern, which we didn't observe before at lower coverages and neither at temperatures below $\sim$ 350 K. In Fig. 6.3(a) we present a (background corrected) cumulative μLEED pattern, which we obtained by summing up individual patterns for electron energies from 5 eV to 36 eV at 1 eV spacing. The pattern is four-fold symmetric and the underlying structure is commensurate, like the c(8×8) structure. This can be seen by the repetition of the pattern around each of the four first order Cu(001) substrate spots. While the pattern appears highly complex at first sight, it can be nicely described by the superposition of four equivalent domains. One of the domains can be described with a $\left(\begin{smallmatrix} 5 & -7 \\ 5 & 4 \end{smallmatrix}\right)$ superstructure in matrix notation, with the [110] and [1$\bar{1}$0] substrate directions as a base. A calculation of the corresponding pattern is shown in Fig. 6.3(b) and (d), with the spots belonging to each of the four rotational domains in the same color (gray tone). Figures 6.3(c) and (d) show the inner part of the pattern at a higher magnification. Additionally, we superimposed the expected position of spots on the diffraction pattern in Fig. 6.3(c). All spots that carry intensity were traced back in the calculated diffraction pattern.

The diffraction pattern is quite characteristic and since we observe the superposition of four equivalent domains, already a slightly different overlayer structure would produce a very different pattern. Interestingly, we observed no intensity at the expected positions of the c(8×8) structure. Together with the similar LEEM IV characteristics (cf. Fig. 6.2), this is strong proof for another surface confined layer phase and not a second layer on-top of the c(8×8) domains. Since this phase forms at higher BDA coverages, molecules are packed in a denser way in the emerging structure. The $\left(\begin{smallmatrix} 5 & -7 \\ 5 & 4 \end{smallmatrix}\right)$ unit cell covers an area of 55 Cu(001) unit cells, which is 14% smaller than the unit cell of the c(8×8) structure, which covers 64 Cu(001) unit cells.

To clarify the question, whether the conversion into the compressed phase occurs through a gradual compression of the c(8×8) structure or through the nucleation of the compressed phase, we also followed the conversion in-situ in reciprocal space with μLEED. Figure 6.4 shows the development of the diffraction pattern with increasing BDA coverage at an electron energy of 6 eV and at a substrate temperature of 400 K. The patterns were obtained with a large illumination aperture that limited the beam to an area with 25 μm diameter on the surface (compared to 1.4 μm in Fig. 6.3). In the first
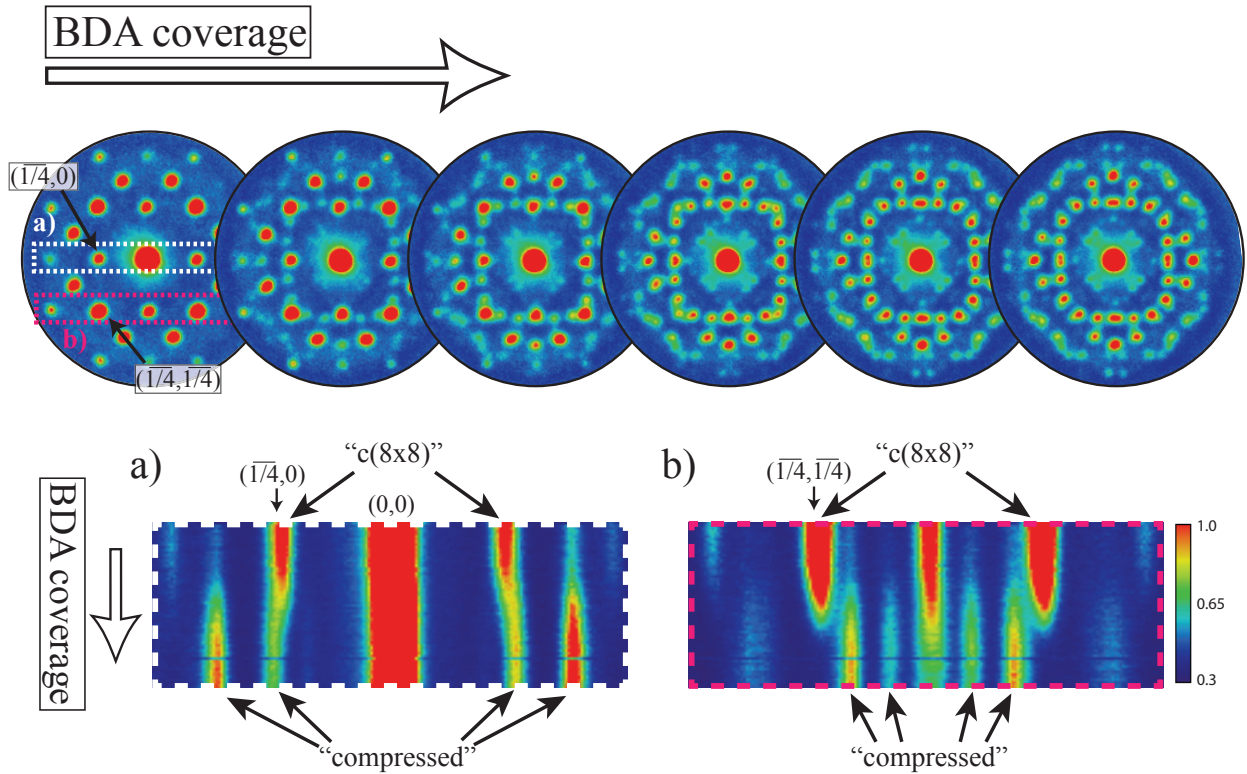
Figure 6.4: **Top:** Conversion of the c(8×8) phase into the compressed phase with increasing BDA coverage as seen in µLEED at an energy of 6 eV and a temperature of 400 K. In the pattern on the left only the c(8×8) is visible, which completely vanished upon conversion in the rightmost image. The dashed rectangles mark the areas used for linescans in the lower part of the figure. **(a)** Shows line profile versus coverage plots through the $(0,0)$ and $(\overline{1/4},0)$ spots (white dashed box), **(b)** parallel to the same direction through the $(\overline{1/4},\overline{1/4})$ - c(8×8) spot (pink (gray) dashed box). The relative intensity color code is explained on the right hand side.

pattern of the sequence, the only ordered structure on the surface was the c(8×8) phase. As we started to deposit more BDA, the coverage increased, and the spots which belong to the compressed phase appeared and gained intensity. At the same time, the c(8×8) diffraction spots lost intensity, until they completely vanished for the highest coverages.

The lower part of Fig. 6.4 shows line profiles as a function of BDA coverage. Figure 6.4(a) shows line profiles through the $(\overline{1/4},0)$ and $(0,0)$ c(8×8) spots, Fig. 6.4(b) along the same direction but through the $(\overline{1/4},\overline{1/4})$ c(8×8) spot. In Fig. 6.4(a), the center of the $(\overline{1/4},0)$ spot seems to move continuously with increasing coverage to a position that belongs to the pattern of the compressed phase. This would point at a gradual compression of the c(8×8) overlayer with increasing coverage. However, this is actually a coincidental effect, since both spots are close to each other and overlap partially. In the line profile through the $(\overline{1/4},\overline{1/4})$ spot (Fig. 6.4(b)), we can see that the

$(\overline{1/4},\overline{1/4})$ c(8×8) spot is not moving at all as it vanishes. The closest spots belonging to the compressed phase appear simultaneously, also at a fixed position. Thus, both structures form distinct phases and the conversion is not proceeding through the continuous compression of the c(8×8) phase, but rather through the nucleation of the compressed phase within the c(8×8) domains.

6.3.3 Molecular structure in the compressed phase

We will now discuss the possible arrangement of the BDA molecules in the compressed structure. From the µLEED patterns we found a $\left(\begin{smallmatrix} 5 & -7 \\ 5 & 4 \end{smallmatrix}\right)$ overlayer structure. Compared to the c(8×8) structure, the unit cell of this overlayer is both rotated and compressed (see Fig. 6.5(a)). The compressed unit cell covers 55 Cu lattice cells, compared to 64 for the c(8×8). Since the structure forms upon increasing the coverage (locally) beyond the c(8×8) coverage, the molecular density should be higher than in the c(8×8) phase. In the c(8×8) unit cell one molecule occupies 16 Cu(001) unit cells ($1.04\,\mathrm{nm}^2$). Assuming that all molecules adsorb in a flat lying geometry, which is expected given the anticipated strong interaction of the carboxylate groups with the substrate, four molecules fit into the compressed unit cell. As already mentioned, this would correspond to a 14% compression, i.e., 13.75 Cu(001) unit cells ($0.89\,\mathrm{nm}^2$) per molecule, compared to 16 in the c(8×8) structure.
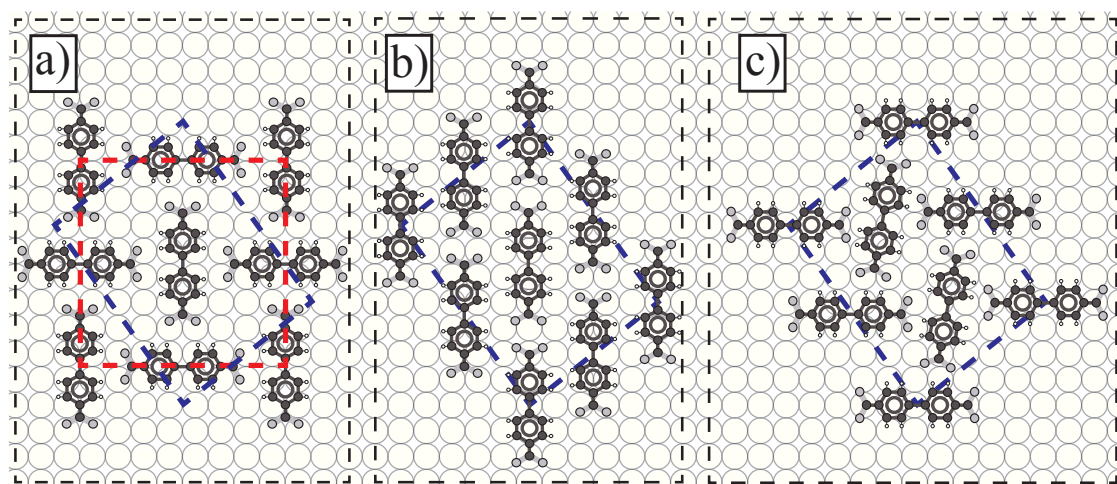
Figure 6.5: **(a)** Sketch of the uncompressed c(8×8) BDA structure. The red dashed square shows the c(8×8) unit cell, the blue dashed rectangle the $\left(\begin{smallmatrix} 5 & -7 \\ 5 & 4 \end{smallmatrix}\right)$ superstructure. **(b)** Sketch of one possible configuration in the compressed phase: a close packed structure with all molecules oriented in the same direction, similar to BDA phases observed on Au(111) or HOPG [43, 108]. **(c)** Other possible compressed structure, similar to the c(8×8) structure, but with the molecules slightly rotated and at smaller distances. Note, that in both (b) and (c), the molecules in the unit cell are adsorbed on different substrate lattice sites.

The four molecules can fit into the compressed unit cell in several different ways and orientations. While in principle, we should be able to get more information on the orientation of the molecules from the µLEED intensity distribution, this analysis is complicated here by the possibly also coherent superposition, of four equivalent domains (see Fig. 6.3). The intensity distribution is to a large degree determined by the addition of intensities from different rotational domains. Equivalent spots from all four domains have identical intensity, even with the smallest illumination aperture of 1.4 µm diameter. The compressed areas inside of the domains consist of several small equivalent domains, with no apparent preference for a specific orientation.

Without microscopic information on a molecular scale, we can only speculate how the molecules are oriented in the unit cell. Two possible and reasonable structures are presented in Fig. 6.5(b) + (c). In both examples, the four molecules are not on identical positions on the Cu(001) lattice, so a reduction to a smaller unit cell is not possible. The compressed structure is commensurate to higher order, while the c(8×8) structure is commensurate to first order, i.e., all molecules are adsorbed on identical Cu(001) lattice sites.

One possible structure is a close packed structure, which is shown in Fig. 6.5(b). The molecules in this structure are arranged similar to BDA structures observed on Au(111) (see Chapter 7) or HOPG [43, 108]. In the latter structures, the molecules interact through dimer hydrogen bonds between the *protonated* carboxylic acid groups. This bonding motif would not be possible here, since the molecules are *deprotonated*. Rather they would need to form hydrogen bonds to the next lateral neighbor, similar to the mutual interaction of terephtalic acid on Cu(001) [11]. Of course, this means a much weaker molecular interaction than in the c(8×8) structure. Additionally, the negatively charged carboxylate groups are quite close together, which could involve large repulsive electrostatic forces. The formation into this close packed structure from the c(8×8) phase, would also require large mass transport to allow the rotation of molecules by 90°.

The transformation is not a problem in the case of the open structure shown in Fig. 6.5(c). This structure is very similar to the c(8×8) structure. Thus, the conversion between both phases only involves a minimal rotation and movement of molecules. The basic building block, two molecules rotated now by approximately 90°, are the same in both the relaxed and compressed structures. Also, the carboxylate groups are still pointing towards the positively polarized hydrogen atoms on the phenyl rings of the neighboring molecules, which allows for a remaining interaction between molecules. Therefore, we tend to favor this latter structure.

Irrespective of the actual structure in the compressed phase, the higher order commensurability will reduce the average binding energy per molecule in the compressed, surface confined layer compared to the c(8×8) layer. However, the densification still reduces the total free energy, due to the increased number of molecules that can make contact to the substrate, which ensures a stronger binding than in the physisorbed state on top of the c(8×8) layer.

6.3.4 Dynamics of the phase conversion

After closing the shutter the compressed phase is not stable and slowly converts back to the c(8×8) structure. The formation and subsequent decay of the compressed phase is shown in a clear way in the image sequence presented in Fig. 6.6. The experiment was performed at a substrate temperature of 378 K and a start voltage of 0.8 V, for which the compressed phase appears darker than the surrounding c(8×8) islands. The first image in Fig. 6.6 (t = 0 s) shows the surface after deposition of an initial amount of BDA (approximately ~ 0.5 BDA molecules per nm^2) and waiting for >1000 s with the shutter of the BDA source closed. At this point, slightly less than 40% of the surface is covered by solid c(8×8) domains. Some of the domains show the compressed phase in the center (see e.g. island indicated by the arrow). At t = 0 s we opened the shutter again for 60 s, and molecules are deposited at an estimated rate of 5×10^{-5} ML/s. The images directly after opening the shutter show two effects: several new, small c(8×8) domains nucleate within the dilute phase on the Cu terraces due to the increased supersaturation. At the same time, the contrast of the c(8×8) islands turns dark, and the compressed areas are growing, which appear dark for the start voltage used here (cf. Fig. 6.2).

After closing the shutter (t = 60 s), the contrast increases again, beginning from the rim of the domains. At about t = 160 s - 260 s we can clearly distinguish the two different phases: the compressed phase is in the center of larger islands, surrounded by a rim of the c(8×8) phase. The interface between both phases appears sharp - no contrast gradients are resolved. The shape of the compressed phase follows the shape of the island, with the distance to the outside border of the surrounding island being almost constant. As we wait with the shutter closed, the compressed phase completely decayed after about 1500 s. Several of the smaller c(8×8) islands in the vicinity grew at the same time. Also the larger islands grew, though, only where they were not bordered by underlying Cu steps. The material from the compressed phase is apparently incorporated into the c(8×8) domains in the surrounding ar-
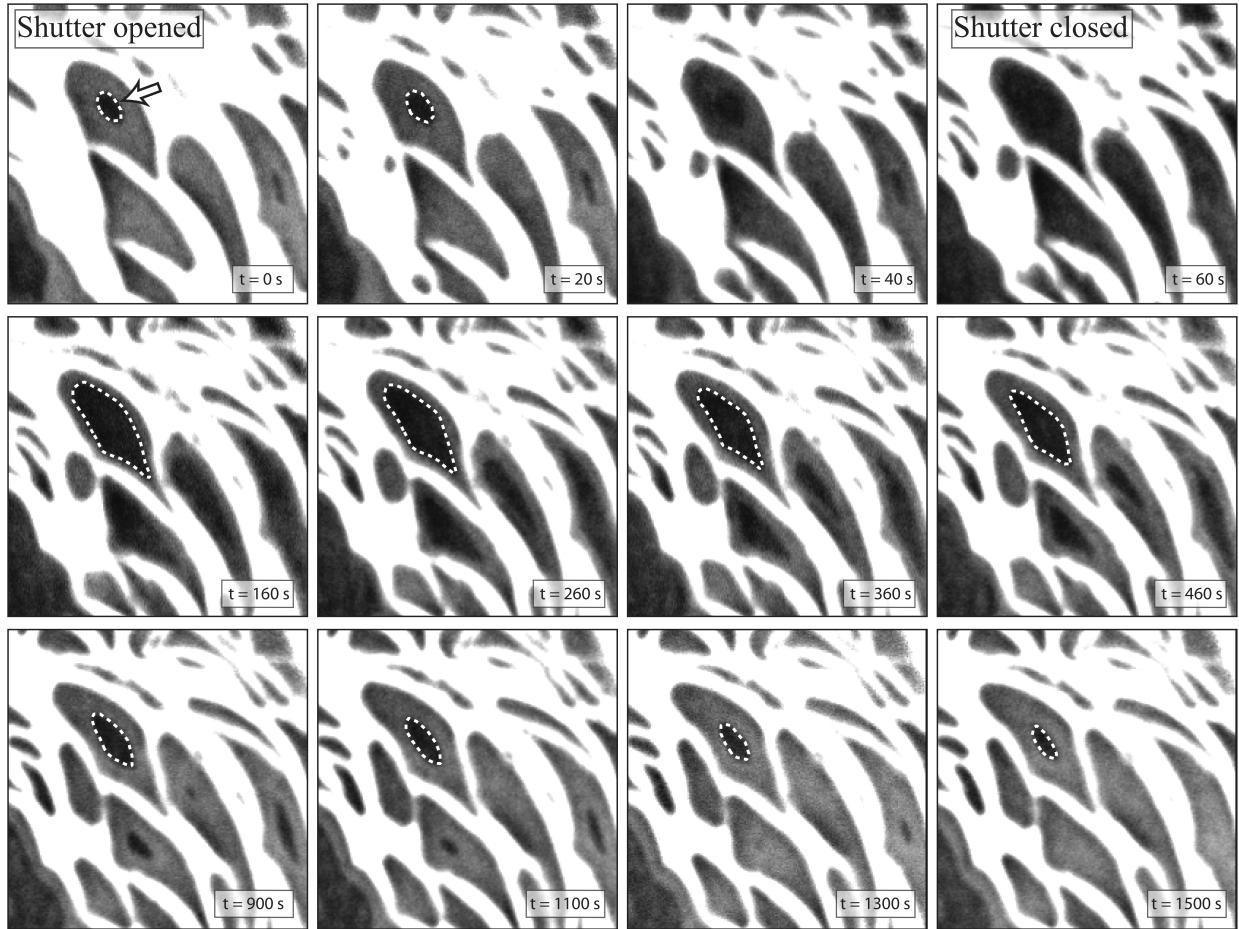
Figure 6.6: LEEM image sequence (FoV 4 μm, start voltage 0.8 V) showing the formation and decay of the compressed phase. We deposited additional BDA on a surface covered with large c(8×8) domains at a temperature of 378 K. Approximately 1000 s before the first image, BDA deposition was stopped. White areas are Cu terraces just filled with the dilute phase, gray areas are the c(8×8) structure and the darker gray areas represent the compressed phase. The arrow in the first image shows remainders of the compressed phase from the initial growth. The compressed area for this island is additionally marked with white dashed line in the sequence, where clearly distinguishable. The shutter of the BDA source was opened at $t = 0$ s and closed at $t = 60$ s, with an estimated deposition rate of 5×10^{-5} ML/s. Immediately after opening the shutter, the contrast of the islands turns dark, the compressed areas increase and several new BDA domains nucleate on the Cu terrace. After closing the shutter the contrast on the islands slowly lightens, starting from the outside rim of the domains.

eas. We also observed indications for material desorbing back into vacuum, however, with desorption rates which were very low (on the order of a small fraction of a monolayer per hour).

An obvious next step, is a comparison of the c(8×8) domain size increase relative to the area initially occupied by the compressed phase. This would allow a determination of the molecular density in the compressed structure. We did so for several different experiments and found densities varying between 1.1 and 2 times the c(8×8) density for the compressed structure. The problem with this analysis are the many small BDA domains that nucleated on small terraces formed by step bunches and whose area increase is hard to quantify. The latter is due to electron lensing effects at the edge of the BDA domains caused by the work function differences between Cu substrate and BDA [79]. In addition communication is possible at large distances, even outside the field of view.

The conversion (or decay) of the compressed phase is further analyzed in Fig. 6.7. We plotted the area of the compressed phase versus time after stopping BDA deposition for five different domains. The substrate temperature was kept constant at 378 K. The decay curves were shifted in time for maximal overlap; the time scale is not related to the closing of the BDA source shutter. Even though, the five BDA domains have quite different shapes (see insets in Fig. 6.7) and the compressed areas have different relations to the domain boundaries, all five decay curves follow roughly the same trend. The decay curves deviate from a linear decrease: the conversion slows down for smaller remaining compressed areas. This is pointing at one of two things: either the conversion is limited by the area, or by the perimeter of the compressed phase. In the first case, we would expect an exponential decay of the area:

$$\frac{dA(t)}{dt} = -C \times A(t) \tag{6.1}$$

$$A(t) = A(t_0) \times exp(-Ct), \tag{6.2}$$

where $A(t)$ is the area of the compressed phase at time t and C is a parameter. In the case of decay limited by the length of the interface between compressed and c(8×8) area, and assuming for simplicity a circular geometry, we would expect a decay curve following a second order polynomial:
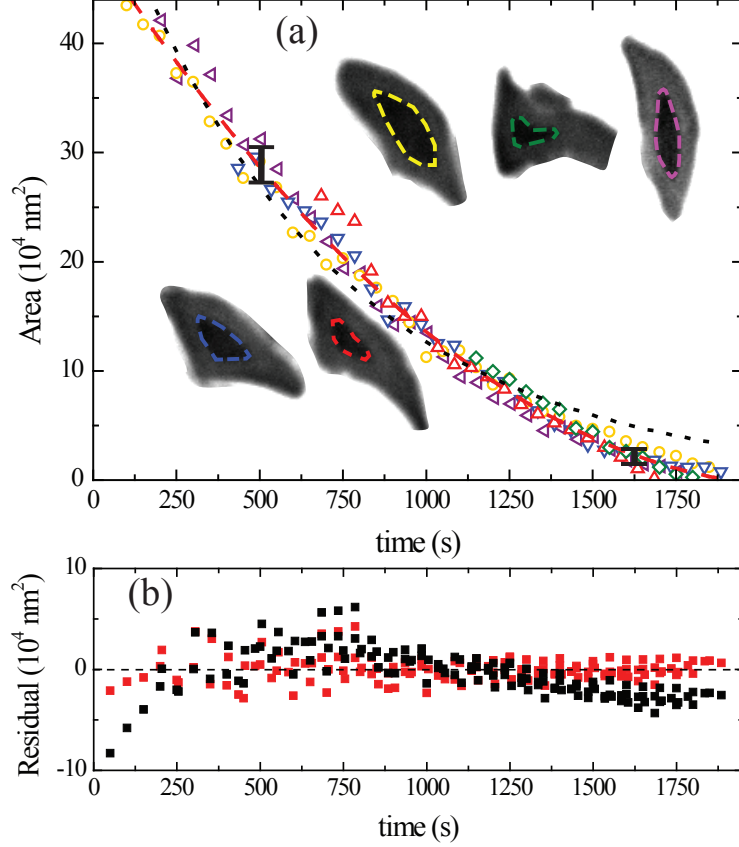
Figure 6.7: **(a)** Area of the compressed phase embedded in five different BDA islands versus time at T = 378 K and after stopping BDA deposition. The curves are shifted in time for maximum overlap. The insets show the five islands that were analyzed and the dashed lines therein mark the respective area of the compressed phase. Colors correspond to the colors of the data points. The different decay curves are identical within the uncertainty of the size determination. An estimate for the error bar is shown for two times. The black short dashed line is an exponential fit (Eq. 6.2), the red dashed line a polynomial fit of second order (Eq. 6.4). **(b)** Plot of the residuals for the two fit curves (black data points exponential fit, red (gray) data points polynomial fit).

$$\frac{dA(t)}{dt} = -C^*\sqrt{A(t)} \tag{6.3}$$

$$A(t) = (A(t_0) - 2\sqrt{(A(t_0))}C^*t + (C^*t)^2), \tag{6.4}$$

where C^* is a parameter with dimension $\frac{m}{s}$. We fitted the decay curves with both models in Fig. 6.7. The red short dashed line is an exponential fit using Eq. 6.2, the black long dashed line a polynomial fit using Eq. 6.4. The polynomial model gives the slightly better fit. The adjusted R^2 of the polynomial fit is 0.989, versus 0.958 for the exponential fit, additionally, the plot of the residuals for the exponential fit shows a systematic deviation

(see Fig. 6.7(b)). Therefore, we conclude that the decay is limited by the perimeter length of the compressed areas.

The concave shape of the decay curves in Fig. 6.7 is actually quite unusual. The decay of 2D clusters typically involves convex shaped decay curves, i.e., accelerated decay for smaller cluster sizes, or no curvature at all [59, 56, 64, 58, 57, 54]. The first case is observed when the decay process is limited by the diffusion of entities away from the edge of the island (diffusion limited decay). Also the decay of BDA c(8×8) islands follows this behavior (cf. Chapter 3). A linear decay curve is expected for decay that is limited by the detachment rate of entities from the island edge (interface limited decay). In both cases, the driving force behind the decay is a reduction of the free energy associated with the interface. The decay dynamics arise from the increasing free energy cost for smaller clusters, i.e., the Gibbs-Thomson effect. Here, this is apparently not the case; the decay rate is proportional to the perimeter length irrespective of its curvature.
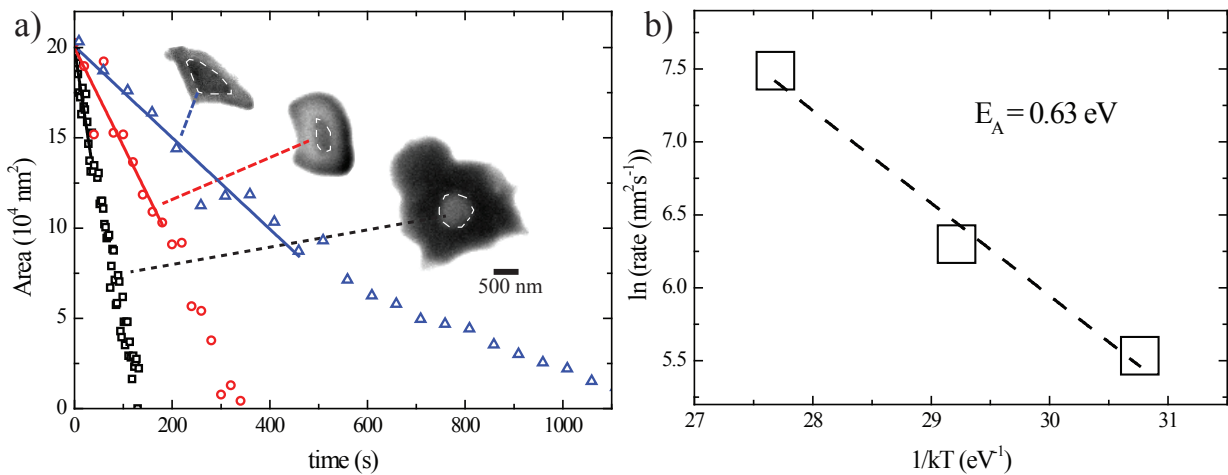
Figure 6.8: **(a)** Decay curves of the compressed phase at three different substrate temperatures. LEEM images of the respective BDA domains are shown as insets at the same scale and with the compressed phase indicated with white dashed lines. The image at 420 K was recorded with a start voltage of 2.4 V, hence the reversed contrast. **(b)** Arrhenius plot of the initial slope at $A(t_0) = 2 \times 10^5\,\mathrm{nm}^2$ in area per second of the three curves in (a) (solid lines). From the slope, we find an activation energy for the decay limiting process of $E_A = 0.63\,\mathrm{eV}$.

The decay rate of the compressed areas depends strongly on the substrate temperature: the higher the temperature, the faster the decay process. Figure 6.8(a) shows decay curves obtained for three different substrate temperatures: 378 K, 398 K and 420 K. The respective BDA islands at the different temperatures are shown as insets in the same figure. An Arrhenius plot of the three initial decay rates at $A(t_0) = 2 \times 10^5\,\mathrm{nm}^2$ is presented in Fig. 6.8(b). The three data points lie nicely on a straight line. From the slope we find an activation energy of $E_A = 0.63\,\mathrm{eV}$ for the process that is limiting the de-

cay. From the interception of the fit with the ordinate, we can determine a prefactor of $5 \times 10^{10} \, \mathrm{nm^2 s^{-1}}$. To determine the frequency prefactor ν_0 of the decay limiting process, we need to take into account our choice of $A(t_0)$. The latter comes into play through the number of molecules along the perimeter of the compressed areas. For $A(t_0) = 2 \times 10^5 \, \mathrm{nm^2}$, this corresponds to $\sim$ 1600 molecules. Therefore, we find a frequency prefactor of $\nu_0 = 3 \times 10^7 \, \mathrm{s^{-1}}$.

Despite the good fit in Fig. 6.8(b), the error bar attached to the activation energy is probably quite large, though, difficult to estimate here. The three islands in Fig. 6.8(a) have different geometries and relations to the compressed areas. Preparing an experiment with exactly the same, or even only similar, geometry is almost impossible due to the fact that the overall shape is determined by the shape of the hosting Cu(001) terraces. Given the fact that in this particular case the most compact form is found for the high temperature data a slightly lower activation energy might be more realistic.

6.3.5 Formation of vacancy holes in the c(8×8) layers
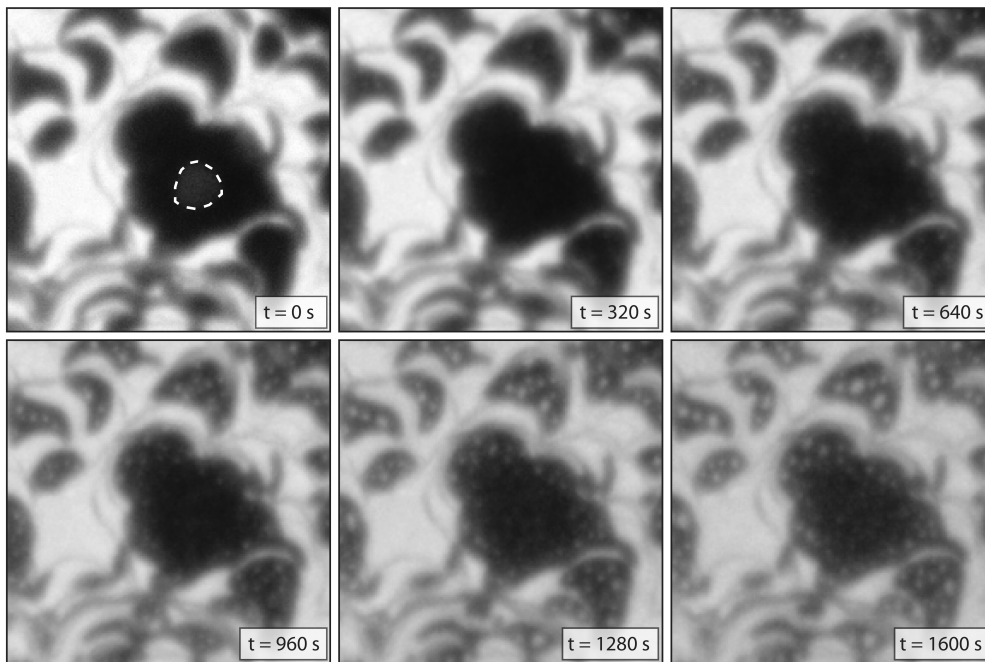
Figure 6.9: Formation of vacancy-holes in the c(8×8) domains at T = 420 K. The BDA deposition was stopped at t = 0 s. The compressed area in the first image (t = 0 s, light gray area marked with dashed line) decays within $\sim$ 250 s. Slowly vacancy-holes form in the formerly closed domains, starting close to the domain edges (t = 320 - 640 s), then also in the center (t = 960 - 1280 s). In the end, holes coalescence and form large voids (t = 1600 s). FoV is 5.5 μm, start voltage 2.4 V.

Once the compressed areas completely disappear, we observe the nucleation of vacancy-holes in the previously closed c(8×8) domains. The LEEM

image sequence in Fig. 6.9 illustrates this process at a substrate temperature of 420 K. In the first image, right after stopping BDA deposition, the c(8×8) domains appear as closed layers. The compressed phase formed in the center of the largest domain, which decayed rather fast within ∼ 250 s after closing the shutter. Immediately after the compressed phase in the center island disappeared, holes started to nucleate in the island. These holes first form close to the domain boundaries. Over time more and more holes formed increasingly in the center of the largest domains. The holes are mobile and show large edge fluctuations; molecules must be constantly attaching/detaching on the inside of the holes. As a result, the holes move slowly within the domains. We could observe several times the coalescence of holes into larger voids.

At this point the question about the fate of the missing material arises. The BDA domains are not increasing in size laterally, so the material from the vacancy-holes is apparently lost from the local area of the surface. One possibility is, that molecules diffuse to parts on the surface, which have a lower total BDA coverage. The angle at which the molecules arrive from the source is relatively flat, and we observed relatively large differences of the BDA coverage on a millimeter scale. The other, and more likely, possibility is desorption of admolecules from the domains into vacuum. The substrate temperature is quite high here, and it would not be too surprising if molecules desorb at the low rate we observed here.
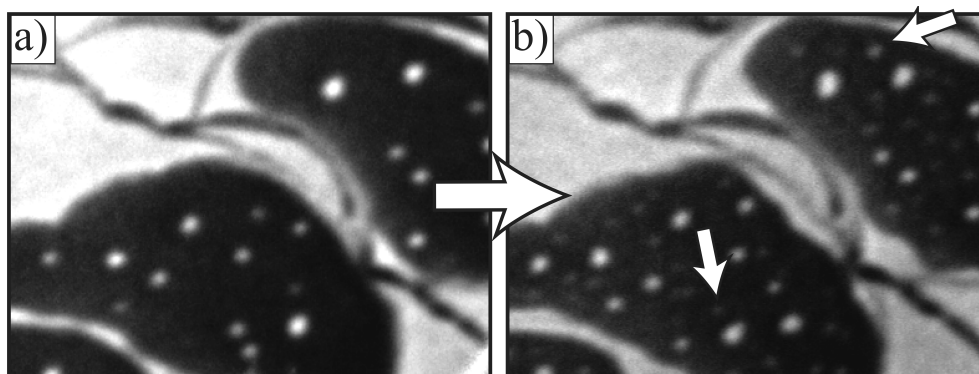
Figure 6.10: Heating of a BDA domain which from 414 K (**(a)**) to 418 K (**(b)**) within ∼ 74 s, the arrows mark two of many small holes that nucleated during the process. Images size is 1.5 μm by 1.1 μm, start voltage 2 V.

The rate at which the holes in the BDA layers form and grow depends strongly on substrate temperature. For substrate temperatures below ∼ 390 K we did not observe the formation of holes on the time scale of the experiment (∼ 1000 s). Figure 6.10 shows the result of slightly heating a domain, in which vacancy-holes already formed. We increased the temperature

in a fast step ($\sim 74\,\mathrm{s}$) from $414\,\mathrm{K}$ to $418\,\mathrm{K}$. New holes nucleate immediately in between the existing ones, as the temperature is raised. The area of the vacancy-holes increased by approximately $10^4\,\mathrm{nm}^2$ in $74\,\mathrm{s}$, while the total area of the c(8×8) domains was about $10^7\,\mathrm{nm}^2$. Therefore, the rate at which the molecules leave the c(8×8) structure and form vacancies is roughly $1.3 \times 10^{-5}\,\mathrm{s}^{-1}$. With the frequency prefactor $\nu_0 = 3 \times 10^7\,\mathrm{s}^{-1}$ we found from Fig. 6.8 (b), this gives an estimated activation barrier of $1.0\,\mathrm{eV}$.

6.3.6 Transformation mechanisms

We now address possible mechanisms behind the formation and decay of the compressed phase. To summarize our findings: the compressed phase grows in the center of islands, whose expansion is terminated by the steps bordering the host Cu(001) terrace. The shape follows the shape of the c(8×8) islands, i.e., the host Cu terrace, and the rims maintain their c(8×8) structure. The formation of the compressed phase only occurs while additional BDA is deposited from vacuum. Without this incident flux, the compressed phase is unstable and decays. The decay of the compressed phase proceeds from the division line between the compressed and the c(8×8) islands. The compressed phase does not emerge in small c(8×8) domains and is not observed at the lower end of our experimental temperature window (290 - 420 K) [38, 78, 96]. For instance, after BDA deposition far beyond a macroscopically closed c(8×8) layer at room temperature, we did not observe the emergence of the compressed structure with µLEED. The latter observations hint at the involvement of a thermally activated process. Unfortunately, we have no access to processes at the molecular scale and, therefore, we can only provide the most plausible course of events for formation and decay of the compressed areas based on the information presented before.

Formation mechanism

Our basic hypothesis is, that the formation of the compressed phase requires a local density of physisorbed admolecules on-top of the c(8×8) domains beyond a certain threshold value. The emerging admolecule density profile will have its maximum at the center of the c(8×8) domains, since admolecules will descend from the domain at its edge due to a finite Ehrlich-Schwoebel barrier. These molecules will become part of the surrounding dilute phase and finally become aggregated in the edges of still growing c(8×8) patches. The extent of the lower density near the rims will be determined by the interplay between diffusion (thus temperature and diffusion barrier) and

Ehrlich-Schwoebel barrier. In this framework, the persistent c(8×8) rims are naturally explained by the fact that there the admolecule density remains below the threshold value needed for compression. This explains, why compression does not occur in small c(8×8) patches. It also explains why the compression starts on smaller domains at lower substrate temperatures and identical BDA deposition rates: due to the lower mobility, the required threshold density can be reached even on smaller domains.

The compression process is now thought to occur by a reduction of free energy: the physisorbed admolecules on top of the c(8×8) domains can gain binding energy by making contact to the substrate, which is possible with the relatively open c(8×8) structure. A local transformation from the structure sketched in Fig. 6.5(a) to that of Fig. 6.5(c) requires a relatively mild rearrangement: molecules have to move slightly and leave their preferred adsorption geometry, and also rotate slightly to optimize the intermolecular interaction in the new situation. However, the weak hydrogen bonds in the c(8×8) structure have to be (partially) broken, which would explain why the process appears to be thermally activated. In short, the total binding to the substrate has increased at the cost of less attractive lateral interaction between molecules. We think that the compressed phase nucleates at several locations near the center, which results in about equal presence of all four rotational and mirror domains. This is consistent with the μLEED observations, where all four domains show equal spot intensity. We note that these domains cannot be resolved with LEEM and μLEED. The huge number of diffraction spots effectively makes it impossible to perform dark field measurements and the aperture used to do μLEED is just too large (1.4 μm). Since the molecular rearrangement occurs easiest at the edges of the compressed areas, the nuclei will grow and coalesce in the center of gravity of the c(8×8) domains.

Decay mechanism

After interrupting the BDA deposition, the compressed areas slowly decay back into the c(8×8) phase. This implies that this phase is not stable in the absence of the enhanced admolecule density on top of the c(8×8) domains, which is the result of the incoming flux of molecules. As during growth, the interface between both phases is sharp and the contrast difference remains constant (cf. Fig. 6.6). From this observation, and the shape of the decay curves (cf. Fig. 6.7), we conclude that the decompression also takes place at the interface between the two phases, which is consistent with a process reverse to compression: the c(8×8) structure is restored and this happens

most naturally at the interface between both phases. The excess molecules are then expelled on top of the c(8×8) domain, where they form mobile admolecules. Eventually, the admolecules will descend from the domain and be incorporated in growing c(8×8) domains nearby; or perhaps even desorb into vacuum. For the moment we disregard the latter option, which seems to occur at very low rates for the higher end of the temperature range probed here. We mention that the sketched mass transport events would satisfy micro-reversibility requirements. However, the situation may be more complicated, since we cannot exclude that the diffusing particles are different: the arriving BDA molecules will be protonated, while the expelled molecules may be (partially) deprotonated. As mentioned above, we will stick to this simple description since we have no access to detailed molecular processes. The described processes are illustrated in Fig. 6.11.
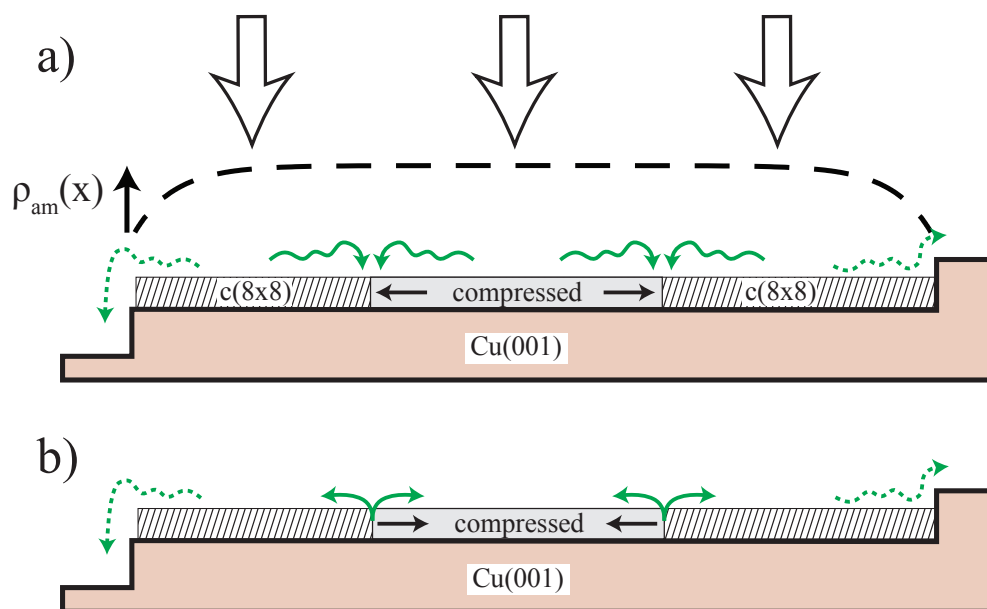
Figure 6.11: Sketch of the compressed phase formation (a) and decay (b). **(a)** During deposition of molecules on the existing layers, an admolecule phase is formed. Physisorbed admolecules have two ways to leave the layer: Diffusion down onto a Cu terrace (dashed arrow) or incorporation into the compressed phase (solid arrow). The density $\rho_{am}(x)$ of the admolecule phase will be highest in the center of the domain, where the compressed phase nucleates first. **(b)** Proposed mechanism that leads to the decay of the compressed phase after stopping the deposition: molecules are expelled at the interface between compressed and relaxed phase (solid green arrow), where they form again admolecules that can diffuse down (or desorb; not shown).

We found that the decay process is activated with $0.63\,\mathrm{eV}$ (cf. Fig. 6.8). An obvious assumption would be, that this is the energy required to push out one molecule from the layer at the boundary between the compressed and the c(8×8) phases. The value of 0.63 eV carries a substantial error

bar. From the growth rate of the integrated areas of vacancy holes at high temperature (Fig. 6.10), we have estimated an activation barrier of 1.0 eV. This is supposedly an activation energy for the movement of a molecule from the edges of a vacancy-hole to the top of the c(8×8) domain. If we account also for the cohesive energy of 0.35 eV in the c(8×8) structure (cf. Chapter 3), this would yield an activation energy of 0.65 eV for the formation of an admolecule from the c(8×8) phase. The comparison of the two activation energies (from the decompression kinetics and the vacancy-hole formation) is consistent.

6.4 Conclusions

We have demonstrated with LEEM and μLEED the formation of a compressed BDA phase on Cu(001). The compressed phase nucleates in the center of large (uncompressed) c(8×8) domains during BDA deposition at elevated temperatures ($\sim> 370$ K). The interface separating both phases is very well defined. We determined the structure in the compressed phase with μLEED and found a $\left(\begin{smallmatrix} 5 & -7 \\ 5 & 4 \end{smallmatrix}\right)$ overlayer, with four equally populated domains (two rotational domains, each split into two mirror domains). The structure is commensurate to higher order and the molecules are packed 14% denser than in the uncompressed c(8×8) structure.

The emergence of a compressed phase shows the delicate balance of the different energies in the growth of supramolecular networks on metal surfaces. The interaction of the chemisorbed molecules with the substrate is much stronger than the mutual interaction between adsorbed molecules through relatively weak hydrogen bonds. Therefore, the molecules in the networks are only very loosely bound to each other. At the relatively elevated temperatures used here, the presence of admolecules on the layers is apparently already enough to break the molecular networks and allow the incorporation of additional molecules, which reduces the total free energy.

7

In-situ observation of a deprotonation driven phase transformation - BDA on Au(111)

We have studied the growth of 4,4'-biphenyldicarboxylic-acid (BDA) domains on Au(111) by Low Energy Electron Microscopy (LEEM) and μLEED. In the temperature range of 300-400 K the linear BDA molecules form at least three different 2D crystalline phases on Au(111). We attribute the presence of different phases to the substrate assisted and thermally activated deprotonation of the acid, a surprising result given the anticipated low reactivity of the gold substrate. We determined the crystal structure of each phase with selected area diffraction (μLEED). At room temperature the BDA molecules form needle shaped domains with the carboxylic-acid dimer being the main molecular bonding motif. Upon annealing the substrate covered with BDA needles from room temperature to above ∼ 330 K we observed a remarkable and irreversible transformation of the domain shape from needle like to more compact 2D islands. The lattice position of the molecules in the annealed domains does not change, however, the molecules rotate slightly to make contact to a lateral neighbor. We attribute this rotation to a partial deprotonation of the carboxylic-acid groups and the breaking of the dimer bonds, which we further support with work function measurements (LEEM IV). Finally, a third phase, the γ-phase, is formed upon direct BDA deposition with the substrate temperature above 330 K. In this phase the molecules form an open 2D metal-organic coordination network by the incorporation of Au ad-atoms.

7.1 Introduction

Hydrogen bonded networks formed by molecules adsorbed on surfaces offer a promising way to create novel nanostructures [5, 7, 27, 109, 81]. Understanding how the molecules interact with each other is crucial to obtain control over the self-assembly. In general, these nanostructures are formed close to thermal equilibrium and thus represent a thermodynamic minimum in free energy. An advantage of this growth close to equilibrium is an intrinsic error-correction: Since the hydrogen bond strength is in general rather weak, molecules adsorbed at incorrect positions can detach again and reattach at the correct lattice position. One class of systems, that is particularly interesting, are benzoic-acids adsorbed on metal surfaces. The structure, that these molecules form, is determined by an interplay between the molecule-substrate interaction and the possible hydrogen bonds that can be formed between molecules. The latter depends on the number of carboxylic-acid functional groups, and their respective positions. For example, linear and symmetric benzoic-acids often assemble in close-packed rows forming carboxylic-dimer head to tail bonds [13, 18, 43, 110, 108, 44], while benzoic-acids with a three-fold symmetry form honeycomb networks [16, 10, 20].

More structures are obtained if the benzoic-acids deprotonate on the reactive metal surfaces or through the incorporation of small metal atoms, either deliberately co-deposited or originating from the metal substrate itself. In this case, the formation of very well ordered structures with regularly spaced voids was observed [111, 12, 38, 21, 112]. The deprotonation reaction is a thermally activated process catalyzed by the metal substrate. Therefore, the activation energy for this reaction depends strongly on the type of metal substrate. For example, on the relatively reactive Cu surfaces, deprotonation of the carboxylic-acid groups was observed below room temperature [107, 113, 10, 106, 11, 14, 114]. On the other hand, on Ag(111) deprotonation was observed at higher temperatures [16]. The different carboxylic-acid groups on the molecules deprotonated stepwise at different temperatures. On the less reactive Au(111) surface, no deprotonation of benzoic-acids was observed so far under vacuum conditions [13, 43, 19, 108, 112]. An exception is, if more reactive metal ad-atoms are co-deposited on the surface [115, 25, 112]. These observations are all based on the molecular interaction derived from the arrangement of the molecules, i.e. their distances and orientation, as observed in STM.

Understanding and controlling the deprotonation state is not only important in terms of the structures' stability. By changing the deprotonation state

of the benzoic-acids it is possible to gain further control over the structures that are formed by the molecules and their interaction with other adsorbates.

Here, we present a low-energy electron microscopy (LEEM) and selected area diffraction (µLEED) study on the growth of 4,4'-biphenyldicarboxylic-acid (BDA) on Au(111). BDA consists of two phenyl rings and two functional carboxylic-acid groups (see sketch in Fig. 7.2). The molecule is linear with a length of about 1.15 nm, as measured between the oxygen atoms of the two carboxylic-acid groups. The carboxylic-acid groups are actively involved in the mutual interaction between BDA molecules. Depending on whether these groups are in a protonated or deprotonated state, different types of bonds can be formed. On Cu(001) and at room temperature, BDA is deprotonated and two molecules form bonds between the carboxylate groups and the phenyl ring of the next molecule (cf. Chapters 3-6). A direct interaction between the carboxylate groups is not possible. STM studies on the adsorption of BDA [43, 19, 108] and of the similar terephthalic-acid (TPA) on Au(111) [13] reported close-packed structures, with molecular chains located side by side. This structure is typical for the carboxylic-acid head to tail bonding as the main intermolecular interaction motif and the same interaction is also observed in bulk crystal modifications of TPA [116]. The presence of this type of bond suggests that BDA molecules are protonated on the Au(111) surface, at least under the conditions employed in the STM studies.

Our findings here generally confirm this picture for BDA deposited with the Au(111) substrate close to room temperature. In addition to the close packed structure, Xiao et al. [19] also observed chiral, rectangular BDA networks. As the authors reported, annealing to 393 K did not change the relative coverages of both domain types (close-packed and chiral), an observation which makes a deprotonation driven reaction or the incorporation of Au ad-atoms unlikely. However, in this chapter we show that the BDA molecules indeed deprotonate at higher substrate temperatures, and that at least three different crystalline phases are formed on the Au(111) substrate. Each phase is formed under different growth conditions. This observation is in contrast to previous studies, but is clearly demonstrated and comprehensively explained by the enhanced real time imaging capabilities of LEEM.

7.2 Experimental

Experiments were performed in an Elmitec LEEM III with a base pressure of 1×10^{-10} mbar. A Au(111) crystal was prepared by cycles of Argon ion sputtering and annealing at 500-600°C. BDA in powder form (Purity > 97%, TCI

Europe, CAS: 787-70-2) was evaporated from a Knudsen cell type evaporator. Prior to experiments, the evaporator was thoroughly degassed. Molecules were evaporated at a source temperature of 463 K with the sample held at fixed temperatures for each deposition experiment between 300 K and 380 K. The source temperature of 463 K resulted for Cu(001) in a BDA deposition rate of $8 \times 10^{-6}\,\text{ML s}^{-1}$, where we express the coverage in terms of occupied Au(111) lattice sites. One BDA molecule covers approximately 12 Au(111) lattice sites; the maximum BDA coverage in a close-packed structure is thus 1/12 ML.

LEEM images were recorded in bright-field mode at a start voltage between 2-3 V. The exposed area was limited by an illumination aperture with a diameter of 25 μm. Any electron beam induced damage is then observable as a sharp change in island density and/or morphology at the edge of the exposed area. Indeed we observed very slow electron induced degradation at start voltages above 3 V, however, not to an extent that interfered with measurements, as long as the exposed area was occasionally changed.

The images shown here are all corrected for an inhomogeneous background intensity. LEEM images were normalized to an image of the clean surface taken in mirror mode, which removes most of the inhomogeneities of the channel plate detectors. The μLEED patterns were corrected for a cloud of secondary electrons, which yields only little information on the surface structure (see Chapter 2).

7.3 Results and Discussion

7.3.1 BDA growth at room temperature

In a first experiment, we deposited BDA with the Au(111) crystal at room temperature. Figure 7.1(a) shows a LEEM image of the Au(111) surface after deposition of approximately 0.013 ML of BDA. The molecules condensed into elongated needle shaped domains. Each domain nucleated at an Au step. Most of them (but not all) at a defect, which is pinning the Au step (cf. white arrows in Fig. 7.1(a)). The growth of the needles is much faster in their long direction than in the short direction. The growth rates in the two directions differ by a factor of 10 to 20. The exact difference is not constant and depends on the local environment of the growing needle, e.g., on the competition for material with other needles. At substrate steps, the needles get blocked in their growth, but occasionally cross over single steps and continue to grow on the neighboring terrace with the same orientation. The needles grow preferably in certain directions, generally not coinciding with
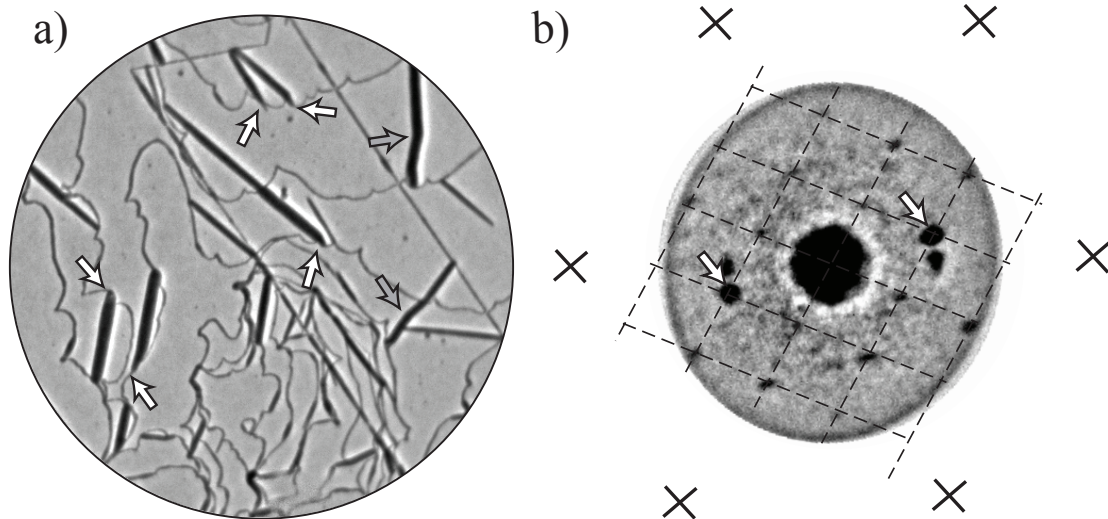
Figure 7.1: **(a)** LEEM image of BDA grown at room temperature on Au(111) with a BDA coverage of about 0.013 ML. White arrows mark where some of the black BDA needles nucleated. Gray arrows mark two examples, where the respective needle changed growth direction (Field of view (FoV) is 5.5 µm, start voltage 3 V. **(b)** slightly distorted µLEED pattern at 8 eV from a single BDA needle in (a). Crosses mark the position of the Au(111) first order spots, which are outside the Ewald's sphere. Weak diffraction spots can be described with a c($\begin{smallmatrix} 8 & 2 \\ 0 & 3 \end{smallmatrix}$) superstructure (dashed grid). Arrows mark the pair of bright diffraction spots, indicative for the molecular orientation within the unit cell. A second domain shows up as additional, much weaker, spots.

the substrate high symmetry directions. Exceptions to this are intersections of bulk glide planes with the surface. The glide planes are caused by plastic deformation during annealing of the crystal and show up as straight lines along substrate symmetry directions. BDA domains nucleate at these lines and grow parallel to them, resulting in a decoration with needles. This behavior is different from the one observed for domains that nucleate at regular substrate steps, which generally grow away from the step onto the terrace. Most of the individual domains grow in only one direction, resulting in straight needles. However, occasionally the domains change their growth direction on a terrace by a small angle ($< 20°$). A few examples for this are indicated with gray arrows in Fig. 7.1(a)).

To determine the crystal structure in the needles we used µLEED. We selected an area of surface with a 1.4 µm illumination aperture, which minimized the number of different needle domains exposed to the electron beam. Due to the high density of needles, especially small needles at steps, it was impossible to isolate an individual needle in the aperture. A representative diffraction pattern at 8 eV obtained from mostly a single domain is shown in Fig. 7.1(b). The most prominent feature in the pattern is a pair of intense diffraction spots. These lie in a direction that is perpendicular to the long

axis of the BDA needle. In Fig. 7.1(b), we captured two needles within the aperture. The set of spots which are marked with arrows in Fig. 7.1(b)), originate from the largest needle in the aperture. A second, much weaker set of spots belong to a smaller needle in the aperture, with a slightly rotated orientation. By scanning across the surface in µLEED, we could find at least 12 different rotational domains. This is twice as many as expected for a threefold symmetric substrate, which is indicative for a weak interaction between the molecules and the substrate. Therefore, there are only small energy differences for growth along different azimuth directions. The latter is also supported by calculations of the BDA potential energy on Au(111) as a function of binding angle [117].

The two dominant bright spots appear at a distance, which corresponds to 2.5 Au nearest neighbor distances (0.72 nm) in real space. This value nicely corresponds to the van der Waals width of BDA. The result suggests a structure consisting of chains of BDA molecules, which are separated by their van der Waals width. This can be understood by realizing that all molecules constituting an individual chain scatter the probing electrons coherently, when considering a direction perpendicular to the chains. When adjacent rows scatter in phase, very strong diffraction spots perpendicular to the rows are to be expected. Our results are completely consistent with, and thus reconfirm, the structure found in STM studies for BDA on Au(111) [43, 19, 108]: elongated domains, or needles, consisting of parallel chains of molecules. The chains aggregate side by side, and are stabilized by van der Waals forces.

A set of much weaker diffraction spots can be described with a $c\left(\begin{smallmatrix} 8 & 2 \\ 0 & 3 \end{smallmatrix}\right)$ superstructure in matrix notation, where we use the $[10\bar{1}]$ and $[\bar{1}10]$ substrate directions as a base (cf. Fig. 7.2). Attempts to obtain a higher quality diffraction pattern failed, mainly due to the small individual needle sizes and the electron beam induced degradation at energies above 3 eV that prevented long exposure times.

A model of the proposed structure is shown in Fig. 7.2. The molecules arrange in a close packed structure, as already observed in STM in other studies [43, 19, 108]. In the grammar of molecular epitaxy [97], this superstructure corresponds to a coincidence-IA "point-on-line" (POL) overlayer. The molecules interact mutually through the formation of relatively strong carboxylic-dimer bonds within the individual chains. The chains aggregate side by side due to weak van der Waals forces. The intermolecular distances are consistent with the close packed structures reported in previous STM studies [43, 19, 108]. The shortest distance between two molecules within one chain is 1.42 nm and for two molecules in adjacent chains 0.86 nm. The
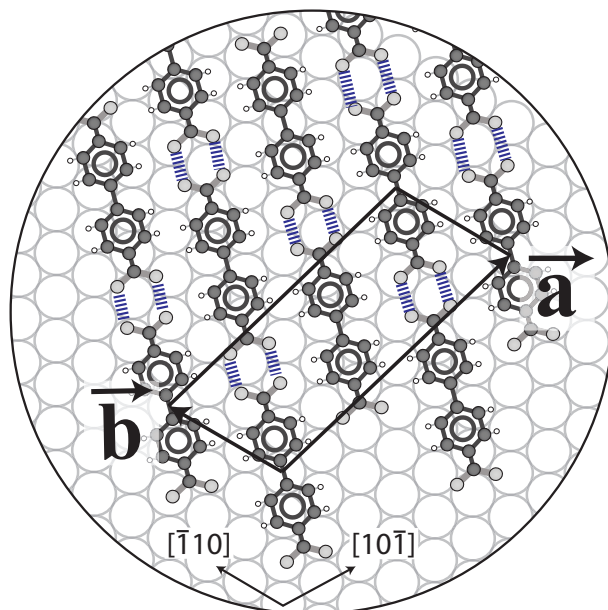
Figure 7.2: Model of the proposed structure in the α-phase: Molecules interact through head to tail bonds indicated with blue dashed lines.

distance of the oxygen atoms in the dimer hydrogen bond is 0.27 nm, close to the value of 0.275 nm found in bulk TPA crystals [116].

The weak intensities of the diffraction pattern (with the exception of the aforementioned pair of bright spots) are indicative for a poorly defined super-structure. One reason for this poor ordering is the lack of strong molecular in-teraction between the chains: While the distance between neighboring chains is well-defined through the size of the molecules, the correlation between the positions of molecules in adjacent chains will be small. Another reason is the apparently weak interaction of the BDA with the substrate: molecules are not adsorbed at well-defined lattice sites, but feel only a weakly corrugated potential landscape [117].

The weak interaction of BDA with Au(111) is not surprising. Calcu-lations of the benzene adsorption energy on Au(111) gave an estimate of only 0.077 eV, compared to 0.68 eV on Cu(001) [118]. On the other hand, the carboxylic-dimer is a relatively strong bond. Calculations estimated its strength to be 0.5 to 0.6 eV [119, 20]. The energy gained by optimizing the hydrogen bond length is thus much larger than the energy gained by optimizing the adsorption geometry. The minor influence of the substrate is also reflected by the existence of at least 12 rotational domains. Some of these domains will follow lower symmetry substrate directions than the $c\left(\begin{smallmatrix} 8 & 2 \\ 0 & 3 \end{smallmatrix}\right)$ superstructure or are even incommensurate. Still, the energy cost for growth in these directions, related to non-optimal registry with respect to the substrate, is apparently small and kinetic effects during BDA growth

outweigh them. Additionally, the Au(111) herringbone reconstruction introduces a periodically varying substrate [120, 121]. In the µLEED patterns we did not observe a splitting of the spots, suggesting that the molecules do not follow the reconstruction. This is different from the case of TPA adsorbed on Au(111) [13]. Probably, the smaller TPA molecule, which consists out of only one phenyl ring, can conform better to the substrate potential energy landscape, gaining relatively more energy by optimizing the adsorption geometry. For the larger BDA it is more difficult to find such configurations on a substrate with varying lattice constant.

7.3.2 Transformation of the α- into the β-phase

Up to now, we only discussed BDA growth at a substrate temperature close to room temperature. We will denote the closed-packed structure that the BDA molecules form at this growth temperature as the α-phase. In this section, we will show that the α-phase is not stable against a slight increase of the temperature - it converts irreversibly into a new phase, the β-phase, upon annealing. The transformation is faster for higher substrate temperatures, i.e., the conversion is thermally activated.

Figure 7.3 shows two LEEM image sequences of the transformation process. The two experiments differ in the initial BDA coverage, annealing time and annealing temperature. In both experiments, the surface is first covered with α-phase needles grown at room temperature. The needles are mostly located along step edges and decorate glide lines, which run across the image. As the substrate temperature is increased, we can see how the islands change their shape and the needles become more compact. Some of the needles shrink and decay, mainly those which were initially smallest (especially width) and those decorating dislocation lines. At the same time, the other needles grow considerably in size. The longer annealing at a higher temperature (390 K) in the experiment shown in Fig. 7.3(b) results in further ripening of the compact domains. At the end of this experiment, the surface is covered by only a few domains, each spanning over several neighboring Au terraces and reaching sizes of several square micrometers. The whole process only involves the transformation of existing α-phase needles, the nucleation of new domains is not observed (cf. Fig. 7.4).

Already in the first image of Fig. 7.3(b), some of the α-phase needles are slightly rounded - they are considerably deviating from the shape seen in Fig. 7.1. Taking into account the observation of a thermally activated transformation, it is reasonable that the needles are already slowly transforming at lower temperatures. As we will discuss in Sect. 7.3.5, the phase transforma-

Figure 7.3: Two examples for the transformation of the α-phase needles into the β-phase, which is characterized by increasingly compact island shapes. Annealing times are defined as the time lapse from the start of the temperature increase. The curved lines represent step(bunche)s and the straight lines show the intersection of glide planes with the (111)-surface and are thus oriented along close packed azimuth directions. The experiment in the top row **(a)** started at a lower initial BDA coverage, and features a shorter anneal at a lower final temperature as compared to the experiment in the bottom row **(b)**. The longer annealing at a higher temperature results in ripening of the β-phase domains and therefore a lower island density. The dashed box in the first image indicates the area presented in detail in Fig. 7.4. Top row: FoV 10 μm, start voltage 3 V, bottom row: FoV 6 μm, start voltage 2.7 V.

tion is driven by the (thermally activated) deprotonation of the carboxylic-acid groups. The α-phase is thus a low temperature phase, formed by the protonated species and only stable at low temperatures due to the frozen deprotonation kinetics.

In Fig. 7.3(b) we can see that some domains (marked with white arrows) first grew, and then decayed later in the annealing process, while at the same time larger domains grew further. Apparently, the large domains grew through Ostwald ripening, due to different vapor pressures of the individual domains. That difference is partially caused by the different domain sizes (Gibbs-Thomson relation), but could additionally be caused by the
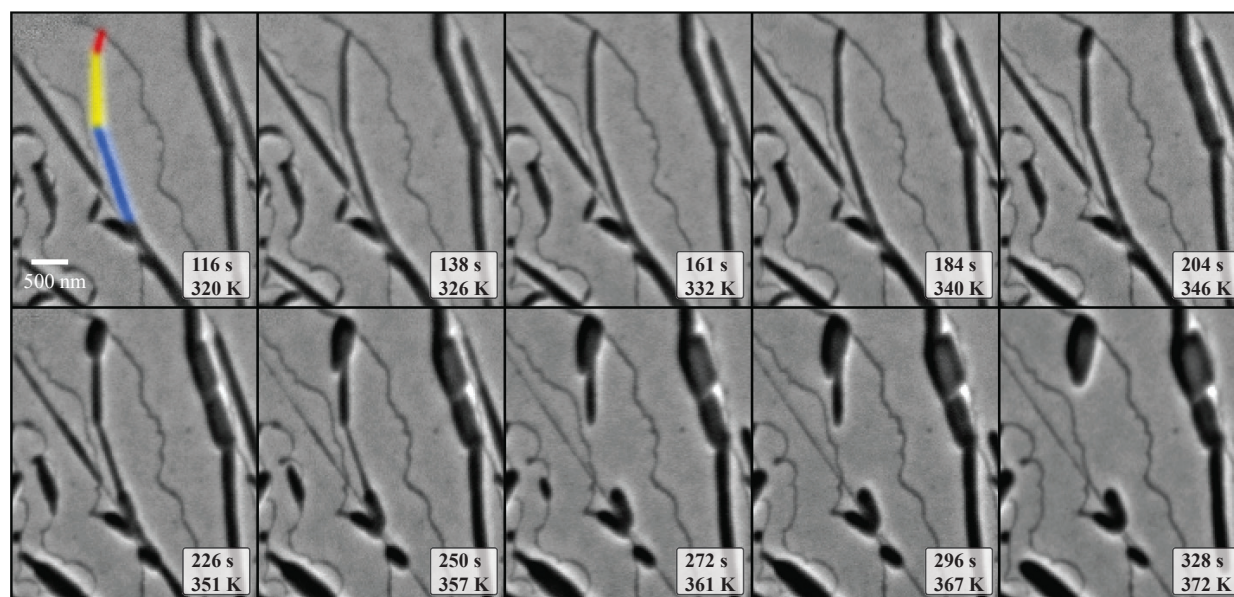
95

Figure 7.4: Detail of the transformation process shown in Fig. 7.3(a). The needle in the center consists initially out of three domains (recolored for clarity in the first image), which grew in different directions. Upon increasing the temperature the uppermost domain is transforming and growing at the expense of the other two domains. Nucleation of new domains is not observed.

specific registry of the molecular structure in each domain with respect to the Au(111) substrate.

7.3.3 Crystal structure in the β-phase

The transformation process in Fig. 7.3 not only involves an impressive change of the island shape, but also of the crystalline structure. Figure 7.5(a) shows a µLEED pattern obtained from a single domain of the β-phase at an electron energy of 30 eV. The other domains show identical patterns, except for different orientations with respect to the substrate lattice. The six intense spots on the outside in Fig. 7.5(a) are the first order Au(111) diffraction spots. Each spot is six-fold split due to the Au(111)-($22 \times \sqrt{3}$) herringbone surface reconstruction (cf. inset in Fig. 7.5(a)) [120, 121].

The β-phase diffraction pattern is closely related to the pattern observed for the α-phase. However, the main difference is an overall increased quality of the pattern, i.e., higher order spots are significantly more intense. The ordering of the molecules is increased, which is apparently caused by a stronger interaction of the molecules with the substrate in the annealed β-phase. This is also consistent with the existence of only 6 rotational domains, which is the expected number of domains. Three domains are formed due to the symmetry of the substrate and each is split into two mirror domains. The pair
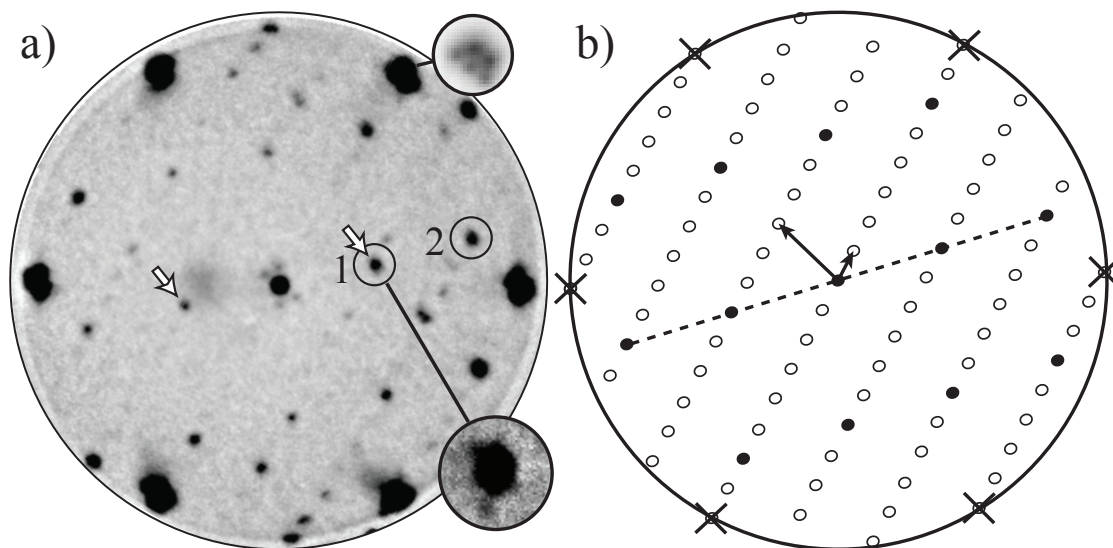
Figure 7.5: **(a)** Background corrected (see Chapter 2) µLEED pattern of the β-phase measured at an electron energy of 30 eV. The brightest spots belong to the Au(111) substrate. Each spot is split due to the herringbone reconstruction. The insets show the splitting of one of the Au spots as well as a faint splitting of the brightest spot belonging to the β-phase. **(b)** Calculated pattern of the $\left(\begin{smallmatrix} 8 & 2 \\ 0 & 3 \end{smallmatrix}\right)$ superstructure, which describes the observed diffraction pattern. Black circles mark selected spots that carry more intensity.

of bright spots, which was the main feature in the α-phase µLEED pattern, is also still present in the β-phase at an identical position. Additionally, the corresponding second order spots are also clearly visible and are more intense (spots labeled 1 and 2 in Fig. 7.5(a)). It is thus reasonable to conclude, that in the β-phase the same side-by-side aggregation of molecules as in the α-phase is present.

The diffraction pattern (Fig. 7.5(a)) can be described with a $\left(\begin{smallmatrix} 8 & 2 \\ 0 & 3 \end{smallmatrix}\right)$ superstructure, which we express in the same base as introduced before (see Fig. 7.6). The unit cell is identical to the one in the α-phase, with the difference that the superstructure is *not* centered anymore. An important observation is, that the transformation proceeded through the conversion of the α-phase domains, and not through the nucleation of new domains (see Fig. 7.4). Therefore, there are restrictions to the orientation of the molecules and their density in the β-phase due to steric hindrance. A major change of the density would require the concerted motion of thousands of molecules, which seems unlikely.

The presence of the two intense spots shows, that the molecules are still oriented in a similar way as in the α-phase. Apparently, the main difference is that in the α-phase the two molecules in the unit cell are identical scatterers, which results in the extinction of spots. This degeneracy is lifted in the β-phase, which can either be caused by different adsorption heights or different
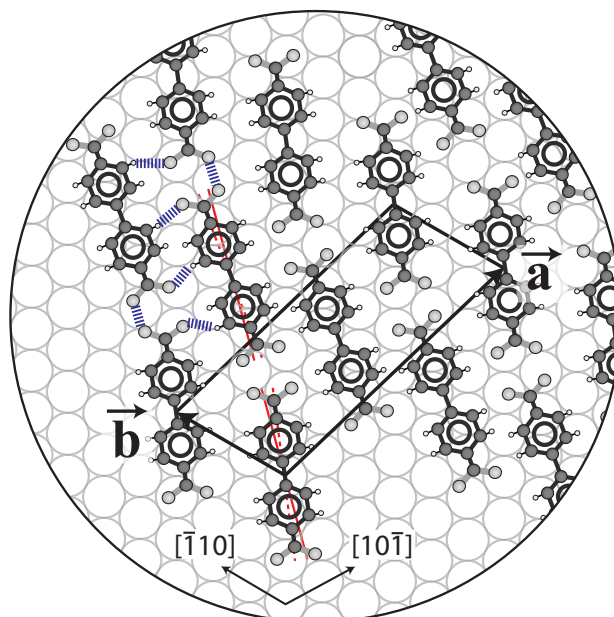
Figure 7.6: Model of the proposed structure in the β-phase: Intermolecular distances are identical to the α-phase, but the corner and center molecules in the unit cell are slightly rotated in opposite directions. Dashed blue lines mark proposed hydrogen bonds between molecules (see Sect.7.3.5).

orientations of the center and corner molecules. Indeed, the center molecule is positioned at a different lattice site, however, this is also the case in the α-phase. Another possibility is, that the two molecules are slightly rotated against each other by only a few degrees (see sketch in Fig. 7.6). In this way, the average orientation of the molecules is still perpendicular to the direction defined by the intense spots (the $[3\,8\,\overline{11}]$ substrate direction), while the molecules are not equivalent scatterers, giving rise to the not centered superstructure. Except for the small rotation, this structure is identical to the α-phase and no mass transport is necessary for the phase transformation. We will discuss the origin for a rotation in Sect. 7.3.5.

The molecules in the β-phase form a commensurate superstructure. A faint splitting of the brightest spots suggests that the molecules follow the herringbone reconstruction of the underlying Au lattice (see inset in Fig. 7.5(a)). In total we observed six rotational domains with an otherwise identical LEED pattern. Presumably, the β-phase domains are formed by α-phase domains, which were oriented closest to these directions.

7.3.4 BDA growth above ~ 330 K (γ-phase)

Finally, a third phase is formed by the direct deposition of BDA at higher substrate temperatures (from about ~ 330 K), which we will denote as the
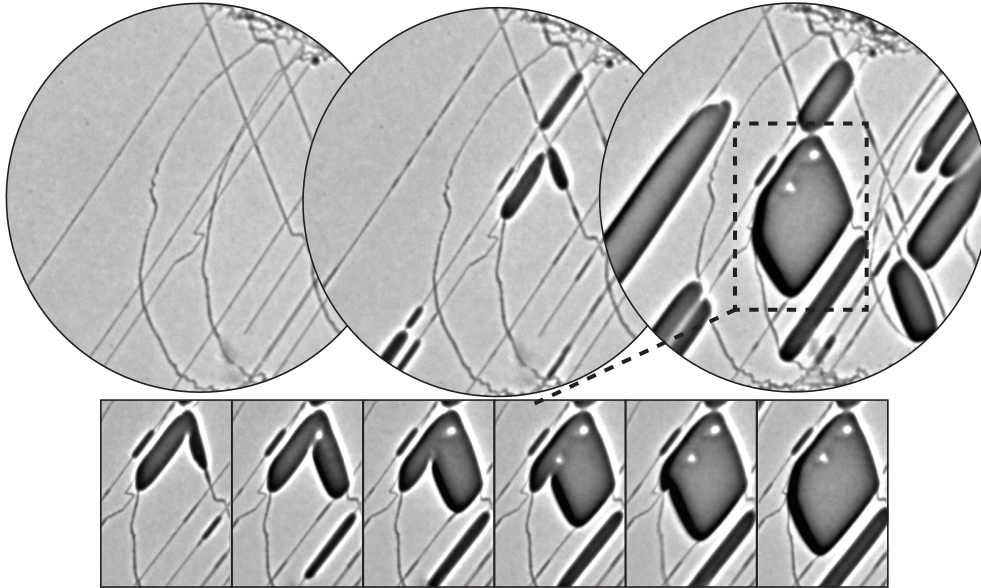
Figure 7.7: Image sequence of BDA growth at $T_S = 380\,K$. Domains nucleate at glide lines and grow with a higher rate along the same lines. Domains do not grow over step edges or glide lines. BDA coverage in the final image is about 0.025 ML. The inset shows the growth of one domain in detail, time lapse between frames is 120 s. FoV is 4 µm, start voltage 2.7 V.

γ-phase. Figure 7.7 shows an image sequence of the BDA growth at a substrate temperature of 380 K. Domains nucleate at substrate glide lines (cf. Sect. 7.3.1) and first grow along them. The domain growth rate parallel to the glide line is slightly higher than the growth rate away from the glide line, onto the terrace. In none of the cases did we observe the crossing of a domain over a glide line or a substrate step onto a neighboring terrace, which is different from the behavior of the α-phase and β-phase domains. The domains grow with remarkably straight boundaries. Especially the boundary that is parallel to the glide line (and not blocked) shows surprisingly straight edges. These sides of the domains expand with a growth rate that is constant over the entire length (see inset in Fig. 7.7). This is very different from the ramified structures observed for the β-phase (see Fig 7.3(b)).

Figure 7.8(b) shows a cumulative µLEED pattern obtained from an individual γ domain by summation of patterns for electron energies from 3 eV to 35 eV at 1 eV spacing. Again we find back a pair of two intense spots, which we have already seen for both the α and β-phase diffraction patterns. The spots appear at the same periodicity, however, lie now along a high symmetry substrate direction (here [$\bar{1}$10]). For each domain this direction coincides with the crystal direction of the glide line at which that domain nucleated. From this information, we conclude that again side-by-side aggregated chains of molecules are present in the γ-phase, similar to the α- and β-phase. The chains are oriented parallel to the glide line, i.e., in Fig. 7.8 along the [$\bar{1}$10]
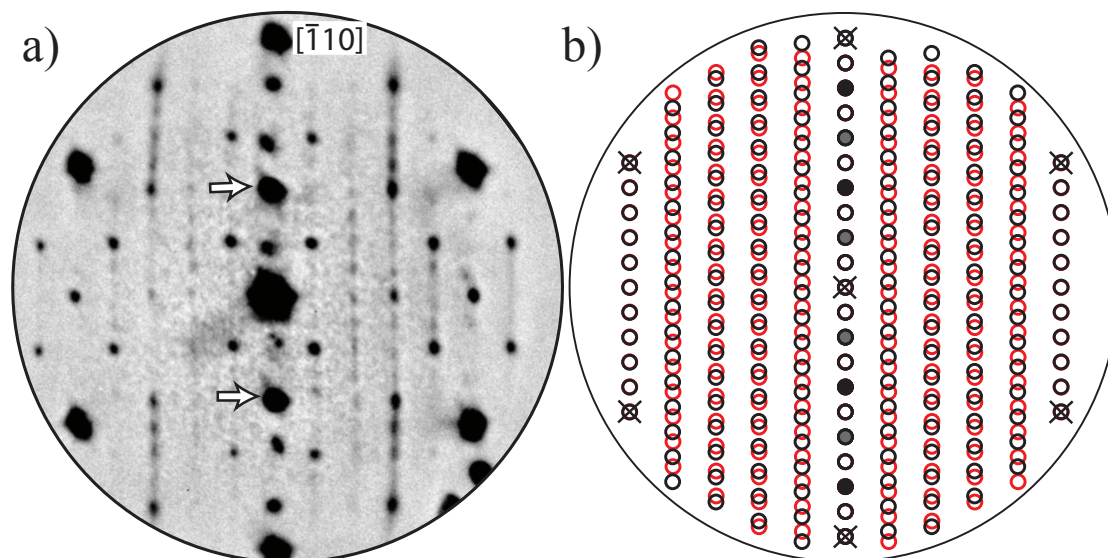
Figure 7.8: **(a)** Cumulative µLEED pattern from $3\,\text{eV}$ to $35\,\text{eV}$ obtained from an individual γ-phase domain. Most prominent features are a pair of intense spots (arrows) and rows of several spots along the $[\bar{1}10]$ direction. **(b)** Explanation of the µLEED pattern: A superposition of two mirror domains (black and red circles) with a $\left(\begin{smallmatrix} 10 & 4 \\ 0 & 5 \end{smallmatrix}\right)$ superstructure. The mirror axis is the $[\bar{1}10]$ direction. Filled spots along that direction carry a high intensity.

direction. Parallel to this direction we observe rows of several spots, which appear severely smeared out. On the other hand, the distance between the rows is very well-defined at a five-fold periodicity. The weak definition of the spots in the rows could point at disorder in this direction. However, along the $[\bar{1}10]$ direction the spots are well-defined. The explanation is, that the pattern is a superposition of two mirror domains with a $\left(\begin{smallmatrix} 10 & 4 \\ 0 & 5 \end{smallmatrix}\right)$ super-structure and the $[\bar{1}10]$ direction as a mirror axis. The diffraction spots of both domains overlap only for every 5th row, while in between they are at interdigitated positions, which makes them appear undefined. A calculation of the resulting diffraction pattern is shown in Fig. 7.8(b).

A model of the molecular structure for one of the two mirror domains is shown in Fig. 7.9. This structure is equivalent to one of the chiral structures ("B"-phase) found by Xiao et al. [19]. The double row of molecules along $[\bar{1}10]$ causes the intense spots pair. The µLEED pattern in Fig. 7.8 was obtained from what appeared to be one continuous domain, however, still both mirror domains are present in the diffraction pattern with equal intensities. This was also the case for all other domains, which produced equivalent LEED patterns. The mirror operation involves only a phase shift of the molecules within the double row. Perpendicular to the $[\bar{1}10]$ direction both mirror domains are compatible to each other and a shift from one mirror domain to the other should be easily incorporated. Both mirror domains can therefore exist in a single continuous domain.
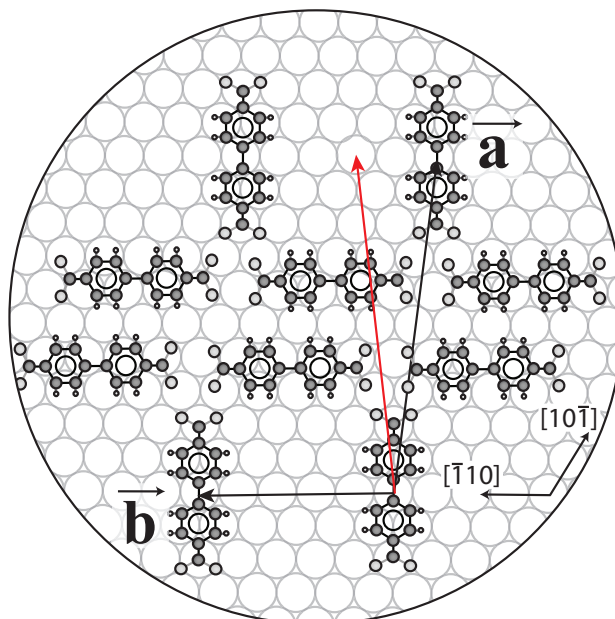
Figure 7.9: Proposed molecular structure in one of the mirror domains of the γ-phase, which is equivalent to the structure found by Xiao et al. [19]. The unit cell of the other mirror domain is indicated with a red arrow.

7.3.5 A deprotonation driven phase transformation?

In the α-phase the molecules are fully protonated. This is consistent with the observed growth anisotropy and the resulting needle like domain shape, which is typical for the formation of strong carboxylic-dimer bonds. On the contrary, in the β- and γ-phases the molecules form extended 2D sheets with sizes spanning several µm². This is an indication for a more uniform bonding in the different crystalline directions. The proposed structure in the β-phase is very similar to the α-phase and at first sight one would also expect the formation of carboxylic-dimer bonds. However, this interaction scheme would be incompatible with the clear two dimensional character of the domains, which suggests a more uniform interaction; or at least a stronger lateral component perpendicular to the chains. A possibility is the formation of inter-row hydrogen bonds, which are however expected to be much weaker [122]. From this point of view, there is no reason why the molecules should break a stable bond and form a less stable bond at higher temperatures. A likely explanation is, that the carboxylic-acid groups deprotonate upon annealing. In that case, it is impossible for the molecules to form dimer bonds; instead the negative charge left on the carboxylate group will result in the formation of a bond to the hydrogen atom on the phenyl ring of a lateral neighbor. A similar transition was observed for the (self-limiting) deprotonation of TPA on Pd(111) [18]. There, the protonated phase formed

one molecule wide chains, while the deprotonated molecules aggregated in 2D domains. The bonding in the β-phase would be similar to the deprotonated phase of TPA on Pd(111), however, with every second molecule slightly rotated.

The rotation of the molecules in the β-phase gives rise to different distances between the respective closest hydrogen atom on a neighboring phenyl ring and the two oxygen atoms on the carboxylate groups (see sketch in Fig. 7.6). Assuming a complete deprotonation, both oxygen atoms would form a bond with that closest hydrogen atom. This would mean two different hydrogen bond lengths, which is unlikely to be a stable situation. A way out is a partial deprotonation (formation of a monocarboxylate), with only every second carboxyl group deprotonated [16]. The remaining hydrogen atom on one of the carboxyl groups is then taking part in a bond to one of the oxygen atoms on the next neighboring carboxyl group. The other pair of oxygen atoms form bonds with hydrogen atoms on neighboring phenyl rings (cf. sketch in Fig. 7.6). The different strengths of the two bonds explain the unequal bond lengths and therefore the rotation.
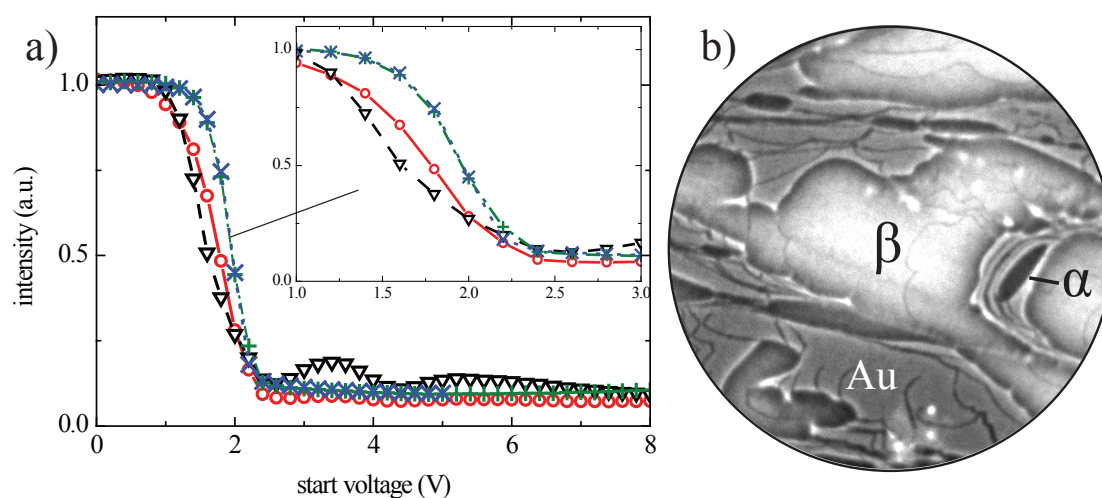
Figure 7.10: **(a)** LEEM IV curves taken from the α-phase (–○–), β-phase (--▽--), Au(111) covered with a 2D BDA gas (-··+-··) and from the clean Au(111) substrate (··×··). The curves are all normalized to the intensity at a start voltage of -5 V. The inset shows the voltage range from 1 to 3 V enlarged. **(b)** LEEM image taken at 3.2 V of the Au(111) surface covered both with the β and α-phase (see Sect. 7.3.5). FoV is 4 µm.

To further support a deprotonation at higher substrate temperatures, we took advantage of the spectroscopic capabilities of the LEEM and performed intensity-voltage (LEEM IV) measurements. We prepared a surface covered with both the β- and α-phase (cf. following Sect. 7.3.5) and recorded LEEM images while sweeping the start voltage from -5 V to 8 V. Figure 7.10 shows image intensity versus electron energy profiles measured on the α-, the β-

phase, and on the substrate covered with a 2D BDA gas in equilibrium with both the α- and β-phase. In separate experiments we recorded spectra for the γ-phase (not shown), which are similar to the β-phase spectra, and spectra for the clean Au(111) substrate.

The LEEM IV curve from the β domain shows two peaks in the voltage range at 3.2 V and 5.4 V, respectively. These peaks are also present in the α- and γ-phases, but weaker. It is impossible to discern here, whether these peaks originate from to the electronic structure of the molecules, or the crystalline order. Important for our analysis is the transition from reflection of electrons in front of the surface at negative start voltages, to interaction with the surface lattice (and therefore electron diffraction) at positive start voltages. The transition can be seen as a sharp decrease of the image intensity as the start voltage is increased from negative values. This is, because intensity is lost from the specular into higher order diffraction beams. The start voltage, at which this transition occurs, depends on the work function of the surface. For a material with a lower work function, the transition sets in at lower start voltages, as compared to a material with a higher work function [44, 123, 124]. As we can see in the inset in Fig. 7.10(a), the intensity obtained from the β-phase domain drops at slightly lower start voltages compared to the intensities α-phase and the Au substrate. The IV curve from the β-phase is shifted by approximately 0.3 V to lower voltages with respect to the curve from the α-phase. This corresponds to a reduction of the work function in the β-phase, as is expected for a deprotonated acid [106].

The transformation from the α-phase to the β-phase (Fig. 7.3) is irreversible; upon cooling the substrate the α-phase does *not* recover. This raises an important question: in which structure does BDA grow if β-phase nuclei are already available on the surface? If the molecules indeed deprotonate, they should form two different species on the surface: the protonated and the deprotonated molecule. Molecules that are deposited at lower temperatures belong to the protonated phase and cannot attach to existing β-phase domains, which are formed by the deprotonated species. On the other hand, at higher temperatures all molecules are (partially) deprotonated and either the existing β-phase domains should expand, or the γ-phase form.

To clarify this question, we deposited additional BDA once after cooling back down to room temperature after the transformation (Fig. 7.3) and once with the substrate kept at a temperature of 385 K, i.e. well above the transition temperature which is around 330 K. In the first case (see Fig. 7.11(a)), new needle like domains nucleated at step edges, just as if BDA was deposited on a clean substrate at the same temperature. Also the preexisting β-phase domains grew, however, only in length, through the nucleation of
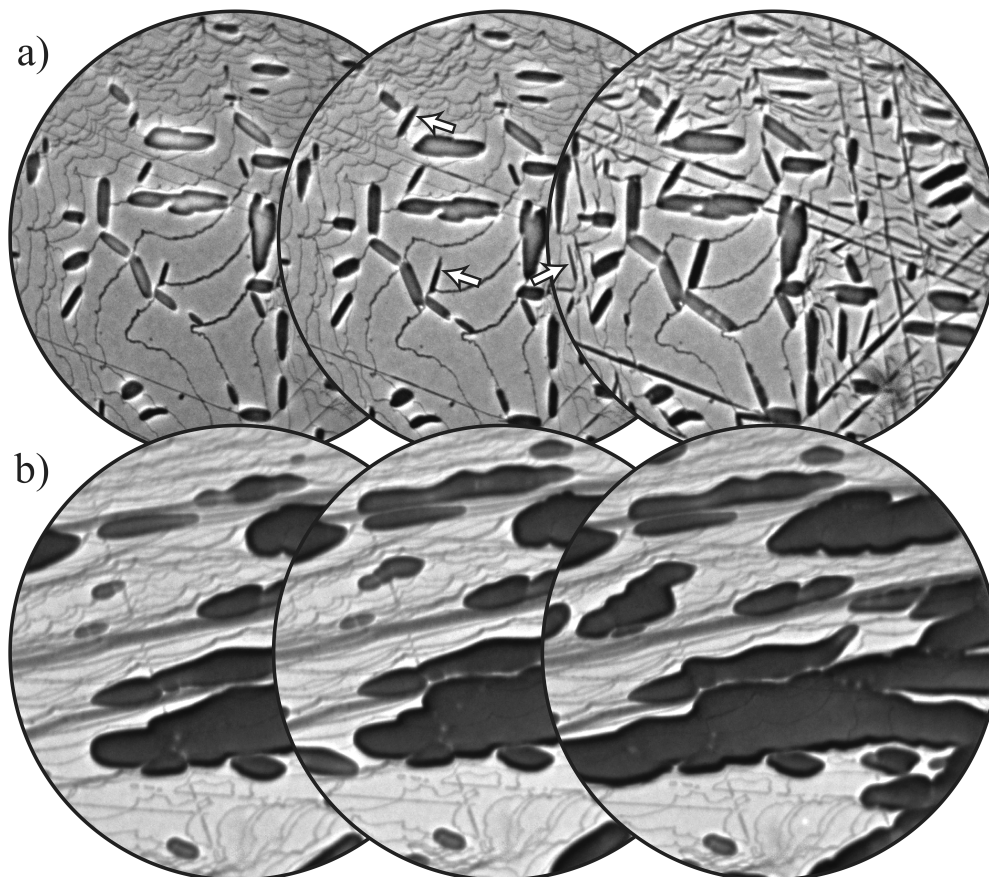
Figure 7.11: **(a)** Growth of BDA at $300\,\mathrm{K}$ on a surface already covered with the β-phase. New α-phase domains nucleate at step edges (arrows) and existing β-phase domains grow in length, not in width. **(b)** Growth of BDA at $385\,\mathrm{K}$ on a surface already covered with the β-phase. The existing domains grow in a non-continuous manner, covering entire Au terraces in short time where occasionally their expansion is temporarily interrupted.

needles at the apex of the domains. These needles have presumably also the α-phase structure - the structures are too small and too close for a meaningful µLEED analysis. This observation is consistent with a deprotonated species at higher temperatures. The protonated molecules nucleate in new domains with the α-phase structure. Apparently, the apexes of the existing β-phase domains act as strong nucleation centers. The latter is not surprising: The β domains were still elongated from the transformation of the α needles. The molecules in these β domains are thus oriented parallel to the long axis of the domains, and the domain apexes are terminated by unsaturated carboxylate / carboxyl groups. These groups act as nucleation centers for needles, imprinting their orientation on the growing needle.

The situation is different, if we add BDA at higher substrate temperatures (here T = $385\,\mathrm{K}$) to the surface with pre-existing β-phase domains. On the clean Au(111) surface, we would expect the growth of the γ-phase. Instead, the existing β domains grow. The growth proceeds in a step wise manner:

the domains are blocked at substrate steps temporarily, and then advance over the next terrace in short time (see Fig. 7.11(b)). Interestingly, domains of the γ-phase are not formed; the nucleation of new domains of any phase is not observed at all. The presence of β-phase nuclei inhibits the nucleation of the γ-phase effectively.

In summary, we have very strong evidence for a deprotonation of BDA on Au(111) above $\sim 330\,K$. This result is in strict contrast to the observations reported by Xiao et al. [19]. Xiao et al. observed domains with the α-phase structure and additionally domains with a rectangular crystal structure co-existing with the α-phase. We also observed the same rectangular structures (the γ-phase), however, only when depositing BDA directly at higher substrate temperatures above $\sim 330\,K$. To test, whether the rectangular phase is caused by a deprotonation and subsequent incorporation of Au ad-atoms, Xiao et al. annealed the Au(111) substrate up to $> 393\,K$. They did not observe a change in the relative coverages of both phases, and from this observation concluded that the BDA molecules do not deprotonate and that no Au ad-atoms get incorporated in the rectangular phase. We clearly observe the opposite: while on the molecular level the room temperature and the annealed phase are not too different, the different intermolecular interaction results in remarkable changes of the long range order. Conversely, this also means that the γ-phase, which forms during growth at high temperatures, is indeed a 2D metal-organic coordination network, with Au atoms incorporated in between where the (deprotonated) carboxylic-acid functional groups meet. The resulting structure bears remarkable resemblance to BDA-Mn networks on Au(111) [25].

Clearly, our results are not only contradictory to the observations by Xiao et al., but also to other STM studies on similar benzoic acids on Au(111) and under vacuum conditions [13, 115, 43, 122, 19, 108, 112]. The general consensus in these studies is, that benzoic acids do not deprotonate on Au(111), due to the low reactivity of the substrate. We can only speculate about the differences between the STM observations from Xiao et al. and our results. Except for a rotation of the molecules, the structure in the β-phase is identical to the α-phase. Therefore, it is probably hard or even impossible to notice the conversion of the α into the β-phase as a structure change in STM. Also, if we take into account the limited field of view in STM, it will be difficult to notice the dramatic change of the island shape and size after the transformation, which in LEEM is an obvious aspect. We can get some more information, if we take a closer look at Fig. 1(a) in reference [19]. The closed-packed domain attributed to the protonated species in that figure is not bordered by straight rows of molecules, as would be expected for the

α-phase, but ragged and clearly has a two dimensional character. In other STM studies, the protonated low temperature (α-)phase formed needle like structures [43, 25] (and also for TPA on Au(111) [13]). The sides of these needles in those studies are accurately terminated by almost perfect straight rows of molecules. One possible scenario is thus, that the closed-packed structures observed by Xiao et al. is in fact the (deprotonated) β-phase, which is why they did not observe a further change upon annealing the substrate. The presence of the γ-phase at room temperature, on the other hand, can be explained by deposition on a substrate that was still above room temperature after annealing during surface preparation. To clarify the picture we obtained here by studying mostly the ordering on the mesoscopic scale with LEEM, further research with other techniques is required. For example by imaging directly the intermolecular bonds with high resolution STM[125, 126] or by unambiguously assigning a deprotonation reaction with spectroscopic methods [106].

7.4 Conclusion

We studied the growth of BDA domains on Au(111) by Low Energy Electron Microscopy (LEEM) and μLEED. Depending on the growth temperature and temperature history, we observed the formation of three different phases. We attribute the occurrence of the different phases to the deprotonation of BDA on Au(111) above $\sim 330\,\mathrm{K}$.

The fact, that BDA deprotonates on Au(111) slightly above room temperature, is an important piece of information. It would be surprising, if this result is specific only for BDA, e.g., due to specific sites occupied on the substrate lattice. Molecules that diffuse on the substrate can probe all lattice sites, and will thus also find the more reactive sites. A deprotonation should therefore also occur for other benzoic-acids or even carboxylic-acids in general. Since benzoic-acids are a common class of molecules for self-assembly studies and Au(111) is a common substrate, our observations are relevant to a wide range of studies. Knowing the temperature window in which the acid groups deprotonate, allows to gain further control over the structures that are formed, however, also limits their stability. In our case, we can control reproducibly whether the molecules grow in a closed-packed (α- and β-phases) or an open structure (γ-phase) by adjusting the substrate temperature in a window smaller than $50\,\mathrm{K}$.

Summary

This thesis describes a study of the nucleation and growth behavior of two-dimensional supramolecular networks formed by 4,4'-biphenyldicarboxylic acid (BDA) molecules on metal crystal surfaces. The Cu(001) and the Au(111) surfaces were used as templates. On both surfaces, the molecules form highly ordered, hydrogen-bonded networks. These networks offer great promise for the use as flexible templates for the fabrication of novel nanoscale structures.

In this work, we investigated the nucleation, growth and decay of the supramolecular networks on the surfaces in-situ using low energy electron microscopy (LEEM). This microscope offers the capability to visualize in real-time processes on surfaces with a large field of view with good lateral resolution and at variable temperatures. At the same time, the molecular structure can be determined with selected area electron diffraction. In short, the most important results from this work are a deeper understanding of the thermodynamic driving forces behind the self-assembly process and the influence of the substrate (morphology) and temperature on the growth of the networks.

We found that on both the Cu(001) and the Au(111) surface, the BDA molecules adsorb in a planar geometry and form large two-dimensional islands in which the molecules organize in highly ordered networks. Single crystalline domains exceeding lateral dimensions of several micrometers, could be grown by optimizing the growth condition (i.e., temperature and growth rate). The interplay between intermolecular forces and the molecular interaction with the metal substrates plays an important role in the emerging detailed structure of the molecular network. However, we found that also the exact growth conditions, i.e., molecular coverage and growth temperature, can play a decisive role.

The major part of this work was devoted to BDA on Cu(001), which is a rather simple system, in the sense, that for a large range of growth parameters (temperature, coverage) we observe only one crystalline phase on the surface. In this phase, the basically flat lying, deprotonated molecules assemble in a square, hydrogen-bonded nanostructure, which forms a c(8×8) superstructure on the underlying Cu(001) surface. The c(8×8) islands are surrounded by a diluted, 2D "gas" phase formed by adsorbed and mobile BDA molecules. While we cannot observe the admolecules directly with

LEEM, we can see their presence as a decrease of the image intensity on the Cu terraces, due to diffuse scattering of the probing electron beam.

In Chapter 3, we quantified this intensity attenuation, and translated it into the density of admolecules in the diluted phase on the terraces. Therefore, in addition to the information on their size and growth rate, we also have microscopic information on the density of molecules in front of the 2D crystallites. Next, we measured the density for which the two phases (dilute and c(8×8)) are in equilibrium as a function of temperature. The resulting phase diagram was interpreted in terms of a 2D lattice gas model and we extracted a 2D cohesive energy of $0.35\,\mathrm{eV} \pm 0.03\,\mathrm{eV}$. We found that the density of molecules in the diluted phase is quite large, reaching up-to half the density in the c(8×8) structure. While this is partially due to the weak intermolecular interaction, also entropy effects play a major role. Since the molecules are large compared to the underlying Cu lattice, a multitude of equivalent translational adsorption sites are allowed, which is thus increasing the entropy in the diluted phase. In the same chapter, we also studied the decay dynamics of c(8×8) domains after an increase of temperature and estimated the admolecule diffusion constants to be between $650\,\mathrm{nm^2\,s^{-1}}$ and $1300\,\mathrm{nm^2\,s^{-1}}$ in the temperature window of $362\,\mathrm{K}$ to $400\,\mathrm{K}$.

The critical nucleus size is a common concept in nucleation models, which describes the smallest stable structure during nucleation. Smaller nuclei tend to be unstable, larger nuclei tend to be stable. In epitaxial growth studies of atomic species, the critical nucleus consists in many cases out of just a few atoms or molecules and it is impossible to observe these small, short-lived fluctuations directly. In Chapter 4, we show that for growth of BDA on Cu(001), the critical nucleus can become huge, containing hundreds of molecules. These critical nuclei exist long enough (seconds) to be observed directly in LEEM. Surprisingly, we found that nuclei which are several times larger than the critical nucleus, and should be post-critical, still have a finite probability to decay. This behavior is explained with the slow diffusion of admolecules, which leads to large concentration gradients that can either stabilize or destabilize growing nuclei.

While the BDA networks nucleate on Cu terraces, larger domains inevitably meet substrate steps. In Chapter 5, we studied the influence of the substrate morphology on the c(8×8) domain growth. For that, we deposited BDA with the substrate at an elevated temperature of $410\,\mathrm{K}$, which, due to the increased molecular mobility, leads to a very low island density, much smaller than the number of terraces. We found that steps effectively terminate the expansion of the BDA domains, but are transparent to individual admolecules. This leads to an anomalous nucleation behavior: Once

the initial domains cover their respective host terrace, subsequent domains nucleate on neighboring terraces. Before the domains hit the steps, they feature a ramified shape, caused by a Mullins-Sekerka type growth instability. This includes a so far not observed Mullins-Sekerka type growth instability, that is characterized by high growth rates *along*, instead of *perpendicular* to the Cu steps.

For low BDA coverage, we only observed a c(8×8) BDA superstructure on Cu(001). However, for more extreme growth conditions, i.e., high coverage and elevated temperatures (> 370 K), we observed a second surface confined structure, in which the molecules are 14% denser packed than in the c(8×8) structure. Still, the molecules form a commensurate structure on the Cu(001) substrate, which is reflecting the strong interaction between molecules and substrate. A LEEM and µLEED analysis of this compressed phase is presented in Chapter 6. The compressed phase is observed first during BDA deposition in the center of large c(8×8) domains. This is presumably due to a higher density of admolecules on the c(8×8) layer there. At about 400 K the compressed phase is not stable in the absence of the 3D gas phase, and slowly transforms back into the c(8×8) structure after stopping BDA deposition.

Finally, Chapter 7 deals with the growth of BDA domains on Au(111). We found that the BDA molecules form three different crystalline structures on the surface. Unlike for the case of Cu(001), the carboxylic acid groups of the BDA molecules are protonated when deposited with the Au(111) substrate held at room temperature. Under this condition, the molecules form a closed packed structure, in which the molecules form chains and interact through relatively strong head-to-tail hydrogen bonds between carboxylic acid groups. The anisotropy of the molecular interaction is reflected by an elongated, needle-like shape of the domains. Upon annealing the substrate above approximately 330 K, the molecules deprotonate and the hydrogen bonds between the acid groups break. Accompanying this, we observed a spectacular change of the BDA domain shapes from needle like to compact. This is attributed to an increased molecular interaction within the domains. A third crystalline phase is formed by direct deposition with the substrate temperature above 330 K. Here, the molecules order in an open nanostructure, presumably with Au adatoms being incorporated as linkers forming metal-organic coordination bonds.

In conclusion, this work demonstrates that the self-assembly of molecules on metal surfaces can be generally described with known concepts from epitaxial growth of atomic species. However, these concepts need to be adjusted to account simply for the size of the molecules and for the possibility of

chemical modifications, e.g., deprotonation. As we have shown in the third chapter, the size and the shape of the molecules may lead to a large fraction of molecules in a disordered phase, due to a strong impact from entropy. This is an important aspect, for example, the high density in the dilute phase leads directly to the anomalous size fluctuations we observed during nucleation of domains on Cu(001). On the other hand, the temperature induced deprotonation of the molecules can be employed to tailor how the molecules interact mutually, as shown for the example of BDA on Au(111).

Samenvatting

Dit proefschrift beschrijft de nucleatie en groei van twee-dimensionale supramoleculaire netwerken, die bestaan uit 4,4'-biphenyldicarboxylic acid (BDA) moleculen, op metaal oppervlakken. Als templates werden Cu(001) en Au(111) oppervlakken gebruikt. De moleculen vormen op beide oppervlakken goed geordende netwerken, waarbij de moleculen via waterstofbruggen wisselwerken. Deze netwerken worden als kansrijk beschouwd voor gebruik als flexibele templates voor het maken van nieuwe nanoscopische structuren.

Hier hebben wij de nucleatie, de groei en het verval van de supramoleculaire netwerken met behulp van in-situ Lage Energie Elektronen Microscopie (LEEM) onderzocht. Deze microscopie biedt de mogelijkheid om processen op oppervlakken op een relatief grote lengte schaal met goede laterale resolutie en bij variabele temperatuur waar te nemen. Tegelijkertijd kan de exacte structuur van het moleculaire netwerk met behulp van lokale elektronen diffractie (μLEED) in gebiedjes van 1.4 micrometer bepaald worden. Het belangrijkste huidige resultaat is een fundamenteel inzicht in de thermodynamisch drijvende kracht achter de spontane vorming van de netwerken en in de invloed van de morfologie en de temperatuur van het substraat op de groei van de netwerken.

Wij hebben gevonden, dat op beide oppervlakken de BDA moleculen vrijwel vlak liggen en grote twee-dimensionale eilandjes vormen, die bestaan uit moleculaire netwerken. Monokristallijne domeinen met laterale afmetingen groter dan enkele micrometers konden door het optimaliseren van de groei parameters (d.w.z. temperatuur en groeitempo) gerealiseerd worden. Het samenspel van de intermoleculaire krachten en de moleculaire interactie met het metaal oppervlak bepaalt de ontstane structuur van de moleculaire netwerken. Maar ook de precieze groei condities, d.w.z. moleculaire bedekking en substraat temperatuur, kunnen een doorslaggevende rol spelen.

Het grootste deel van dit proefschrift is gewijd aan BDA op Cu(001). Dit is een relatief eenvoudig systeem omdat wij voor een groot bereik van de groei parameters (temperatuur, bedekking) één enkele kristallijne fase observeren. In deze fase zijn de vrij vlak liggende, gedeprotoneerde moleculen gebonden door waterstofbruggen en vormen een vierkant rooster. Het rooster vormt een c(8×8) superstructuur op het onderliggende Cu(001) substraat. Rond de c(8×8) eilandjes bevindt zich een verdunde, 2D "gas" fase, gevormd door

geïsoleerde en mobiele BDA moleculen. Wij kunnen deze admoleculen niet direct waarnemen, maar kunnen wel hun invloed op de LEEM intensiteit van de Cu terrassen zien, omdat de admoleculen de inkomende elektronenbundel diffuus verstrooien.

In hoofdstuk 3, hebben wij deze intensiteitvermindering gekwantificeerd, en in de dichtheid van admoleculen op de koper terrassen vertaald. Boven op de informatie over de omvang en groeisnelheid van de 2D kristallijne fase, hebben wij daarmee ook microscopische kennis m.b.t. de dichtheid van admoleculen rond de 2D eilandjes. Vervolgens hebben wij het evenwicht tussen beiden fasen als functie van de temperatuur gemeten. Het resulterende fasendiagram wordt verklaard aan de hand van een 2D rooster gas mode. Uit de vorm van de fasencoëxistentielijn leiden we een 2D cohesieve energy van $0.35\,\text{eV} \pm 0.03\,\text{eV}$ af. De dichtheid van de moleculen in de verdunde fase is relatief groot. Afhankelijk van de temperatuur kan zij tot bijna de helft van de dichtheid in de c(8×8) structuur bedragen. Dit kan gedeeltelijk door de zwakke wisselwerking tussen moleculen worden verklaard, maar ook entropie effecten spelen een grote rol. Omdat de moleculen groot zijn in vergelijking tot het onderliggende Cu rooster, zijn er diverse gelijkwaardige adsorptieplaatsen beschikbaar, die de entropie in de verdunde fase verhogen. In hetzelfde hoofdstuk hebben wij ook de verval dynamica van de c(8×8) domeinen na een temperatuurverhoging onderzocht en de diffusie constante voor de geadsorbeerde moleculen in het temperatuur bereik van $362\,\text{K}$ tot $400\,\text{K}$ afgeleid.

De kritische kiemgrootte is een karakteristiek concept, dat de kleinste stabiele structuur tijdens nucleatie beschrijft. Kleinere kiemen zijn instabiel en vervallen, grotere nuclei zijn stabiel en groeien verder. In epitaxiale groei studies van atomaire lagen bestaat de kritische nucleus vaak uit een handvol atomen, en is het zo goed als onmogelijk deze kleine en kort levende fluctuaties direct te observeren. In hoofdstuk 4, laten we zien, dat tijdens de groei van BDA op Cu(001), de kritische nucleus zeer groot wordt en uit honderden moleculen kan bestaan. Deze kritische nuclei leven lang genoeg (seconden) om ze direct met LEEM te zien. Verrassend hebben wij gevonden, dat nuclei die zo'n zes maal groter zijn dan de kritische nucleus, nog steeds met een eindige waarschijnlijkheid vervallen. Dit gedrag wordt toegeschreven aan de langzame diffusie van de moleculen, die tot grote concentratie gradiënten leidt, welke lokaal een stabiliserende of destabiliserende invloed op de groeiende kiemen hebben.

Waar de BDA netwerken op Cu terrassen kiemen, stuiten de groeiende domeinen onvermijdelijk op de atomaire stappen op het substraat. In hoofdstuk 5, hebben we de invloed van de substraat morfologie op de groei van de

c(8×8) domeinen bestudeerd. Daarvoor hebben we de BDA moleculen bij een relatief hoge temperatuur van 410 K op het substraat gedeponeerd. Bij de toegenomen beweeglijheid van de admoleculen is de nucleatie dichtheid van de eilandjes nu heel laag, d.w.z. vele malen kleiner dan één per terras. Wij vonden, dat de substraat stappen de BDA domeingroei effectief blokkeren, maar eenvoudig gepasseerd kunnen worden door individuele moleculen. Dit leidt tot een abnormaal en niet eerder gerapporteerd nucleatie gedrag: Zodra de initiële domeinen hun eigen terras volledig bedekken neemt de dichtheid in de 2D gas fase weer toe en vormen zich nieuwe domeinen op tot dusver lege terrassen. Voordat de domeinen de stappen bereiken, nemen ze een meer en meer vertakte vorm aan . Dit wordt veroorzaakt door Mullins-Sekerka groei instabiliteiten. Die omvatten een nog niet eerder waargenomen groei instabiliteit van het Mullins-Sekerka type, welke veroorzaakt wordt door een relatief snelle groei langs stappen, in plaats van de klassiek snelle groei loodrecht op de stappen.

Voor lage BDA bedekking, hebben wij alleen de c(8×8) BDA superstructuur op Cu(001) geobserveerd. Maar voor meer extreme groeicondities, d.w.z. hogere bedekkingen en temperaturen (> 370 K), hebben wij een tweede twee-dimensionale kristallijne structuur gevonden. In deze structuur zijn de moleculen 14% dichter gepakt in vergelijking met de c(8×8) structuur. Deze structuur met de matrix notatie $\left(\begin{smallmatrix} 5 & -7 \\ 5 & 4 \end{smallmatrix}\right)$ is steeds commensurabel m.b.t. het onderliggende Cu(001) rooster. Dit weerspiegelt de sterke wisselwerking tussen de moleculen en het substraat. Een LEEM en μLEED analyse van deze gecomprimeerde fase wordt in hoofdstuk 6 besproken. De gecomprimeerde fase ontstaat eerst in het midden van grote c(8×8) domeinen tijdens BDA depositie. Dit wordt mogelijk gemaakt door een hoge dichtheid van admoleculen op de c(8×8) laag. De gecomprimeerde fase is niet stabiel boven ongeveer 400 K en transformeert langzaam terug naar de c(8×8) structuur in afwezigheid van de 3D gas fase na het stoppen van de BDA depositie. Dit wordt toegeschreven aan een meer macroscopische herverdeling van het geadsorbeerde materiaal of aan verlies van moleculen aan het vacuum.

Tenslotte wordt in hoofdstuk 7 de groei van de BDA domeinen op Au (111) behandeld. We vonden dat de BDA moleculen drie verschillende kristallijne structuren op het oppervlak vormen. In tegenstelling tot Cu(001) blijven de carbonzuurgroepen van de BDA moleculen geprotoneerd als de moleculen bij kamertemperatuur op Au(111) worden gedeponeerd. Bij kamertemperatuur vormen de moleculen een gesloten structuur en wisselwerken de moleculen via een relatief sterke kop-staart waterstofbruggen tussen de carbonzuurgroepen. De anisotropie van de moleculaire interactie wordt gekenmerkt door langwerpige, naaldvormige domeinen. Bij het verhogen van de substraat tem-

peratuur boven ongeveer 330 K, deprotoneren de moleculen en dientengevolge verdwijnen de waterstofbruggen tussen de zuurgroepen. Tegelijkertijd zagen we een spectaculaire verandering van de vorm van de BDA domeinen van naaldvormig naar compact. Dit wordt aan minder anistrope moleculaire interactie in de domeinen toegeschreven. Een derde kristallijne fase wordt gevormd door directe BDA depositie op het substraat op een temperatuur boven 330 K. In deze fase vormen de moleculen een openen nanostructuur, vermoedelijk met Au adatom opgenomen als verbindingsstukken in het metaal-organische coördinatie netwerk.

Samenvattend hebben we laten zien, dat de zelfassemblage van moleculen op metaal oppervlakken algemeen beschreven kan worden met bekende concepten van epitaxiale groei van atomaire kristallen. Echter deze concepten moeten aangepast worden om effecten t.g.v de grootte en vorm van de moleculen en van mogelijke chemische modificaties, zoals bijvoorbeeld deprotonering, in rekening te brengen. Zoals wij in het derde hoofdstuk laten laten zien kan de grootte en de vorm van de moleculen tot een hoge concentratie van moleculen in de ongeordende fase leiden. Dit is een belangrijk aspect. De hoge dichtheid in de verdunde fase leidt bijvoorbeeld direct tot de abnormaal grote fluctuaties van de kiemgroottes, welke wij tijdens nucleatie van BDA domeinen op Cu(001) hebben gezien. Anderzijds kan de temperatuur geïnduceerde deprotonering van de moleculen worden gebruikt om gecontroleerd de netwerkstructuur van de moleculen te bepalen, zoals in het voorbeeld van BDA op Au (111).

Bibliography

[1] B. D. Gates *et al.*, Chem. Rev. **105**, 1171 (2005).

[2] G. Binnig and H. Rohrer, Surf. Sci. **126**, 236 (1983).

[3] D. Eigler and E. Schweizer, Nature **344**, 524 (1990).

[4] G. Whitesides, J. Mathias, and C. Seto, Science **254**, 1312 (1991).

[5] D. Philp and J. F. Stoddart, Angew. Chem. Int. Edit **35**, 1154 (1996).

[6] G. M. Whitesides and B. Grzybowski, Science (New York, N.Y.) **295**, 2418 (2002).

[7] J. V. Barth *et al.*, Angew. Chem. Int. Edit **39**, 1230 (2000).

[8] J. V. Barth, Annu. Rev. Phys. Chem. **58**, 375 (2007).

[9] S. L. Tait, ACS Nano **2**, 617 (2008).

[10] A. Dmitriev *et al.*, J. Phys. Chem. B **106**, 6907 (2002).

[11] S. Stepanow *et al.*, J. Phys. Chem. B **108**, 19392 (2004).

[12] S. Stepanow *et al.*, Nano Lett. **5**, 901 (2005).

[13] S. Clair *et al.*, J. Phys. Chem. B **108**, 14585 (2004).

[14] T. Classen *et al.*, J. Phys. Chem. A **111**, 12589 (2007).

[15] A. Langner *et al.*, Proc. Natl. Acad. Sci. U. S. A. **104**, 17927 (2007).

[16] M. Ruben *et al.*, J. Am. Chem. Soc. **128**, 15644 (2006).

[17] S. Stepanow *et al.*, Nat. Mater. **3**, 229 (2004).

[18] M. E. Cañas Ventura *et al.*, J. Chem. Phys. **125**, 184710 (2006).

[19] W. D. Xiao *et al.*, J. Phys. Chem. C **114**, 6646 (2010).

[20] M. Lackinger and W. M. Heckl, Langmuir **25**, 11307 (2009).

[21] A. Langner *et al.*, Angew. Chem., Int. Ed. **51**, 4327 (2012).

[22] R.-Q. Zhong *et al.*, CrystEngComm **12**, 677 (2010).

[23] M. R. Montney, R. M. Supkowski, and R. L. LaDuca, CrystEngComm **10**, 111 (2008).

[24] X.-L. Wang *et al.*, CrystEngComm **10**, 349 (2008).

[25] Y.-F. Zhang, N. Zhu, and T. Komeda, Surf. Sci. **602**, 614 (2008).

[26] S. Stepanow, N. Lin, J. V. Barth, and K. Kern, J. Phys. Chem. B **110**, 23472 (2006).

[27] J. V. Barth, G. Costantini, and K. Kern, Nature **437**, 671 (2005).

[28] J. A. Venables, G. D. T. Spiller, and M. Hanbucken, Rep. Prog. Phys. **47**, 399 (1984).

[29] M. Zinke-Allmang, L. C. Feldman, and M. H. Grabow, Surf. Sci. Rep. **16**, 377 (1992).

[30] E. Bauer, Ultramicroscopy **119**, 18 (2011).

[31] W. Telieps and E. Bauer, Ultramicroscopy **17**, 57 (1985).

[32] E. Bauer, Rep. Prog. Phys. **57**, 895 (1994).

[33] J. de la Figuera, N. C. Bartelt, and K. McCarty, Surf. Sci. **600**, 4062 (2006).

[34] E. Loginova, N. C. Bartelt, P. J. Feibelman, and K. F. McCarty, New J. Phys. **10**, 093026 (2008).

[35] E. Loginova, N. C. Bartelt, P. J. Feibelman, and K. F. McCarty, New J. Phys. **11**, 063046 (2009).

[36] B. Poelsema, L. K. Verheij, and G. Comsa, Phys. Rev. Lett. **51**, 2410 (1983).

[37] U. Linke and B. Poelsema, J. Phys. E **18**, 26 (1985).

[38] F. S. Khokhar *et al.*, J. Chem. Phys. **135**, 124706 (2011).

[39] R. Bouwman, J. Vac. Sci. Technol. **15**, 91 (1978).

[40] J. K. Gimzewski, Science **283**, 1683 (1999).

[41] N. Lin *et al.*, Angew. Chem. Int. Edit **41**, 4779 (2002).

[42] C. Perry, S. Haq, B. G. Frederick, and N. V. Richardson, Surf. Sci. **409**, 512 (1998).

[43] N. Zhu, T. Osada, and T. Komeda, Surf. Sci. **601**, 1789 (2007).

[44] F. S. Khokhar, R. van Gastel, and B. Poelsema, Phys. Rev. B **82**, 205409 (2010).

[45] B. Poelsema, L. K. Verheij, and G. Comsa, Surf. Sci. **152-153**, 851 (1985).

[46] B. Poelsema, S. T. de Zwart, and G. Comsa, Phys. Rev. Lett. **51**, 522 (1983).

[47] B. Poelsema, L. K. Verheij, and G. Comsa, Phys. Rev. Lett. **49**, 1731 (1982).

[48] I. V. Markov, *Crystal Growth For Beginners*, 2nd edition ed. (World Scientific, Singapore, 2003).

[49] M. J. Sparnaay, Surf. Sci. Rep. **4**, 101 (1985).

[50] A. Bilić *et al.*, J. Chem. Theory Comput. **2**, 1093 (2006).

[51] H. Ibach, *Physics of Surfaces and Interfaces*, 1 ed. (Springer-Verlag, Berlin, Heidelberg, New York, 2006).

[52] J. A. Venables, *Introduction to Surface and Thin Film Processes* (Cambridge University Press, Cambridge, 2000).

[53] S. Berner *et al.*, Chem. Phys. Lett. **348**, 175 (2001).

[54] J. Ikonomov, C. H. Schmitz, and M. Sokolowski, Phys. Rev. B **81**, 195428 (2010).

[55] T. Steiner, Angew. Chem. Int. Edit **41**, 49 (2002).

[56] G. Schulze Icking-Konert, Surf. Sci. **398**, 37 (1998).

[57] K. Morgenstern, Surf. Sci. **441**, 289 (1999).

[58] K. Morgenstern, G. Rosenfeld, and G. Comsa, Phys. Rev. Lett. **76**, 2113 (1996).

[59] G. Rosenfeld *et al.*, Surf. Sci. **402-404**, 401 (1998).

[60] W. Theis, N. C. Bartelt, and R. M. Tromp, Phys. Rev. Lett. **75**, 3328 (1995).

[61] H. Hibino, C. W. Hu, T. Ogino, and I. S. T. Tsong, Phys. Rev. B **63**, 245402 (2001).

[62] Q. Zheng and J. D. Gunton, Phys. Rev. A **39**, 4848 (1989).

[63] M. Giesen, Prog. Surf. Sci. **68**, 1 (2001).

[64] P. A. Thiel, M. Shen, D.-J. Liu, and J. W. Evans, J. Phys. Chem. C **113**, 5047 (2009).

[65] I. Lifshitz and V. Slyozov, J. Phys. Chem. Solids **19**, 35 (1961).

[66] B. Gilbert *et al.*, Ultramicroscopy **83**, 129 (2000).

[67] J. Weckesser, J. V. Barth, and K. Kern, J. Chem. Phys. **110**, 5351 (1999).

[68] J. Ikonomov, P. Bach, R. Merkel, and M. Sokolowski, Phys. Rev. B **81**, 161412 (2010).

[69] R. Gomer, Rep. Prog. Phys **53**, 917 (1990).

[70] G. L. Kellog, Surf. Sci. Rep. **21**, 1 (1994).

[71] E. C. Viljoen and C. Uebing, Langmuir **13**, 1001 (1997).

[72] R. M. Tromp and J. B. Hannon, Surf. Rev. Lett. **9**, 1565 (2002).

[73] W. Theis and R. Tromp, Phys. Rev. Lett. **76**, 2770 (1996).

[74] I. Goldfarb, Phys. Rev. Lett. **95**, 025501 (2005).

[75] D. Jesson, M. Kästner, and B. Voigtländer, Phys. Rev. Lett. **84**, 330 (2000).

[76] B.-S. Lee *et al.*, Science **326**, 980 (2009).

[77] U. Gasser *et al.*, Science **292**, 258 (2001).

[78] D. Schwarz, R. van Gastel, H. Zandvliet, and B. Poelsema, Phys. Rev. B **85**, 235419 (2012).

[79] S. A. Nepijko, N. N. Sedov, and G. Schönhense, J. Microsc. **203**, 269 (2001).

[80] O. Ivasenko and D. F. Perepichka, Chem. Soc. Rev. **40**, 191 (2011).

[81] J. V. Barth, Surf. Sci. **603**, 1533 (2009).

[82] B. Poelsema *et al.*, Appl. Phys. A **53**, 369 (1991).

[83] M. Bott, T. Michely, and G. Comsa, Surf. Sci. **272**, 161 (1992).

[84] T. Michely, M. Hohage, M. Bott, and G. Comsa, Phys. Rev. Lett. **70**, 3943 (1993).

[85] G. Rosenfeld *et al.*, Appl. Phys. A **61**, 455 (1995).

[86] G. Rosenfeld, B. Poelsema, and G. Comsa, J. Cryst. Growth **151**, 230 (1995).

[87] H. Brune, Surf. Sci. Rep. **31**, 125 (1998).

[88] T. Michely and J. Krug, in *Islands, Mounds and Atoms*, 1 ed., edited by G. Ertl, H. Lüth, and D. L. Mills (Springer-Verlag, Berlin, Heidelberg, New York, 2004).

[89] J. Evans, P. Thiel, and M. Bartelt, Surf. Sci. Rep. **61**, 1 (2006).

[90] P. Gambardella *et al.*, Surf. Sci. **449**, 93 (2000).

[91] W. W. Mullins and R. F. Sekerka, J. Appl. Phys. **34**, 323 (1963).

[92] W. W. Mullins and R. F. Sekerka, J. Appl. Phys. **35**, 444 (1964).

[93] G. Bales and A. Zangwill, Phys. Rev. B **41**, 5500 (1990).

[94] L. Schwenger, R. L. Folkerts, and H.-J. Ernst, Phys. Rev. B **55**, R7406 (1997).

[95] T. Maroutian, L. Douillard, and H.-J. Ernst, Phys. Rev. B **64**, 165401 (2001).

[96] D. Schwarz, R. van Gastel, H. Zandvliet, and B. Poelsema, Phys. Rev. Lett. **109**, 016101 (2012).

[97] D. E. Hooks, T. Fritz, and M. D. Ward, Adv. Mater. **13**, 227 (2001).

[98] L. Kilian *et al.*, Surf. Sci. **602**, 2427 (2008).

[99] M. Stöhr *et al.*, Angew. Chem., Int. Ed. **44**, 7394 (2005).

[100] L. Kilian *et al.*, Phys. Rev. Lett. **100**, 136103 (2008).

[101] C. Stadler *et al.*, Nature Physics **5**, 153 (2009).

[102] G. Ertl, M. Neumann, and K. Streit, Surf. Sci. **64**, 393 (1977).

[103] S. Soubatch, I. Kröger, C. Kumpf, and F. Tautz, Phys. Rev. B **84**, 195440 (2011).

[104] Y. Ye *et al.*, J. Phys. Chem. C **111**, 10138 (2007).

[105] P. Bak, Rep. Prog. Phys. **45**, 587 (1982).

[106] B. Immaraporn, P. Ye, and A. J. Gellman, J. Phys. Chem. B **108**, 3504 (2004).

[107] Q. Chen *et al.*, Surf. Sci. **446**, 63 (2000).

[108] Z. Pei *et al.*, Electrochim. Acta **55**, 8287 (2010).

[109] S. Stepanow, N. Lin, and J. V. Barth, J. Phys.: Condens. Matter **20**, 184002 (2008).

[110] C. Heininger, L. Kampschulte, W. M. Heckl, and M. Lackinger, Langmuir **25**, 968 (2009).

[111] M. A. Lingenfelder *et al.*, Chemistry **10**, 1913 (2004).

[112] C. S. Kley *et al.*, J. Am. Chem. Soc. **134**, 6072 (2012).

[113] D. Martin, R. Cole, and S. Haq, Phys. Rev. B **66**, 155427 (2002).

[114] Y. Ge *et al.*, Langmuir **26**, 16325 (2010).

[115] S. Clair *et al.*, J. Phys. Chem. B **110**, 5627 (2006).

[116] M. Śledź and J. Janczak, J. Mol. Struct. **595**, 77 (2001).

[117] B. I. Kim, J. Hanson, M. Turner, and L. Reeder, Surf. Sci. **606**, 1340 (2012).

[118] A. Bilić *et al.*, J. Chem. Theory Comput. **2**, 1093 (2006).

[119] T. Neuheuser, B. A. Hess, C. Reutel, and E. Weber, J. Phys. Chem. **98**, 6459 (1994).

[120] M. Van Hove *et al.*, Surf. Sci. **103**, 189 (1981).

[121] J. Barth, H. Brune, G. Ertl, and R. Behm, Phys. Rev. B **42**, 9307 (1990).

[122] Y. F. Zhang, Y. Yang, Y. Kawazoe, and T. Komeda, J. Chem. Phys. **131**, 174706 (2009).

[123] Y. Murata *et al.*, Applied Physics Letters **97**, 143114 (2010).

[124] Y. Murata *et al.*, Physical Review B **85**, 205443 (2012).

[125] R. Temirov *et al.*, New J. Phys. **10**, 053012 (2008).

[126] C. Weiss, C. Wagner, R. Temirov, and F. S. Tautz, J. Am. Chem. Soc. **132**, 11864 (2010).

List of Publications

1. D. Schwarz, H. Wormeester and B. Poelsema, "Validity of Lorentz-Lorenz equation in porosimetry studies", Thin Solid Films **519**, 2994 (2011).

2. F.S. Khokhar, R. van Gastel, D. Schwarz, H.J.W. Zandvliet and B. Poelsema, "A Low Energy Electron Microscopy study of the initial growth, structure and thermal stability of BDA-domains on Cu(001)", Journal of Chemical Physics **135**, 124706 (2011).

3. D. Schwarz, R. van Gastel, H.J.W. Zandvliet and B. Poelsema, "Phase transformations of 4,4'-biphenyldicarboxylic acid on Cu(001)", Physical Review B **85**, 234706 (2012).

4. D. Schwarz, R. van Gastel, H.J.W. Zandvliet and B. Poelsema, "Size fluctuations of near critical nuclei and Gibbs free energy for nucleation of BDA on Cu(001)", Physical Review Letters **109**, 016101 (2012).

5. D. Schwarz, R. van Gastel, H.J.W. Zandvliet and B. Poelsema, "Growth anomalies in supramolecular networks: 4,4'-biphenyldicarboxylic acid on Cu(001)", submitted.

6. D. Schwarz, R. van Gastel, H.J.W. Zandvliet and B. Poelsema, "In-situ observation of a deprotonation driven phase transformation - 4,4'-biphenyldicarboxylic acid on Au(111)", in preparation.

7. D. Schwarz, R. van Gastel, H.J.W. Zandvliet and B. Poelsema, "Formation and decay of a compressed phase of 4,4'-biphenyldicarboxylic acid on Cu(001)", in preparation.

Acknowledgements

Writing a thesis and especially the accompanying experiments can be an extremely difficult and frustrating task. Fortunately, I had many colleagues who could always help and motivate me.

First of all I want to thank my supervisor, Prof. Bene Poelsema. Bene, thank you for your continuous support. I was always sure to have your support and your door was always open to talk about any ideas, scientific or not.

Raoul, thank you for introducing me into the LEEM and your help with the instrument. Especially my thanks for your fine tuning of my presentation for the PEC!

Herbert, the experimental training I got from you was priceless, thank you for that!

Harold, thank you for proof reading and your help with the manuscripts!

Gregor thank you for all the discussions on organic film growth!

My thanks to Hans and Hermann for their quick help with technical problems.

I want to thank the group's secretaries, Rianne and later Simone, for their friendly help with administrative problems.

Thanks to Avijit, Frank, Maciej, Rene, Stefan, Tijs, Tjeerd and all the other (former) colleagues for the nice conversations during lunch or other occasions, I wish you all the best for the future!

I want to thank my family and friends. Especially my parents, who always supported me in what I did and my sister, who helped me with the cover of this thesis.

And finally, Vasilisa, you were always there for me, even when I had to work a lot at the end. You made the most stressful times pass easy, thank you for that!

Curriculum Vitae - Daniel Schwarz

Date of Birth: 25th July 1983   **In**: Mainz, Germany

Education

2008 – Present	Ph.D. student in physics at the MESA+ Institute for Nanotechnology - University of Twente *An in-situ study of the molecular structure and growth kinetics and thermodynamics of organic layers on metal surfaces using LEEM and selected area diffraction.* Supervisors: Prof. Bene Poelsema and Dr. Raoul van Gastel
2008	Diploma in Physics from the University of Hamburg
2007-2008	Diploma Thesis at the Austrian Research Center, Vienna *'Characterization of embedded MgO-based Ferromagnet-Insulator contacts to silicon'* Supervisors: Priv. Doz. Dr. Hubert Brückl and Dr. Theodore Dimopoulos
2003 – 2008	Study of Physics at the University of Hamburg
1995 – 2003	Gymnasium, Bad Oldesloe

Awards

Wayne B. Nottingham Prize at the 72nd Annual Physical Electronics Conference, Dallas (2012)